Modeling Wildland Fire Radiance in Synthetic Remote Sensing Scenes

by

Zhen Wang

B.S. Beijing Institute of Technology, 1996

A dissertation submitted in partial fulfillment of the
requirements for the degree of Doctor of Philosophy
in the Chester F. Carlson Center for Imaging Science
Rochester Institute of Technology

August 09, 2007

Signature of the Author _____

Accepted by _____
         Coordinator, Ph.D. Degree Program   Date

CHESTER F. CARLSON CENTER FOR IMAGING SCIENCE

ROCHESTER INSTITUTE OF TECHNOLOGY

ROCHESTER, NEW YORK

<u>CERTIFICATE OF APPROVAL</u>

Ph.D. DEGREE DISSERTATION

The Ph.D. Degree Dissertation of Zhen Wang
has been examined and approved by the
dissertation committee as satisfactory for the
dissertation required for the
Ph.D. degree in Imaging Science

Dr. Anthony Vodacek, Dissertation Advisor

Dr. Robert Kremens

Dr. Carl Salvaggio

Dr. Robert Teese

Date

DISSERTATION RELEASE PERMISSION

ROCHESTER INSTITUTE OF TECHNOLOGY

CHESTER F. CARLSON CENTER FOR IMAGING SCIENCE

Title of Dissertation:

Modeling Wildland Fire Radiance in Synthetic Remote Sensing Scenes

I, Zhen Wang, hereby grant permission to Wallace Memorial Library of R.I.T. to reproduce my thesis in whole or in part. Any reproduction will not be for commercial use or profit.

Signature _____

Date

Modeling Wildland Fire Radiance in Synthetic Remote Sensing Scenes

by

Zhen Wang

Submitted to the
Chester F. Carlson Center for Imaging Science
in partial fulfillment of the requirements
for the Doctor of Philosophy Degree
at the Rochester Institute of Technology

Abstract

This thesis develops a framework for implementing radiometric modeling and visualization of wildland fire. The ability to accurately model physical and optical properties of wildfire and burn area in an infrared remote sensing system will assist efforts in phenomenology studies, algorithm development, and sensor evaluation. Synthetic scenes are also needed for a Wildland Fire Dynamic Data Driven Applications Systems (DDDAS) for model feedback and update. A fast approach is presented to predict 3D flame geometry based on real time measured heat flux, fuel loading, and wind speed. 3D flame geometry could realize more realistic radiometry simulation. A Coupled Atmosphere-Fire Model is used to derive the parameters of the motion field and simulate fire dynamics and evolution. Broad band target (fire, smoke, and burn scar) spectra are synthesized based on ground measurements and MODTRAN runs. Combining the temporal and spatial distribution of fire parameters, along with the target spectra, a physics based model is used to generate radiance scenes depicting what the target might look like as seen by the airborne sensor. Radiance scene rendering of the 3D flame

includes 2D hot ground and burn scar cooling, 3D flame direct radiation, and 3D indirect reflected radiation.

Fire Radiative Energy (FRE) is a parameter defined from infrared remote sensing data that is applied to determine the radiative energy released during a wildland fire. FRE derived with the Bi-spectral method and the MIR radiance method are applied to verify the fire radiance scene synthesized in this research. The results for the synthetic scenes agree well with published values derived from wildland fire images.

Acknowledgements

I would like to acknowledge the many great people who helped me finish this body of work. My deep and sincere gratitude goes to my advisor, Dr. Anthony Vodacek. Your logical way of thinking has been of great value for me. Thanks for your years of inspirational instruction and guidance on academic issues. You granted me the freedom to pursue my ideas and your wise suggestions have been very valuable. Your door was always open to discuss any topic of interest.

I would also like to thank my committee members: Dr. Robert Kremens, Dr. Carl Salvaggio and Dr. Robert Teese who provided additional insight and took the time to read my dissertation. Thanks!

Many of my colleagues and friends assisted and encouraged me in various ways during my studies over the years. I am grateful to those who sat with me to discuss the matters related with my research and writing efforts.

Finally I wish to acknowledge the limitless support from my dear parents and husband, Wei. Without your stalwart love, faith, and support, this pursuit would not have been possible. I'm eternally indebt to you.

This work is dedicated to my parents and my husband Wei, for their endless love and encouragement throughout this venture.

Contents

List of Figures

List of Tables

Chapter 1

Introduction

1.1 Motivation

Why do we study wildland fire? As part of the natural environment, wildland fire is recognized as a significant global source of emissions that affects the climate. Biomass burning causes atmospheric gas and aerosol production as it consumes forest resources. As a major global source of many radiatively and chemically active species, the combustion of biomass releases significant amounts of trace gases such as CO, CH_4, NO_x, H_2O, and aerosol particles (organic matter, carbon and other constituents) into the atmosphere (Kaufman *et al.*, 1990). Additionally, biomass fire has instantaneous and longer term effects on the production of CO_2 and tropospheric ozone (O_3), which is a reactive oxidant involved in many photochemical processes (Bertschi *et al.*, 2003), contributing as much as 40% and 38% of each respectively in global scale (Levine *et al.*, 1995). Because fire alters the atmospheric transport of solar energy and the atmospheric gaseous composition, it is very important to the global environment. Increased fire ac-

tivity can lead to local air pollution and adds to the global greenhouse effect. On the other hand, biomass burning can also maintain the health of some tree species and forest ecologies that are adapted to frequent low intensity fires.

From perspective of most human activity wildland fire is very destructive. Monitoring and controlling wildfire is a particularly important and challenging charge. Knowledge of fire position, spread rate, and spread direction make it possible to effectively allocate resources for combating wildfires, thereby reducing cost and minimizing risk to life and property. If we can predict fire behavior with forecasting tools before any catastrophic situation really happens, it would further improve the efficiency and efficacy of fire fighting. "Recent advances in the field of fire science, along with the availability of high resolution remote-sensed satellite imagery, powerful image processing software, Geographic Information Systems (GIS), and affordable computer hardware" (Weinstein *et al.*, 1995) have enabled effective fire behavior simulation applications.

The purpose of this research is to integrate available information related to a wildfire in progress, convert a numerical prediction of the wildfire to a visual form, and reasonably simulate fire radiometry. The work includes the following parts:

1. Review the basic physical phenomena in fire that govern the gross behavior and understand fire properties from the perspective of remote sensing;

2. Measure and model visible to long wave IR emission and radiation from biomass burning and burn scars, as well as the time-temperature evolution of fire. These fire properties in turn, are key to the basic information required for fire prediction and management;

3. Take the physical output of a fire behavior model which tracks fire

and hot gases in the atmosphere, integrate the fire spectrum signature, time-temperature dependence and other measurements, provide input to a ray tracing tool, and develop a synthetic scene of a fire that is spectrally and spatially accurate;

4. Rather than 'pure' pixels, synthesized remote sensing pixels may be comprised of fire, burn scar, smoke, and wildland area background. We should be able to estimate the percentage of each end member within each pixel. This part of the work is performed using subpixel analysis with a spectral unmixing method;

5. Compare the completed spectral rendering with infrared images obtained from satellite or airborne platforms. This step aims at evaluating how exactly the radiometry is modeled and how well it could be improved. The physical model provides the data in a mesh format. The matching of the image data to the model grid is required for accuracy assessment.

One major goal of this work is that it should run in the environment of Dynamic Data Driven Applications Systems (DDDAS). DDDAS is a paradigm for applications and simulations. It entails the ability to incorporate additional data into an executing application and in reverse, the ability of applications to dynamically steer the measurement process (Darema, 2004). "The important feature of DDDAS is that the model is running all the time and it incorporates new data as soon as it arrives" (Mandel *et al.*, 2004a,b). DDDAS enables the control-feedback loop between application simulations and measurements. It fosters the capabilities of incorporating real-time dynamic data, enhancing or refining the original simulation model, and improving the understanding of the application. Having the ability to dynamically invoke the application models as needed by

the measurement input data, DDDAS provides the possibility of interaction of the application simulation with streamed input/resource data. This ability goes beyond the current concepts of real-time control.

The procedure is shown in Fig. 1.1. With this system, we will be able to build a bridge connecting the physical model output of fire propagation and the remote sensing scenes. This combination of model and image information could be utilized by fire manager for decision making and training sets producing for detection algorithm and sensor evaluation. Confidence in the radiometric accuracy of the synthetic scene is especially important when the image is used to train the detection algorithm.
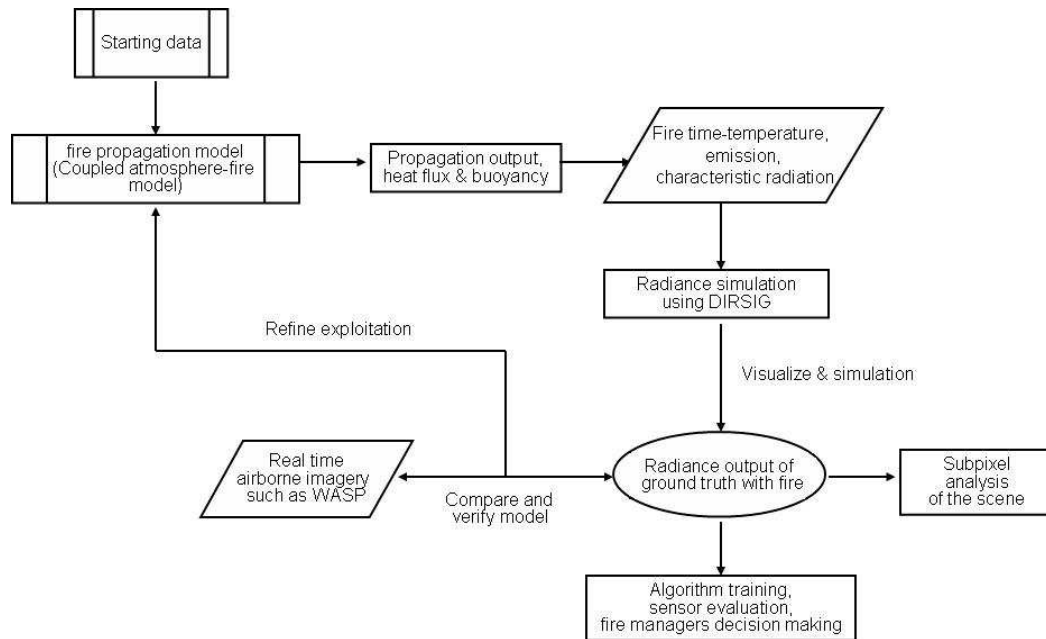
Figure 1.1: Flowchart of Dynamic Date Driven Application Systems for wildfire simulation

In DDDAS environments, we can 'integrate dynamically empirical fire spread

models with turbulence models representing the fire generated winds, together with up-to-date aerial survey and thermal sensor data and other information related to a wildfire in progress, and provide prediction of the course of the wildfire in visual form' (Mandel *et al.*, 2004b). The fire spread model should be able to execute multiple simulations at the same time and generate fire spread rates and directions, flame lengths, and fire line intensities. Remote imagery will give wide range coverage of elevation and ground radiance/reflectance for fire and fuels mapping. These real-time measurements will be feeding back to the physical model and keep adjusting the simulation, which will in turn give more accurate prediction of fire propagation. With this feature, we would be able to provide numerical fire behavior prediction in a visual form. The real-time measurement and prediction of fire behavior will increase the effectiveness and efficiency of fire management.

The other major application of this work is to use the synthetic image to test potential remote sensing systems and fire detection algorithms. It is notoriously difficult to establish ground truth of a fire because of the dynamic and destructive nature of fire. An accurate rendition of a fire scene will allow for flexibility in testing fire detection hardware and algorithms.

1.2 Overview of Physical Simulations of Fire

The fire is intrinsically partially transparent, volumetric, and dynamic. The left picture in Fig. 1.2 is the eternal flame in Arlington National Cemetery taken during the daytime. It is a relatively small and thin flame and we can partially see the stone and grass behind it. The main color of the fire is orange. The right image in Fig. 1.2 is close look at a much larger fire with strong radiation. It

Figure 1.2: Left: Small transparent flame. Right: Flame with complicate spacial structure.

is hot and very bright. The temperature variance makes the fire appear yellow, orange, red, and brown. Many spatial details are revealed at this scale. The flame doesn't have regular shape, and there are no smooth spatial distribution of points to track. In the fire there are extremely dense clumps, very hot and bright spots, and also, black voids. All of these result from turbulence in the fire and radiation and convection to the surrounding cold air, thus makes it complicated to simulate flame physically.

With respect to remote sensing, wild fire size and spread extension is of special importance in decision making. The scale of wildland fire varies considerably depending on the density and type of vegetation. Grass fires can reach 2 meters high, tree fires can reach the height of 20 meters, and crown fires can torch the crown as high as 40 meters or more. The head of some intense fires can even leap past the fire line and start new fires. The left picture in Fig. 1.3 shows some forest fire behavior. It is burning the grass, tree trunks, and may be torching crowns. Forest fires can burn very erratically, burning all fuel down to the mineral soil at one site while a few meters away a tree may be scorched on one side, but

still alive. With strong winds the immense smoke plume of an intense fire could blow over a long distance. The right picture in Fig. 1.3 is satellite imagery of a wildfire to the east of James Bay obtained by the Moderate Resolution Imaging Spectroradiometer (MODIS) on NASA's Aqua satellite in Quebec on June 1, 2005. The areas outlined in red are active fires. The smoke streams extended southeastward over 100 kilometers. This satellite observation of smoke plumes from wildfire reveals that the plumes could be traced intact for a long distance and helps illustrate the effects of fires on air quality.

Figure 1.3: Left: Forest fire. Right: Satellite imagery of wildfire from MODIS in Quebec, 2005.

Many approaches for developing a realistic model for simulating fire and its dynamics have been proposed. Fire dynamics models include the Fire Area Simulator (FARSITE) and Fire Behavior Prediction and Fuel Modeling System (BE-HAVE). These are operational models that could either be linked to other systems and databases or form the foundation of an integrated decision support system.

Some models based on fire physics described with differential equations (Asensio and Ferragut, 2002; Dupuy and Larini, 1999) allow numerical simulations at low computational cost. NCAR's coupled atmosphere-fire model tracks smoke and hot gases in the atmosphere. It is able to represent the complex interactions between the fire and local winds (Clark and Hall, 1995). The Fire Dynamics Simulator (FDS) solves numerically a form of the Navier-Stokes equations appropriate for low-speed, thermally-driven flow with an emphasis on smoke and heat transport from fires (McGrattan *et al.*, 2007).

Apart from fire dynamics models, finer scale simulations for visualization of fire structure has been developed within the computer graphics community. (Nguyen *et al.*, 2002) defines the flame front as a moving boundary between two fluids and an expansion term is introduced to add fine scale detail without using any randomized term. (Lee *et al.*, 2001) deposits emitters which could emit flame particles according to their internal state and simulates fire motion. (Wei *et al.*, 2002) proposes an open surface fire model which starts with fire particles, updates the velocity, and then projects the light onto surroundings. (Perry and Picard, 1994) simulates flames spread by modeling physically-based evolution of the boundary between burning and non-burning regions of polygonally defined objects. (Chiba *et al.*, 1994) generates 2D 'turbulence' as a vortex field which is defined as a composition of various vortices and as a function of time, then simulates the forms and motions of 2D flames by setting tracers free in the fire. These latter models are viewed as research models and are used for research computational experiments.

The importance of radiative heat transfer in the dynamics models suggests that the three dimensional (3D) flame structure in synthetic remote sensing scenes

of fire can be important aspect of the detected radiance and produce more accurate rendering than measurements of radiance considering only 2D ground thermal emission. There has been previous work on volumetric visualization methods to model fire as radiating volume. (Rushmeier and Hamins, 1995) uses line integration and ray casting to imaging fire data which is a stack of cylindrical rings. (Cunningham *et al.*, 2005) represents wildland fire of moderate intensity with circular heat sources and asymmetric elliptical ring heat sources and temperature and gas particle pressure are collected for each segment distance. (Stam and Fiume, 1995) uses a map covering the object to define the amount of fuel and temperature on every point on the object. Particle-based techniques have been quite popular for the animation industry. (Nguyen *et al.*, 2003; Reeves, 1983, 1985) present a fire as an evolving front and a system of particle-based flames, which has a 'fuzzy' shape instead of straight edges. (Lamorlette and Foster, 2002) creates a production model that combines a particle with a flame skeleton. (Henderson *et al.*, 2000) uses both gridless (particles) and grid-based computational data structures to simulate accidental fires and explosions. (Wei *et al.*, 2002) proposed the use of textured splats as display primitives for an open surface fire model. A texture splat is a small image of turbulence detail, can be generated from real images, from a noise function, or from a high-resolution detailed simulation of fire. However, in general it is not necessary to generate wildfire scenes with all of the fine details of flame texture because of practical limits to sensor spatial resolution.

In this research, the ray tracing submodel of DIRSIG is used for fire visualization and radiance prediction. The ray tracing model casts rays to the interested object/volume, collects radiometric information on its journey, and projects rays

onto the scene. To simulate fire dynamic activities, NCAR's coupled atmosphere-fire model is used. This model couples an empirical fire spread model (Rothermel, 1972; Mandel *et al.*, 2004b) with a 3D atmospheric prediction model (Clark and Hall, 1995; Clark *et al.*, 1996a,b; Coen *et al.*, 2001; Clark *et al.*, 2004), and tracks smoke and hot gases in the atmosphere. The solution is achieved by representing the field on regular 3D grid, rather than on unordered set of points. The fire Dynamics Simulator (FDS)(McGrattan *et al.*, 2007) from National Institute of Standards and Technology (NIST) was also used for comparisons of the spatial resolution, precision, computational consumption, and application area.

1.3   Overview of the Thesis

The rest of this document is organized as follows. In Chapter 2, the relevant physical properties of fire are reviewed. Chapter 3 further discusses the fire spatial and spectral characteristics from perspective of remote sensing. Chapter 4 describes fire characteristics measurements and visualization techniques. Chapter 5 introduces fluid dynamics models used in this research to simulate fire dynamics and evolution. Chapter 6 provides the results and the relevant discussions. Chapter 7 is devoted to conclusions and suggested future work.

Chapter 2

Fire Characteristics

Fire is defined intuitively as hot, luminous, and transparent gases. It is also characterized by its rapid and complicated combustion reaction.

2.1 Basic Chemical Properties

Fire is a source of light and heat. Fire can be explained at the molecular level as a set of chemical reactions. When fuel is heated, pyrolysis reduces the large fuel molecules to smaller fragments. Smaller fragments boil off, or say, volatilize, and transform into fuel gas. Since flame is a gas phase phenomenon, "flaming combustion of liquid and solid fuels must involve their conversion to gaseous form"(Drysdale, 1999). For vegetation fuel, when combustion temperatures are reached, gaseous carbon fuel will react with oxygen. This process splits the carbon bonds of the fuel to release the stored energy. Some of the energy heats soot particles which are incompletely burned fuel fragments, causing the soot to radiate heat and light. As expected, most of the biomass is composed of H, C, O

and N (by weight) (Bowen, 1979) :

    -C: 45%

    -H: 5.5%

    -O: 41%

    -N: 3.5%

The molecular combustion products are dominately these elements, e.g., H_2O, CO, CO_2, and NO_x. For any one of these small gas molecules, energy transitions occurs between two adjacent molecular vibrational levels. Interaction between these molecules and the external field takes place whenever absorbed or emitted energy equals to the energy difference of adjacent vibrational levels. The absorption or emission by a volume of gas will result in the depletion/increment of radiation of specific wavelength which is observed as an absorption/emission line in the spectrum. The wavelength range over which these molecules will absorb or emit radiation due to vibrational energy transitions is the near infrared to longwave infrared ($\sim 0.7\mu m$ - $20\mu m$).

    There are also large weight percentages of 'trace' elements in the vegetation fuel:

    -K: up to 7%

    -Na: 0.1%

    -Ca: up to 5%

    -P: up to 1%

When temperature of fire is raised further, alkali compounds are liberated and disassociate into alkali ions. Since the ionization potential and the jump to the first excited energy level of the alkalis is very low, for example, E_{io}=3.89eV for Cesium, E_{io}=4.34eV and $E_{1st\ ex}$=1.69eV for Potassium, E_{io}=5.39eV for Lithium

(Barnard and Bradley, 1985), they are easily excited and ionized. In a fire ions can be directly thermally excited to the first excited state. Excited states spontaneously decay to ground state by means of recombining electrons with ionized atoms. These processes are strongly dependent on temperature, total electron number density, ionization potential, and first excited state level. The excited ions "preferentially drop down to a pair of closely spaced, especially long-lived, interim states"(Hecht, 1998). These so-called *metastable states* are long lived states that are dipole-forbidden from decaying to the ground state (Lin, 1996). Metastable atoms are big, and have many internal energy levels. Since they are long lived, they can form in many plasmas.

Potassium and its emission are of special interest to remote sensing. Potassium is an essential constituent for plant growth and it is found in most soils. It is one of the most reactive and electropositive of metals. With atomic number of 19, its electron configuration is $1s^22s^22p^63s^23p^64s^1$. It is poorly electronegative and easily loses the outer electron and forms potassium ion K^+. Most of the potassium is in the ground state in a fire, very reactive and often forms strong ionic compounds to halogens. (Borovik *et al.*, 1999) measured the electron energy loss spectrum of potassium. Among the energy positions of peaks, the doublet $3p^54s^2\,^2P_{3/2,1/2}$ are the lowest auto-ionizing levels in potassium, which agrees with NIST Atomic Spectra Database that these two wavelengths are observed to have the highest emission energy level (National Institute of Standards and Technology, 2007). The metastable excitation/resonance transition from the first excited state to the ground state correspond to the emission doublet at 766.5nm and 769.9nm (Harris, 1980), which is a good choice for wild fire detection (Vodacek *et al.*, 2002). Sodium also has very strong resonance transition doublets from the first

excited state to the ground state and the strong emission in the yellow is widely used in road lamps, but the emission is not strong enough to be readily observed in a fire.

2.2 Phase of Combustion

There are three basic phases of combustion: pre-ignition, ignition, and combustion. *Pre-ignition* occurs as the water in the fuel in the area of applied heat boils off. The fuel is dried and partially pyrolyzed, and forms a flammable fuel cloud composed of flammable fuel gases, say, wood gases for a forest fire, and tar droplets. In the *ignition phase* applied heat causes the combustion reaction zone to form about the fuel cloud. Once it begins, the fire becomes self-sustaining and burns without an external heat source. "Many forest fuels burn initially by flaming combustion of fuel gases, followed by glowing combustion of fuel solids"(Cottrell, 1989). In *combustion phase* flaming combustion consumes the gaseous fuel. The flames preheat the adjacent unburned fuel which forms new flammable fuel cloud. The fire spreads as the cloud ignites. Flame dominates this phase. The flame dwindles and collapses without continuous flow of fuel gas. The collapsing reaction zone spreads out and initiates glowing combustion, in which the carbon appears reddish-orange. The heat of glowing won't ignite the fuel gases but will release carbon atoms locked in the fuel. "Glowing continues until it releases all the fuel carbons"(Cottrell, 1989). In the way of pyrolyzing and igniting a fire can be considered to some extent as a self-sustaining process.

In summary, the heat released is used to (i) raise fuel temperature to $100^o C$; (ii) separate bound water from the fuel; (iii) vaporize the water in the fuel; and (iv) heat the water vapour to flame temperature. The heat released is clearly a

very important characteristic(Wooster *et al.*, 2004) of a sustained fire.

2.3   Fire as Gas Volume

Fire could be either a small steady flame, or a large turbulent volume. In the work of (Drysdale, 1999) flames were examined when the fuel diameter is between 0.03 and 0.3m. The flames from this size of fire are essentially laminar, but become increasingly turbulent as the diameter is increased. (McCaffrey, 1979) showed that the 'fire plume' above a 30cm square burner consisted of three distinct regimes (see Fig. 2.1), namely:

(i) *flame zone*: a region above the burner surface, where there is persistent flame and an accelerating flow of burning gases;

(ii) *intermittent zone*: a region in which there is intermittent flaming and a near-constant flow velocity;

(iii) *buoyant plume*: is characterized by decreasing velocity and temperature with height.

While these are inseparable in the fire plume, it is appropriate to consider the buoyant plume on its own since its properties are relevant to other aspects of fire engineering, including fire detection and smoke movement. The term 'buoyant plume' is used to describe the convective column rising above a source of heat. Its structure is determined by its interaction with the surrounding fluid (the atmosphere).

Fire could be visualized as a bag filled with hot fuel gases, with oxygen surrounding the exterior. The structure of flame includes a fuel zone and a combustion reaction zone which is the yellowish bag wall in Fig. 2.2. With enough heating, fuel will volatize and transform into fuel gas. When fuel gas molecules
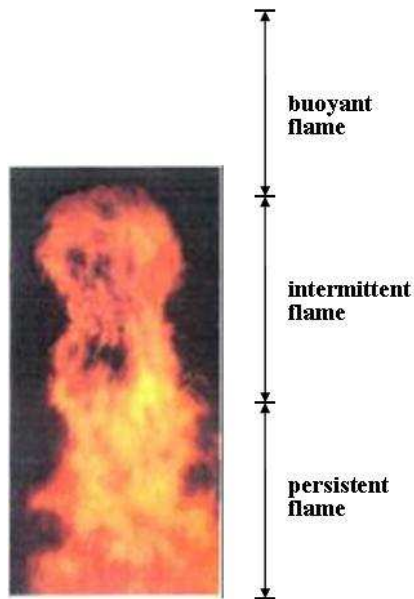
Figure 2.1: Schematic diagram of the fire plume showing McCaffrey's (1979) three regimes.

enter the combustion reaction zone, they react with oxygen from the surrounding air. Carbon bonds of the fuel split and release the energy, which forms the flame walls. By-products such as CO_2 and H_2O float away. Flame accompanies this reaction of fuel gas combustion. "Some fuel molecules avoid entering the reaction zone by collecting themselves together into snowball-like particles called soot"(Cottrell, 1989). The heated soot particles are black carbon particles. Soot absorbs energy from the reaction zone and radiates a yellowish to orange light with varying intensity, depending on the amount of energy they absorb. The soot particles may either enter the reaction zone or exit the flame body and immediately cool to black as soot smoke. If the combustion reaction zone fails, the flame generates black sooty smoke and dies. On the other hand, if the temperature and oxygen concentration are not high enough, the soot particles will tend to grow

in size and agglomerate to give larger particles which will escape from the high temperature environment of the flame as 'smoke'. When their size becomes of the same order as the wavelength of light (0.3 - 0.7 μm) they cause obscuration and reduced visibility by combination of absorption and light scatter (Drysdale, 1999). Smoke emitted by flaming fuel consists of two types: gray pyrolysis smoke from flame-radiated pre-ignition of unburned wood, and black sooty smoke from inside flame due to inefficient combustion. In most wildland forest fires the smoke consists of 50% soot and ash particles (Cottrell, 1989).
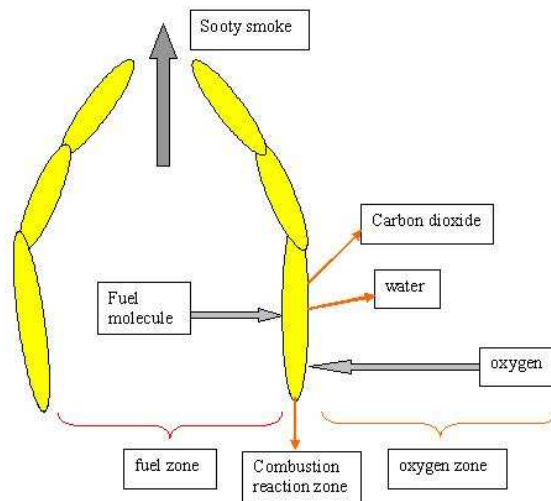
Figure 2.2: Reaction zone in the burning

The thickness of reaction zone includes each point in the luminous zone. Each point in the volume is a source radiating in all directions. Fire could be visualized as volume of radiating points or voxels, which will be discussed in Chapter 4.

The air immediately above a fire contains highly energized molecules of hot gas. The highly energized molecules, the yellowish block arrow in Fig. 2.3, push outward and upward into surrounding cooler air forming a lightweight "bubble"

of air. The surrounding cooler air, the white block arrow in Fig. 2.3, flows in
beneath the "bubble" to buoy it upward into the sky. The hot molecules rise
until they cool to ambient temperature. The in-drafts dramatically accelerate
the burn by providing oxygen, and the updrafts carry and disperse smoke and
ash high and widely into the atmosphere.
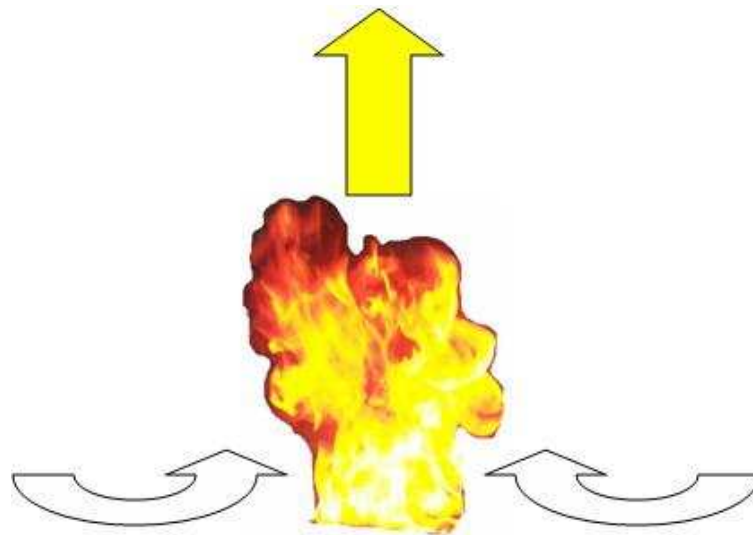
Figure 2.3: Hot air developed from the burning zone

2.4   Heat Transfer

An understanding of some physical processes helps to interpret fire phenomena.
These include heat and mass transfer. Heat is the energy output of the fire, and is
measured in units of Joules. What is usually of more interest is the rate at which
heat is released, not the total amount. The heat release rate (HRR) can thus
be measured in Joules per second, which is termed Watts. Since a fire puts out

much more than 1 Watt, it is usually convenient to quantify the HRR in kilowatts (1000 W) or megawatts (a million watts). There are three basic mechanisms of heat transfer: conduction, convection, and radiation. In addition to radiation by which energy is lost during combustion, other processes also take effect such as convection of the air mass above the fire and conduction into the ground (Asensio and Ferragut, 2002). "While it is probable that all three contribute in every fire, it is often found that one predominates at a given stage, or in a given location" (Drysdale, 1999). In most empirical fire spread models radiation and convection are taken into account as the dominant thermal transfer mechanism and the radiant energy loss is intense.

(a) *Conduction* is the transmission of heat associated with solid where there is temperature difference. It is important for ignition and spread of flame over combustible solids. The *heat flow* Q from region of high temperature to that of low temperature could be expressed as a heat flux q_x, which in one direction is given by:

$$q_x = -\frac{Q}{A} = -k\frac{\Delta T}{\Delta x} \tag{2.1}$$

where A is the transversal surface area; ΔT is the temperature difference over a distance Δx; k is the thermal conductivity in W/mK.

(b) *Convection* is the transfer of heat by currents within fluid. The motion of hot gases and the diffusion of eddies form the convection which causes the wind turbulence in and around the fire. Convection "occurs at all stages in a fire but is particularly important early on when thermal radiation levels are low"(Drysdale, 1999). The *local convective heat flux* of a fluid passing over a surface is expressed as

$$q' = h(T_s - T_\infty) \tag{2.2}$$

where q' is local heat flux; h is local convection coefficient; T_s is surface temperature, and T_∞ is quiescent or ambient temperature.

(c) *Radiation* is electromagnetic radiation from an object that is due only to the object's temperature. It requires no intervening medium between source and receiver. It will dominate the heat transfer in fires at high temperature. It generally provides the heat of gasification necessary to liberate the fuel volatiles from their solid state and is responsible for fire spread. The *total energy* emitted by a body is given by the Stefan-Boltzmann law:

$$E = \epsilon \sigma T^4 \tag{2.3}$$

where σ is Stefan-Boltzmann constant, $5.67 * 10^{-8}(W/m^2 K^4)$; ϵ is the emissivity of the surface; T is the temperature in Kelvins.

2.5 Fire as A Radiator and Its Radiance Characteristics

When considering fire heat transfer, "A substantial amount of heat released in flames is transmitted by radiation to the surroundings" (Drysdale, 1999). Much of the radiation is emitted by minute solid particles of soot which is the source of flame's characteristic yellow luminosity. So, fire can be considered as volume of emitting particles and is characterized in terms of temperature and chemical composition based on its spectra, which will be discussed in Section 4.4. The starting point for this is that the soot particles are close to blackbodies.

Simulation of remote sensing imagery containing fire relies on fire radiance

measurement which is useful in estimating the radiant-energy flux. So, the characteristic emitting radiation from fire should be understood. The starting point for this is that, fire is a good approximation to the blackbody, which is the perfect emitter and absorber of radiant energy with emissivity of 1. Note that this neglects the line emission of hot atmospheric gases that is observed at close range, because those line emissions are absorbed by the intervening cool atmospheric gases between a fire and a remote sensor. See Chapter 6 for example close range fire spectra that are dominated by the line emission of hot atmospheric gases. The Planck or blackbody radiation equation for the spectral radiant exitance from a surface is:

$$
M_\lambda = 2\pi hc^2 \lambda^{-5} \left(e^{\frac{hc}{\lambda kT}} - 1 \right)^{-1} \left[w/(m^2 m) \right] \tag{2.4}
$$

$$
= 3.75 * 10^{-16} \lambda^{-5} \left(e^{\frac{1.44*10^{-2}}{\lambda T}} - 1 \right)^{-1} \left[w/(m^2 m) \right] \tag{2.5}
$$

where h is the Planck constant, $6.63 * 10^{-34}(J/s)$; c is the speed of light, $3.00 * 10^8 (m/s)$; λ is wavelength in micrometers; k is the Boltzmann constant, $1.38 * 10^{-23}(J/K)$; T is the temperature specified in Kelvin; M has units of $w/(m^2 m)$.

The emissivity $\epsilon(\lambda)$ of a real surface is

$$
\epsilon(\lambda) = \frac{M_\lambda(T)}{M_{\lambda BB}(T)} \tag{2.6}
$$

where $M_\lambda(T)$ is spectral exitance from an object at temperature T, $M_{\lambda BB}(T)$ is the exitance from a blackbody at the same temperature. The emissivity is a unitless value and should within the range from 0 to 1. When emissivity $\epsilon(\lambda)$ equals 1, the object behaves like a real blackbody and emits maximum radiance. For some cases, when there are specific chemical compositions in the target, the

observed emissivity might be greater than 1.
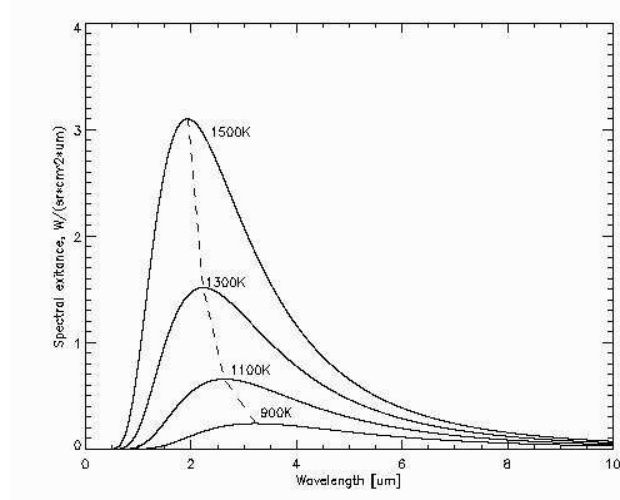
Figure 2.4: Blackbody radiation at different temperatures

The blackbody emits radiation in a range of wavelengths of varying intensities. The graph in Fig. 2.4 indicates the spectral radiant exitance from a surface at varying temperatures into 2π steradians. The shape of spectral radiance relates directly to the temperature. The peak wavelength varies inversely as the absolute temperature. As the blackbody becomes hotter, the total energy emitted increases and the wavelength of peak emission shortens, which is known as Wien's Law:

$$T = \frac{2898\,[\mu m K]}{\lambda_{max}} \tag{2.7}$$

If the flame is thick (L > 1m) and luminous, it is common to assume blackbody behavior, i.e., ϵ=1 (Drysdale, 1999). The emissivity was set to 0.96 (Kremens and Faulring, 2003) for radiative transfer estimation in this research. Heat transfer is partly convection and partly radiation. Depending on the emissivity, convection predominates at low temperatures ($150 \sim 200^oC$) but radiation becomes

increasingly dominant above 400^oC (Drysdale, 1999). This approach is applied to estimate temperature for a couple of planned fires. As the temperature is increased further, color changes are observed which are due to the changing of spectral distribution. By this method the blackbody's temperature could be estimated by examining its color. But the range of visual wavelengths is very small, and in many cases the objects emit strongly only at wavelengths longer than the visual spectrum. Thus we can sense the infrared radiation before it glows at wavelengths that we can see.

Flames are optically thin in the IR and spatially heterogeneous at scales from one to several meters (Riggan *et al.*, 2000). Experiments show in Chapter 6 that flame is transmissive in the NIR and becomes opaque only when it is thicker than at least 3 meters. The radiation emitted from the fire must pass through the intervening fire volume before reaching the detection system. The radiation is absorbed and re-emitted by molecular constituents of the flame and scattered into and out of the path by various fuel gas components or soot particles. The wavelength dependent volumetric attenuation follows an exponential relationship expressed by equation 2.8,

$$I_i(\lambda) = I_0(\lambda)e^{-k(\lambda)b_i} \tag{2.8}$$

where b_i is the path length of the sample, expressed in meters; k is the attenuation coefficient; I_0 is the irradiance from a small fire volume; I_i is the transmitted irradiance from the volume. The left figure in Fig. 2.5 shows the transmitted irradiance calculated with varied attenuation coefficients, $0.03m^{-1}$, $0.3m^{-1}$, and $3.0m^{-1}$. The transmitted irradiance decreases exponentially with path length within the fire volume. The plots in right figure in Fig. 2.5 are the accumulated
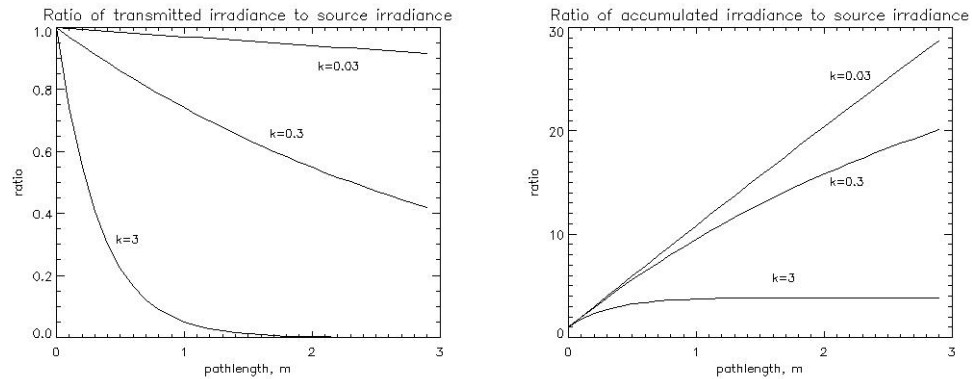
Figure 2.5: Left: ratio of transmitted irradiance along the observation path to source irradiance. Right: ratio of accumulated irradiance along the observation path to source irradiance.

irradiance from fire volume to observer. When the attenuation is $0.03m^{-1}$, the total transmissive irradiance increases almost linearly with the flame thickness. When the attenuation is $3.0m^{-1}$, there is no more increase of the total transmissive irradiance when path length is approaching 3 meters, thus flame appears opaque when it is thicker than 3 meters.

2.6 Spectral Signature of Fire

Remote sensing of the earth involves the capture and analysis of data from aerial or satellite imagery, which is helpful in monitoring and predicting wildfire. The technique that has long been used for fire detection is through the use of midwave IR and thermal IR sensors. The typical fire detection approach is to detect the Planckian radiation in the $3.5 \sim 5\mu$m and $8 \sim 14\mu$m. Since the wavelengths (>700nm) at which hot objects emitting radiation are much longer than the size of smoke particles, it is possible to see through the smoke and get

more information from the actual fire in an IR image. However, there are a large number of other sources giving off heat or reflecting radiation that could cause false alarms.

The overall shape of fire radiance spectra is blackbody-like curve, as discussed in section 2.5, modified by atmospheric absorption and particularly by scattering in the visible spectrum. These are also molecular and atomic emission lines in addition to the Planck-type radiation as will be discussed in Chapter 3.

2.7   Diffusive Wildfire Flame

Most flames in a fire are *diffusion flames*. The principle characteristic of the diffusion flame is that the fuel and oxidizer (air) are initially separate, the oxidizer combines with the fuel by diffusion, and combustion occurs in the zone where the gases mix. If ignited, the mixture will burn wherever the concentrations of fuel and oxygen are within the appropriate (high temperature) flammability limits. The flame speed is limited by the rate of diffusion. Diffusion flames provide a convenient way to examine strained flames and flames with holes.

In *pre-mixed flame* the oxidizer had been intimately mixed with the fuel before it reaches the flame front (ignition), flame propagation through the mixture is a deflagration (e.g., smoke explosion). This creates a thin flame front as all of the reactants are readily available. If the mixture is rich, a diffusion flame will generally be found further downstream. Examples of a laminar pre-mixed flame are Bunsen burner flame and gas stove. Turbulent pre-mixed flames are generated from engineered combustion systems such as boiler and furnace. The flame speed is dominated by the chemistry. The flame front is decided by the flow rate.

Diffusion flames tend to burn slower and to produce more soot than pre-

mixed flames because there may not be sufficient oxidizer for the reaction to go to completion. Diffusion flames tend to have a less-localized flame front than pre-mixed flames.

Wildfires fall into the category of turbulent diffusion flames, since no burner or other mechanical devices existed to mix fuel and air (oxidizer). Diffusion flames have relatively low intensity. The fuel might be cracked to soot before the oxygen reaches it to generate the heat. The small visible and huge infrared radiation cools the flame. The heat is only generated at the fuel-air interface envelope which has a large surface area. Pre-mixed flame burns all the fuel at the flame front in a layer less than 0.1mm thick, where there is more available heat, higher combustion efficiency, higher flame intensities. If a wildfire approaches a pre-mixed condition, stronger radiance will be observed. There will be less aerosol and smoke. But it is impossible to expect consistent pre-mixed conditions where the biomass volatilized into gas, mixed with air, and then burned. Thus biomass burning never has the same combustion efficiency as chemical gases such as propane.

The properties of wildland fire as diffusion flames in very important to describing fire behaviour in the environment.

2.8 Importance of Wildfire Spread Prediction

Having knowledge of fire behavior is the most efficient way for fire managers to establish procedures for controlling a wildland fire. Research scientists and forest resource managers have long been seeking the ability to model wildfire behavior including its spread. Given local conditions such as terrain, fuel type, weather, and wind, fire growth models will generate detailed data regarding fire behavior,

such as heat, rate of spread, and flame scale of burning area. We could further convert these data to fire maps and fire line intensity data which will likely make it easier for forest fire managers to access for operational planning. Through the incorporation of GIS technology, laboratory findings, and remote sensing imagery, fire behavior models are calibrated from past fires to predict the spread rates and directions, flame lengths, fire line intensities, and give more precise prediction of fire position and propagation.

To provide a reasonable explanation of observation of wildland fire and achieve successful forecasting of fire propagation, the mechanism of flame propagation should be understood. (Viegas, 2004) suggests that "radiation from the flame or from the reaction zone inside the fuel bed may be the major heat transfer mechanism responsible for the advance of the fire front". In wildland, there are many other factors that are important in determining the spread rate of fire, like terrain (especially slope), fuel content, wind speed and direction, humidity, temperature, etc. The moisture content of the fuel depends on the weather as well as the type of vegetation. For example, coniferous trees are generally much more flammable than deciduous trees because coniferous trees contain larger amounts of flammable chemicals (resins). These factors are interdependent and have complex interactions resulting in a wide range of fire behavior. As measured by Canadian Forest Service, crown fires can spread at up to 100 meters per minute, and the fastest grass fires have been clocked at over 300 meters per minute.

Current wildfire growth models differ in complexity and origin. They are appropriate for different applications such as training, prediction, and risk assessment. The applications are based on the environmental conditions of the modeled fires, and how urgent the output from model is required. Since fire

prediction is so time-critical, unlike some other applications, fire managers and fire fighters need faster-than-real-time output from simulation. Besides the coupled atmospheric transport/wildfire behavior model FIRETEC (Linn *et al.*, 2002; Linn, 1997), there are other fast-running operational models like Fire Area Simulator (FARSITE) (Finney, 1998) and Fire Behavior Prediction and Fuel Modeling System (BEHAVE) (Grabner *et al.*, 2001). These models are validated for simple scenarios. They can simulate burning conditions before potentially catastrophic situations really happen. By applying these wildfire behavior models to environmental conditions, we'll have some idea of how large a certain fire might be and its potential for movement.

2.8.1   Biomass Fuel Characteristics

Fire will spread most rapidly through grass at ground level or through the forest crown, which is an extreme fire behavior. Fire spreads relatively slowly in wet and living fuel since fuel must be dried and heated to fire point before burning. The heat is transferred ahead of the flame front to unburned fuel by radiation and convection. The rate of fire spread will increase as temperature of fuel increases. It is expected that the higher the initial fuel temperature the less heat is required to ignite the unaffected fuel ahead of the flame.

2.8.2   Environmental Factors Affecting Fire Spread

(i) *Terrain Effect*

Terrain orientation also plays an important role in fire propagation. The reason for this lies in the fact that physical interaction between the radiating flame and unburned fuel changes as terrain slope varies. Let's take a look at

how fire interacts with the surrounding trees in the forest. In Fig. 2.6 flame (a) preheats only a few trees at any time by radiation. The fire spreads relatively slowly. Flame (b) is on the hillside. It can preheat many more trees above and a more rapid rate of upward spread can be expected. The fire might look like it's 'running' up the slope. Flame (c) is at the top of the hill. It still radiates but affects no trees. It will use out any available fuel rapidly and die out. Many wild fires die on mountain tops.
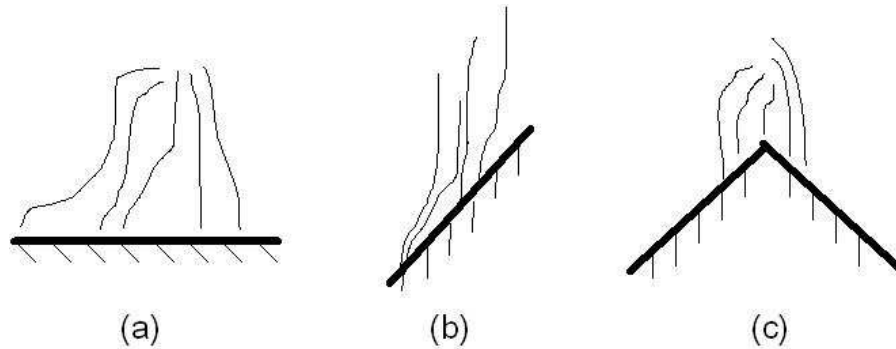
Figure 2.6: Interaction between the flame and terrain at different angles of inclination.

(ii) *Wind Effect*

Wind tends to increase the combustion within the flame. Wind direction and speed information suggest areas where fire is likely to propagate after it starts. When surface wind blows, the fuel cloud caused by fire preheating concentrates on the downwind side of the fuel. The fuel cloud ignites and becomes new fire front. Without wind, the point ignition will spread almost equally in all directions and form a round or elliptical fire front. When there is wind, the heading fire front spreads rapidly in the direction of wind. The backing fire front, by radiation and convection, will slowly creep into the wind. The side fire front, or flanking, also

spread in the direction of wind. Air movement also influence the directional flow of air/flame and a rule commonly used is that a $2m/s$ wind will bend the flame by $\theta = 45^0$ (Ris, 2002).

2.8.3 Time-temperature of Fire and Burn Scar

Time-temperature measurements of flame and burn scar are useful in fire propagation prediction, as well as burned area and damage evaluation. According to Canadian Forest Service measurement, the maximum temperature in forest fire flame is between $800{\sim}1000^oC$. (Kremens and Faulring, 2003) made measurements and determined the length of time the burn scar remains visible to mid and long-wave infrared sensors for different ecosystem types. In their measurement, ground temperature during a bright sunny day can reach ${\sim}40\text{-}50\ ^oC$.

The temperature of fire front measured by thermocouples in contact with soil surface can reach as high as 800^oC, and decays exponentially with a single time constant of about 100 seconds ($1/e$ time).

$$T_t = T_0 e^{\frac{-t}{\tau}} \tag{2.9}$$

Where T_0 is the maximum temperature of fire front, 800^oC; τ is time constant, 100 seconds, which is selected to best fit the temperature drop curve. After certain period of time, the burned area temperature drops to ambient temperature with $+/\text{-}2^oC$ variation, see Fig. 2.7.

Since the high-temperature flaming front is generally transient in mid and long-wave infrared, the burn scar may be observable for a significantly longer time than the flaming front. The burn scar usually has high emissivity (0.9
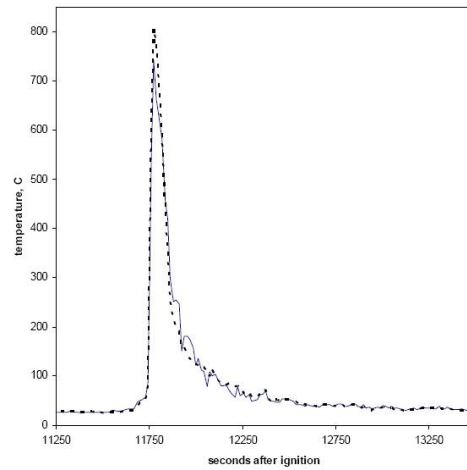
Figure 2.7: Time-temperature measured by thermocouples in contact with the soil surface. Dotted and solid curves are from two thermocouples 1 m apart. Image courtesy of Robert Kremens, 2003.

according to (Kremens and Faulring, 2003)) and radiates significant power even though the temperature of the scar is much lower than the flame temperature.

Chapter 3

Remote Sensing of Wildfire

3.1 Wildland Fire Emission

Remote sensing of wildland fire is performed by analyzing reflected or emitted radiance spectrum (Rizzi and Saunders, 1998; King *et al.*, 1992; Salvador *et al.*, 1998; Fraser and Li, 2002; Richards and Jia, 1998). The unique spectral signatures of fire arise from a variety of phenomena related to the fire itself, particles, and gases produced by the fire, or changes to the vegetation. These remotely detectable signatures can be used to provide a comprehensive understanding of pre-fire, fire, and post-fire effects in the environment. (Li *et al.*, 2000) developed a spatially and temporally explicit model to estimate forest fire emissions. (Longo and Freitas, 2006) calculated the mass of the emitted tracer for each detected fire pixel and then estimated the burned area. (Kaufman *et al.*, 1996) introduced the concept of remotely measured Fire Radiative Energy (FRE) to estimate the biomass combustion rates and the associated emissions. (Wooster *et al.*, 2003) presents the remote determination of FRE by analyzing pure or mixed fire pixel

radiances in the middle infrared spectral region because of fire's strong infrared thermal emission signal.

3.1.1   Trace Gas Components

Trace gases could be very useful for fire detection and evaluation. (Kaufman *et al.*, 1990) build a relationship between observation of detected fires and remote sensed emitted particles, and trace gas emissions, then estimate the total amount of particulates emitted, and further derive fire severity and change in the atmospheric balance.

Biomass matter is mostly carbon, most of the remainder of the biomass matter is water. During the flaming stage a combustion products like water (H_2O), carbon monoxide (CO), carbon dioxide (CO_2), ammonia (NH_3), methanol (CH_3OH), formic acid (CH_2O_2), ethylene (C_2H_4), methane (CH_4) (Worden *et al.*, 1997; Dennison, 2006), and nitrogen oxidants NO_x are released into atmosphere along with smoke aerosol emitted from fire. The moisture contained in the biomass and water generated through combustion can make a small increase in the relative humidity of the smoke. Most of the water vapor in the smoke was in the ambient air before fire. Therefore, the effect of water vapor on aerosol scattering characteristics depends on the atmospheric profile of the relative humidity and the altitude of the smoke(Kaufman *et al.*, 1990). Gaseous emission and absorption from high concentrations of CO_2, CO and H_2O may change the remote sensing scene at some specific wavelengths and be useful in detection methods(Kremens, 2001b). Unique combinations of gas signatures are possible using infrared detection techniques. There are wide and strong water emission centered on 6.5μm and 1.5μm. CO_2 has spiky emission at 2.6μm and 15μm. There are strong vi-

bration bands of $^{12}CO_2$ centered on $2349cm^{-1}$ and $^{13}CO_2$ at $2283cm^{-1}$(Goody, 1995), which are $4.26\mu m$ and $4.38\mu m$ respectively and could be seen with high spectral resolution data.

There are also CO_2, CO, CH_4 and particulate matter emissions from burn scar (post-fire residues). Traditionally CO/CO_2 or $CO/(CO+CO_2)$ ratios have been used to indicate combustion efficiency (Cofer *et al.*, 1998).

3.1.2 Atomic Line Emission

There are many fire physical parameters relevant to remote sensing of fires. Besides fundamental physical parameters such as emissivity ϵ, area, and temperature T, there are molecular line emissions including sodium Na, phosphorus P, and potassium K. These elements are major constituent by weight of plant fuel material (Kremens, 2001a). Sodium Na has obvious emission in visible band 588.995nm and 589.592nm in road lamp spectrum and makes it yellowish. But Na emission is not strong enough to be observed in a fire. Phosphorus P has relative strong emission from ultraviolet to visible and could be observed if the sensor has wide enough spectral coverage. Potassium K has very strong resonance transition doublets emitting at spectrum 766.490nm and 769.896nm (National Institute of Standards and Technology, 2007), which can be very good candidate for fire detection (Vodacek *et al.*, 2002). Fig. 3.1 compares the wildfire imagery to result from band ratio. The lower left image is the Airborne Visible/Infrared Imaging Spectrometer (AVIRIS) imagery of wildfire in Brazil, 1995. The imagery spectral dimension extends over $0.38\mu m$ to $2.5\mu m$. The spectrum of fire pixel shows strong K emission. The lower right image shows fire areas extracted by taking band ratio band44/band43 where the K signal is present in band 44 and absent

in band 43.

Figure 3.1: Upper: Spectrum of fire pixel. Lower left: AVIRIS imagery of band 43 (749.57nm), Cuiaba, Brazil 1995. Lower right: ratio of band 759.12nm to band 749.57nm.

3.1.3   Spectral Broadening

Section 3.1.2 discusses spectral line emission from biomass fire. The shape of individual spectral line, narrow or broad, shallow of deep, contains a wealth

information about the environment in which it was formed. The width of a spectral line is one such measurement. The transitions in spectra cannot be infinitely 'sharp', thus there is always a finite width to the observed spectral lines. Three main processes are responsible for the broadening of spectral lines: natural broadening, thermal Doppler broadening, and pressure (and collisional) broadening.

(i) *Natural Broadening*

According to Heisenberg's uncertainty principle,

$$\Delta E \approx \frac{h}{\Delta t} \tag{3.1}$$

the energy of the states involved in the transition cannot have a precise value due to the uncertainty of time interval over which energy is measured. Natural broadening arises from these uncertainty in energy levels involved in the transition. Electrons can make transitions from and to any of the 'fuzzy' energy levels and produce an uncertainty in the wavelength of the photon absorbed or emitted in a transition(Ostlie and Carroll, 1996). The uncertainty in the photon's wavelength has a magnitude of roughly

$$\Delta \lambda \approx \frac{\lambda^2}{2\pi c}\left(\frac{1}{\Delta t_i} + \frac{1}{\Delta t_f}\right) \tag{3.2}$$

where Δt_i is the lifetime of the electron in its initial state and Δt_f is the lifetime in the final state. A more involved calculation shows that the full width at half-maximum of the line profile for natural broadening is

$$(\Delta \lambda)_{1/2} = \frac{\lambda^2}{\pi c}\frac{1}{\Delta t_0} \tag{3.3}$$

(ii) *Doppler Broadening*

Thermal Doppler broadening is due to the temperature of the emitter or absorber. In a gas, any particular/individual atoms, elements or molecules are continuously moving in random directions, with an average speed proportional to the temperature of the gas.

$$\frac{1}{2}mv^2 = \frac{3}{2}kT \tag{3.4}$$

where m is the mass of an atom. Compare to a stationary observer, any particular/individual atoms, elements or molecules could be moving along the line-of-sight, perpendicular to the line-of-sight, or some combination of both. This means that energy spectral line emitted is Doppler shifted relative to the observer, resulting in a small change in the observed wavelength. This spreading of a spectral line due to the temperature of the emitting medium is called 'thermal Doppler broadening'. Emission lines become broader as gas temperature rises and motions increase. The full width at half-maximum of the line profile for Doppler broadening is:

$$(\Delta\lambda)_{1/2} = \frac{2\lambda}{c}\sqrt{\frac{2kT\ln 2}{m}} \tag{3.5}$$

Although line profile for Doppler broadening is much wider at half-maximum than for natural broadening, the line depth for Doppler broadening has much faster falloff in strength than for natural broadening.

(iii) *Pressure (and collisional) Broadening*

The orbitals of an atom can be perturbed in a collision with a neutral atom or encounter with an ion electric field. The values of the full width at half-maximum for pressure broadening can at times be more than an order of magnitude wider than natural broadening (Ostlie and Carroll, 1996). The width of the spectral

line due to pressure broadening is on the order of

$$\Delta\lambda \approx \frac{\lambda^2}{c} \frac{n\sigma}{\pi} \sqrt{\frac{2kT}{m}} \tag{3.6}$$

where σ is the collision cross section, n is the number density of the atoms.

Spectral broadening can be used to detect fire using AVIRIS data because the line emission of the hot atmospheric gases in the fire is wider than the line absorption by the cooler atmospheric gases between the ground and the sensor. The lower right image in Fig. 3.2 is the difference between band 168 and band 164 where fire pixels have larger band gap than the background pixels.

3.1.4   Smoke in Wildfire Observation

When vegetation transforms into fuel gas with enough heating, it starts to participate in the process of combustion. Some fuel molecules collect themselves together into snowball-like particles which are called soot. The heated soot particles are black carbon particles. Black carbon is a high-temperature flaming product (Cofer *et al.*, 1998; Kuhlbusch and Cruzen, 1996) which may exit the flame body through an inefficient combustion and immediately cool from orange to blackness as soot smoke.

Smoke aerosol emanating from forest fires is often difficult to visually distinguish from cloud cover (Li and Cihlar, 1999). Smoke and cloud have subtle differences in their reflectance and emission in the visible. High molecular weight tar components in smoke are grey bodies. They are heated by the radiation field from the combustion process and emit in the infrared. The water droplets and aerosol particles that make up the smoke are much larger than the molecules

of the air and the scattering from them is almost independent of wavelength in the visible range. Mie scattering predominates in this case and gives the white to achromatic gray color from smoke. Without scattering, we can't 'see' the medium the rays transpass. Analysis of AVIRIS data shows that at visible wavelengths the light is diffused by smoke particles and there is no smoke penetration; we can't see fire through the smoke from space. In the NIR region, scattering doesn't dominate, less of the light is scattered by the smoke and bright active fire fronts are visible. At longer wavelength, say, 1500nm, the infrared radiation passes through smoke with little attenuation, thus burning fire signals are strong and could be easily identified.
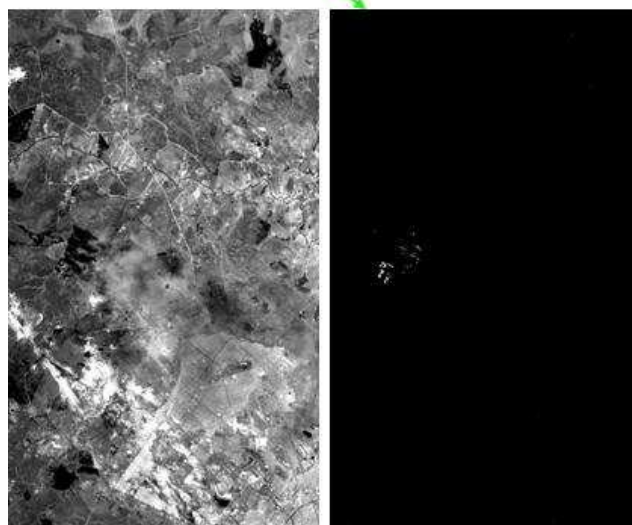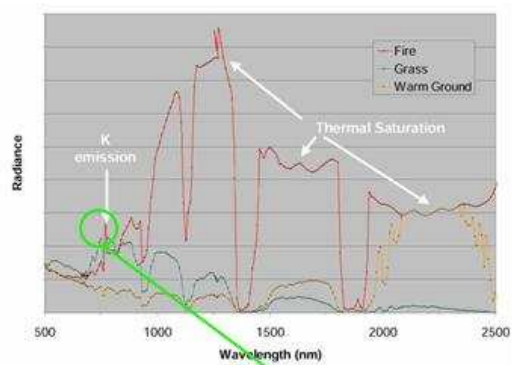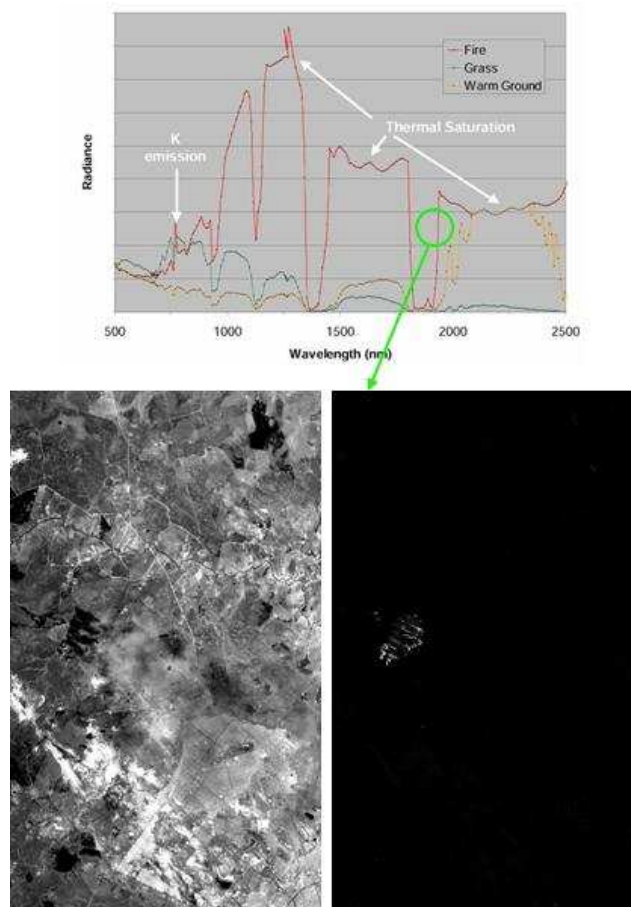
Figure 3.2: Upper: spectrum of fire pixel. Lower left: AVIRIS imagery of band 43 (749.57nm), Cuiaba, Brazil 1995. Lower right: difference of the band at 1951.37nm and the band at 1911.15nm.

3.2 Role of Remote Sensing and Image Processing for Fire Management

There is global interest in monitoring fire regimes. People want to determine the spatial extent of the entire fire as accurately as possible. Remote sensing is the most appropriate technique for a global perspective on the large scale spatial and temporal distribution of biomass burning (Levine *et al.*, 1995). Remote sensing can track wildland fire perimeters, hot spots, and the advance of fires using thermal IR imagery from manned or unmanned airborne platforms (Radke *et al.*, 2000; Vodacek *et al.*, 2002; Mandel *et al.*, 2004a) for cases where a fire location is completely obscured to naked eyes by smoke. It can accurately quantify the burned area on a global scale by measuring fire scars from space. The advancement of remote sensing technologies and capabilities, including the use of satellite and/or aircraft imagery, may provide comprehensive information of fire over wide areas.

Standard gain and offset coefficients are applied to satellite or aircraft imagery to transform digital readings to radiance. By applying radiometric atmospheric corrections reflectance could also be obtained. With appropriate calibration, remotely sensed images can be applied to a variety of fire applications. For example, time-series of calibrated infrared imagery captured over a fire can be analyzed to determine the total heat released (Kremens, 2001a). Further, to retrieve valuable information on the fire regime and to evaluate plant regeneration rates in plant communities, Normalized Difference Vegetation Index (NDVI) post-fire values are used.

This work will establish the relationship between remote sensing related fire

properties such as radiance, transmission, optical emissivity of aerosol and trace
gases, burn scar growth, and physical modeling of heat, buoyancy, and tracers.

3.2.1   Applications of Remote Sensing to Wildfire Management

(i) *Fire Fighting*

Real-time imaging of fire extent and spread, which is the most important
information from a fire-fighting perspective, usually employs infrared detectors
(smoke won't obscure in these bands). Maps of fire extent, temperature, and
fire front could be generated from airborne sensors. Some airborne imagery can
also provide region-wide coverage of smoke plume and information on extent of
smoke and ash deposition. Fire managers could make decisions based on these
most current information available. Satellite sensors are usually not operationally
employed because of low spatial and temporal resolution.

Monitoring fires and smoke simultaneously by remote sensing was suggested
by (Kaufman *et al.*, 1990). (Brenner *et al.*, 2005) utilized a GIS based fire risk
assessment system to assist fire managers to mitigate the harmful effects of wild-
fire and plan for fuel reduction efforts. After obtaining knowledge of fire position
and the spread, decisions on deploying fire fighters or aerial fire fighting planes
can be made. Fig. 3.3 shows the fire fighter fighting with the forest fire and the
fire plane dropping flame retardant trying to stop a line of fire.

The visualization of remote sensing data and fire behavior models play a
significant role in the way in which fire managers approach wildfire suppression,
public outreach, and recovery efforts.

(ii) *Post-fire Assessment*

Figure 3.3: Left: Fire fighters are fighting forest fire. Right: A fire-fighting plane drops flame retardant in California to try to stop a line of fire

Forest managers require a quick and complete assessment of the damage impact following a forest fire. Territorial conditions such as soil and vegetation resources and the location and degree of the damage becomes necessary. High altitude aircraft and polar orbiting satellites can provide moderate resolution images from visible to IR to map burn scar and its severity. Besides the mapping of fires and fire scars, the role of fires in affecting carbon and water cycles could also be assessed by these images.

Caused by changes in canopy cover, biomass removal, moisture, and soil chemical composition, burn severity can be detected and mapped using Landsat Thematic Mapper (TM) data. There are numerous works (Salvador *et al.*, 2000; White *et al.*, 1996; Miller and Yool, 2002) in which LANDSAT scenes are used for mapping the burned area and classifying burn severity. It was shown that mid-infrared bands of Landsat TM (Band 5: 1.55-1.74μm, Band 7: 2.08-2.35μm) contribute new information for classifying burn severity (White *et al.*, 1996), and Landsat-5 spectral channel 4 is the best to identify fire scars. Normalized Difference Vegetation Index (NDVI) indices could also be derived from Landsat 5

to evaluate vegetation cover, which can be very useful in making decisions for restoring vegetation in the affected area.

3.2.2   Sensors Used in Fire Monitoring

The means for wildfire monitoring include satellite remote sensing and airborne remote sensing.

Remote sensing imagery offered by meteorological, oceanic and earth observation satellites have been utilized in various studies related with environmental sciences. Among these satellites the earth observation satellites are used widely in global scale studies including fire observation and monitoring, as well as longer term mapping of fire boundaries in many areas. With this information, we can analyze spatial patterns of fires and analyze their consequences. The selection of the proper sensor should be based on the spectral sensitivity of the available sensors, the availability of atmospheric windows in the spectral range of interest, and the interaction of energy with the features under investigation. The sensors with spectral bands encompassing MIR region ($3\text{-}5\mu m$) and which are capable of making unsaturated measurements over high intensity targets, are optimum for the remote determination of fire (Wooster *et al.*, 2003). Besides spaceborne sensors, there are terrestrial and airborne remote sensing missions which have been utilized in monitoring fire and providing data on fire position:

(1) *Advanced Very High Resolution Radiometer (AVHRR)*
AVHRR is carried on board the National Oceanic and Atmospheric Administration (NOAA) series of satellite. The AVHRR five channel scanning radiometer with 1.1-km resolution is sensitive in the visible, near IR, and IR regions, thus offers the opportunity for a global fire-monitoring system and global data sets on

fire emission characteristics. AVHRR images can be used to identify potential fire pixels using their strong thermal response in mid-infrared channel (3.7μm) (Li *et al.*, 2000), and trace the accompanying smoke plumes with the visible channels. It is helpful in mapping burned area on daily and annual basis (French *et al.*, 1996; Cahoon *et al.*, 1992).

(2) *Moderate Resolution Imaging Spectrometer (MODIS)*

MODIS is carried on board the Earth Observing System (EOS) satellite series. It was designed with 36 spectral channels for a wide array of global investigations. MODIS data covers the visible, near-infrared, shortwave, and thermal infrared spectral bands of the electromagnetic spectrum. MODIS has unique ability to observe a suite of fire related products: active fires, smoke, and burn scars. It can distinguish between low intensity ground surface fires and high intensity crown forest fires. Burn scars could also be observed in the presence of smoke. (Kaufman *et al.*, 2003, 1998) utilized 4μm and 11μm channels of MODIS to monitor global fire with 1km resolution, and observe burn scars in mid-infrared channels ranging from 1.2 to 2.1μm, at which smoke is transparent.

(3) *Operational Linescan System (OLS)*

OLS is carried on the Defense Meteorological Satellite Program (DMSP) Block 5 series satellites. It consists of high-resolution scanners that produce visible and infrared spectrum photographs, can obtain long running nighttime global imagery.

(4) *Visible Infrared Spin-Scan Radiometer (VISSR)*

VISSR is an imaging device used for two-dimensional, cloud cover pictures from a geosynchronous altitude. It provides both day and night time observations of clouds and the determination of temperatures, cloud heights and wind fields. It

has 1-km resolution. A VISSR instrument flies aboard the Geostationary Meteorological Satellite (GMS, Japan), the Meteorological Satellites (Meteosat, European Space Agency), and the Geostationary Operational Environmental Satellites (GOES, USA) which provide hourly information about smoke from its visible channel.

(5) *Hot Spot Recognition Sensor (HSRS)*

HSRS is a two-channel (MWIR and TIR) infrared push-broom imaging instrument. Carried on board the Bi-spectral InfraRed Detection (BIRD, Germany) small satellite, HSRS was especially developed for the recognition and quantitative estimation of thermal processes such as active fires.

(6) *Along Track Scanning Radiometer (ATSR-ERS1)*

The ATSR instruments fly aboard the European Remote Sensing Satellite (ERS-1). ATSR produces infrared images of the Earth in wavebands 1.6, 3.7, 11 and 12 μm at a spatial resolution of one kilometer.

(7) *Advanced Along-Track Scanning Radiometer (AATSR-ERS2)*

The AATSR is a space-borne instrument with four SWIR-TIR wavebands (1.6, 3.7, 11 and 12 μm) and four VIS-SWIR bands (0.65, 0.85, 1.27, and 1.6μm), which ensures the production of a unique 10 year near-continuous data set at the levels of accuracy required (0.3 K or better).

(8) *Thematic Mapper (TM) and Enhanced Thematic Mapper (ETM)*

TM and ETM were carried on board Landsat series satellites. The Landsat Program is a series of Earth-observing satellite missions providing repetitive coverage of continental Earth surfaces in the visible, near-infrared, short-wave, and thermal infrared regions. It is very useful in mapping burned area and classifying burn severity.

(9) *Airborne Visible/Infrared Imaging Spectrometer (AVIRIS)*

AVIRIS is a unique optical sensor that delivers calibrated images of the upwelling spectral radiance from 400nm to 2,500nm. The spectra are acquired at 20m spatial resolution from aircraft flying at 20-kilometer altitude. It is used to gather valuable information on wildland fires which exhibits characteristic emission, absorption, and scattering characteristics that AVIRIS is sensitive enough to detect. AVIRIS is so sensitive that it often exhibits saturation of fire pixels. Radiance is measured in units of $mW/(cm^2 * nm * Sr)$ or $\mu W/(cm^2 * nm * Sr)$.

(10) *Phoenix system*

The Phoenix system is an airborne thermal infrared wildland fire detection and mapping system developed by the United State Department of Agriculture (USDA) Forest Service. Two thermal infrared detectors are utilized to provide thermal detectability, one in the $3 \sim 5\mu m$ band and the other in the $8 \sim 14\mu m$ band. With a typical air speed of 200 knots and a height above ground of 3,000 m, an area of 6,515 hectares can be covered in one minute with an overall resolution of 6.3 m/pixel. Within this area, Phoenix automatically detects fire spots that are 15-20 cm in size. This coverage area is 40.5 sq km per minute.

(11) *Wildfire Airborne Sensor Program*

RIT developed an aircraft sensor, WASP, for fire monitoring. WASP is an airborne sensor system for day/night multi-spectral wildfire detection and mapping. WASP incorporates SWIR ($0.9 \sim 1.8\mu m$), MWIR ($3 \sim 5\mu m$), and LWIR ($8 \sim 11\mu m$) cameras and a very high spatial resolution panchromatic visible camera. WASP was specifically designed as a conceptual design for replacement of the line scanners currently employed by the US Forest Service. WASP enables reliable fire detection with a low false alarm rate.

Chapter 4

Approach

The ultimate goal of this work is to add to the comprehensive suite of fire behavior modeling and prediction tools for more effective use by wildland fire managers. The approach is to combine measurements of fire phenomena with synthetic image generation and atmospheric transmission models to realistically visualize wildland fire.

One major goal is to perform volume visualization of large-scale wildfire using the Digital Imaging and Remote Sensing Image Generation (DIRSIG) model, which will be introduced in Section 4.2. Since DIRSIG requires input spectra for target modeling and there are relatively few published spectral measurements of fire, a set of spectroradiometric measurements of fire were made at the US Forest Service Fire Science Laboratory and at RIT to aid in DIRSIG modeling. These experiments are described in Section 4.1. Another major goal is to correctly model the radiometry of fire which is observed from an airborne or spaceborne sensor. This is completed in part with the Moderate Resolution Atmospheric Transmission model (MODTRAN). Section 4.7 will describe the detail of this

radiometry modeling and prediction.

4.1   Fire Characterization Experiment

4.1.1   Measurement Overview

Spectral characterization of biomass fire extending from the visible to long-wave IR (generally 14μm) are needed for both synthetic image generation and algorithm evaluation if we are to move beyond the simple assumption that fire is a blackbody. A number of laboratory experiments were performed that were designed to measure fire physical parameters relevant to remote sensing of fires such as transmissive radiance, featured line emission, and temperature. Coordinated measurements with instruments such as visible and infrared radiometers, a thermocouple logger, and a digital video camera were used to record basic physical processes during test burns at the USFS Fire Science Laboratory in Missoula, MT. An Analytical Spectral Devices (ASD) spectroradiometer was used during that experiment to measure radiance and line emission from visible to near IR. Thermocouples were used to measure flame and fuel bed temperature.   High speed video camera was used to monitor flame evolution. An Infrared Systems Radiometer was used to measure radiance from the near IR to long IR during a second set of test burns at RIT.

4.1.2   Infrared Systems Radiometer

The Infrared Systems Model 12-550 research radiometer is a modular, personal computer-based system for measuring, storing, analyzing and processing radiometric information. The 12-550 consists of a sensing head and an electron-

ics processing unit. The sensing head features a rigid optical bench that allows a wide selection of field-interchangeable fore-optics, spectral scanning modules, and detector/preamplifier packages. It has a two-layer HgCdTe/InSb sandwich detector. Detector InSb covers the spectral region of $1.5 \sim 6.0\mu$m with resolution 0.05μm; detector HgCdTe covers the region of $2.1 \sim 15.0\mu$m with resolution 1.0μm. With the layered detectors the total working region could extend from near IR to longwave IR. Since the system employs two IR detectors, it should be capable of focusing IR energy from different wavelengths onto the same focal plane. With a normal lens the longer wavelengths don't bend as much as the shorter wavelengths. Different wavelengths bend differently and won't focus together – there will always be wavelengths out of focus!

To make a precise measurement, we have to consider how much the target occupies the radiometer's field of view (FOV). If the target fills the FOV direct measurement can be made without further information. If the target is smaller than the radiometer's FOV, background radiance information has to be supplied to complete the measurement. To determine whether the target "full-fills" or "partially-fills" FOV, need to know size of target and FOV, use following equation

$$distance = targetsize/FOV$$

to calculate the maximum distance that the target could fill the FOV and background measurement is not required.

The Infrared System Radiometer is a scanning system. A complete scan from about 1.5 to 15 μm takes about 10 to 20 seconds. There can be considerable variation in the flame during the course of the scan which will cause unavoidable changes in the detected radiance. Careful alignment of the sensor through the

base of the flame will minimize variation from the flickering flame.

4.1.3   Analytical Spectral Devices Fieldspec Radiometer

High spectral resolution observation of fire can lead to better observation of fire emission transmission properties. The ASD has been used to observe smoke and fire radiance in this research to find key features for spectral simulation and detection. The ASD is field spectrometer for quantitative measurement of spectral radiance, irradiance, reflectance or transmission from 350nm $\sim$ 2500nm with 3 nm resolution. The fine structure in the ASD reading can record potassium (K) emission lines which are quite narrow and occur at 766.5nm and 769.9nm. The equipment is shown in Fig. 4.1. The bare fiber optic cable of ASD has a field-of-view angle of 20°. There are optional fore optics attached to the Pistol Grip and reduce FOV to as little as 1°. We used ASD in radiance mode and fore optics of 1° for data collection. Besides fire spectra, reflectance of the burn scars could also be measured by the ASD.

Internal ASD software is used to adjust instrument gain for optimal performance, and dark-offsets are also determined and stored for automatic subtraction from reflectance calculation. Since fires are a very bright target, we used a blackbody with temperature set to 1100K, about maximum fire ground temperature, and optimize the performance of the ASD to avoid detector saturation prior to recording the spectrum of a fire. A neutral density (ND) filter maybe applied to avoid saturation.

Figure 4.1: Analytical Spectral Devices

4.1.4   Thermocouple

Wien's Displacement Law states that there is an inverse relationship between the wavelength of the peak of the emission of a black body and its temperature. This relationship is useful for determining the temperature of hot radiant objects such as flame, whose temperature is far above that of its surroundings. With Wien's law flame temperature could be derived from radiance peak wavelength. Besides the radiance observation, the most straightforward and precise method for determining the temperature of a fire is placing a probe directly in the flame. The thermocouple consists of a wire probe made of two different metals. Because the metals expand at different rates with temperature, the voltage potential across the probe can be precisely calibrated to give temperature reading. In measurement, an array of thermocouples were placed above the fuel bed to monitor fire kinetic

temperature.

4.1.5 Data Collection

A field experiment was conducted at the Rocky Mountain Research Station in Missoula, Montana in 2004. A laboratory chamber was set with fuel that is very similar to woodland fuel composition. The length of the fuel bed was varied from 1 foot to 8 feet to study the change of fire radiance and potassium emission with flame thickness. The fire kinetic temperature along the observation path was monitored by an array of thermocouples on the fuel bed, as shown in Fig. 4.2. Thermocouples were bound and hang right above the fuel, such that they could stay in flame when the fuel was burning. The ASD were placed at one end of the fuel bed to measure the fire radiant emission. The ASD was calibrated by a 1100K blackbody before measurement. A series of neutral density filters were fixed on the ASD optics to avoid sensor saturation. Spectral measurements with the IR systems radiometer were made outdoors at RIT 12 December 2005 on pine wood burning in a small (0.5m) container. The flame thickness was no more than about 50cm.

For all equipment a large dynamic range is necessary for detectors to avoid saturation. Aspects of this field experiment important to our analysis and study include evolution of temperature, descriptive spatial features of the flame, and spectral characterization of the fire radiance.

4.1.6 Flame Evolution Observation

A high-speed video camera can divide one second into hundreds to thousands of visible sections of the normally unseen. To observe the flame evolution, a
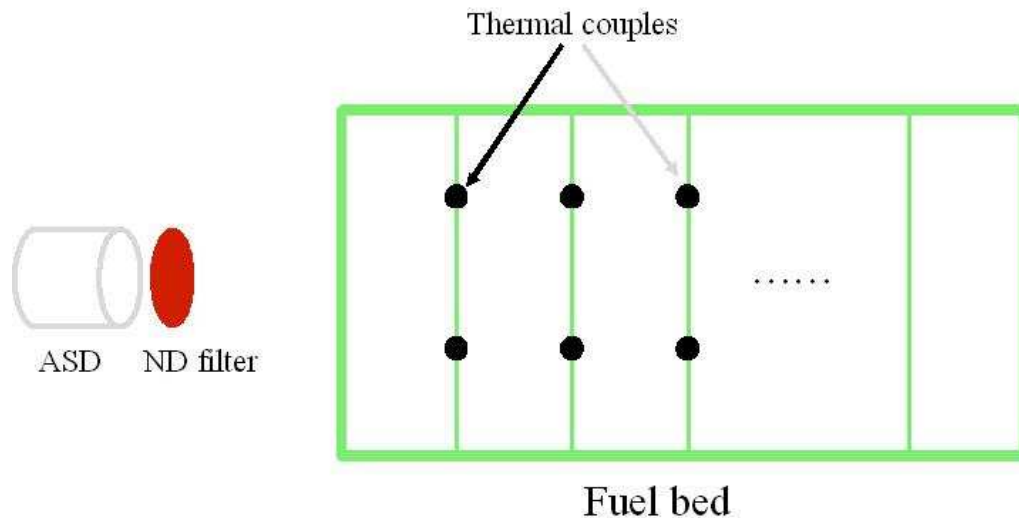
Figure 4.2: Experimental set up for laboratory measurements of fire parameters made at the Fire Science Laboratory.

controlled burn in an open-topped wind tunnel was set and captured with a high-speed video camera. The open-topped wind tunnel was used to remove the effects that a ceiling may have on the flame buoyancy. The wind was induced to test effect of wind velocity on flame length and deflected angle. The high-speed video camera can capture ~120 frames per second in a subsampled mode. Since the integration time for each frame is very short (0.008 second), the fine structure of the fire is visible. Most obvious are the forward bursts of fire which are stretched and seperated from the main flame and are propagated further downwind. The bursts quickly cool down and turn black. This overall behavior is repeated. Analysis of flame structure and evolution from the high speed movie help in design of 3D voxel structure and in experiments measuring fire radiant temperature and spectral signatures. Fig. 4.3 shows a series of frames each 0.017 second apart captured by the high-speed camera.
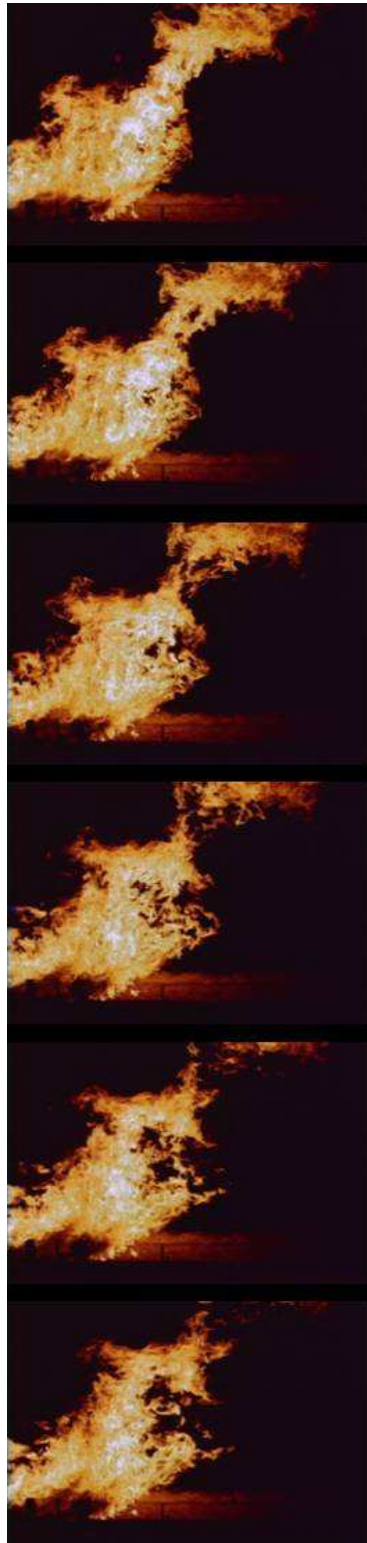
Figure 4.3: Frames of flame each 0.017 second apart, taken with high-speed camera. The forward bursts of fire are stretched and propagated further downwind.

4.2 Digital Imaging and Remote Sensing Image Generation (DIRSIG)

The DIRSIG model is an integrated collection of independent first principles based submodels which work in conjunction to produce radiance field images with high radiometric fidelity. This modular design creates a high degree of flexibility and interchangeability within the model, as well as the capability to diagnose and improve the model by isolating and analyzing each submodel (Brown, 2003). There are five primary submodels of DIRSIG. They are the Scene Geometry Submodel, Ray Tracer Submodel, Thermal Submodel, Radiometry Submodel, and Sensor Submodel. In combination these modeling tools can be used to create synthetic remote sensing scenes.

Image generation in DIRSIG begins by creating the geometric information of the scene. 3-D wire frame models are built in a CAD environment such as Rhinoceros and MAYA. The scenes created using those packages are then facetized. Facets (for solid and liquid objects) and voxels (for gas and plume volumes) are the most basic building blocks in the scene, each one representing a unique material type (See Fig. 4.4). Each facet contains information about its location in the scene to include its vertices, surface normal, slope angle, and azimuthal angle. Each voxel contains information about its location, material type, temperature, and concentration. The material properties include specific heat, thermal conductivity, mass density, specularity, emissivity, optical description, exposed area, and thickness for solid objects; temperature, concentration, and absorption for gas.

The Sensor Submodel converts the entrance aperture radiance to system out-

Figure 4.4: A wire-frame representation of a single DIRSIG object used to construct scenes

put radiance through the system responsivity, which is modeled with Equation 4.1 (Schott *et al.*, 1998). Specifications of the sensor in the scene are sensor response, focal length, spectral bandpass, etc.

$$L_i = \int L_\lambda R_i(\lambda) d\lambda \tag{4.1}$$

The Ray Tracing Submodel projects the three dimensional scene data into a two-dimensional image that conforms to the specifications of the sensor (linescanning, pushbroom, framing, etc.). Rays are cast from the sensor, to an object, either a surface area or a volume, in the scene. Radiance works strictly in the reverse direction. If the ray intersects a facet or voxel along its journey then the facet/voxel is checked to see if it is opaque or transparent. If it is transparent then the ray is attenuate by the transmissivity of the facet/voxel and the ray continues on until it strikes another facet. The specular contribution is determined by casting two more rays, one to the sun and one in the specular direction to determine the radiance hitting the facet from the sun or from another back-

ground object (Brown and Schott, 2000). The radiance from these two sources is attenuated by the reflectivity of the facet and the angular dependent specular falloff values. Once all this has been accomplished, the emissive, specular, and diffuse components are summed, multiplied by the atmospheric transmission, and added to the upwelled radiance.

The Thermal Submodel utilizes solar absorption and thermal emissivity coefficients in the radiational loading computations. The model allows the user to specify an internal or self-generated power term that can be used to model a simple internal heat source within the surface. This can be a useful tool for modeling internal heat sources in buildings or even the biological activity in living vegetation.

The Radiometry Submodel is the mathematical engine behind the Ray Tracing Submodel. Air Force's MODTRAN model is used to determine physical processes in atmospheric propagation from 100-50000 cm^{-1} with a spectral resolution of 1 cm^{-1}. MODTRAN can determine exoatmospheric irradiance, emitted and scattered radiances, and path transmission at a maximum spectral resolution of 2 wave numbers. This submodel features path length dependent extinction and emission for transmissive bodies (flames, plumes, clouds, etc.). The radiometry model simply processes the rays generated by the ray tracer to compute a spectral radiance reaching the sensor for a given pixel (Brown, 2003).

The difficulty in simulating fire is that it does not have regular shape and there are no smooth spatial distribution of points to track. In other words, there are voids, dense clumps, and very hot spots in the flame, all of which result from turbulence in the fire and are obviously observed in real wildland burning. To visualize objects of complicated spatial distribution, as well as correct radiometry

simulation, stepwise integration is utilized in this research.

The stepwise integration algorithm decomposes a complicated curve into a group of small subsets/parts. The algorithm is implemented in this research to calculate total radiance through the medium in which temperatures and densities are varied. Fig. 4.5 explains how well the stepwise integration works on a curve integral. The area under the exponential curve needs to be estimated. The methods relies on rectangles that occupy the area under the curve. The approximation is improved as the number of rectangles increases and each integrating step shortens. The area under the exponential curve is adequately estimated with 50 rectangles relative to that with less steps. Just like computing derivatives, a statement can be made about an arbitrary large number of rectangles in order to approach the best approximation. The tradeoff is the balance between the exactness and computing, as well as rendering time.

The Generic Radiometry Solver handles the surface leaving radiance (reflected + emitted) calculation. It samples the hemisphere above the target and integrates the reflected radiance into a given direction. The user has control over the amount of hemispherical sampling and the number of bounces used to solve for the flux reflected by the surface on a per-material basis.

Since its inception, DIRSIG's development has been focused on creating precise radiometrically accurate images through the use of first principles equations in conjunction with empirically measured, material specific emissivity databases. A great deal of research has been conducted on its accuracy. All of this makes DIRSIG the logical choice for rigorous modeling the radiometry for wildfire.
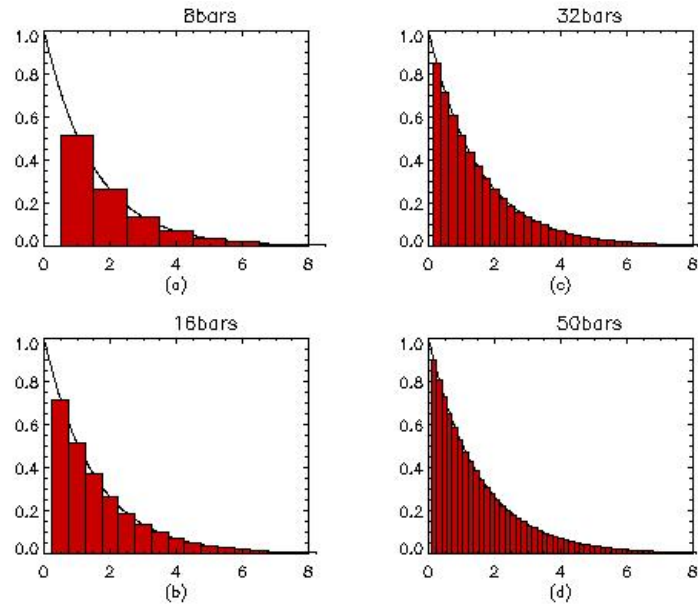
Figure 4.5: Compare estimation of area under exponential curve with stepwise integration with different number of steps. (a) with 8 steps. (b)with 16 steps. (c) with 32 steps. (d) with 50 steps.

4.3 Voxelized Geometry

For remote sensing purposes, the radiance image should contain information from all the voxels, and the result is an accumulation of radiance that is a function of the material density, extinction, temperature, distance from the sensor, etc. The development of voxel rendering prompted the availability of viewing the flame structure as a three-dimensional field rather than as individual pixels. This gives the advantage that information could be visualized from any view direction. With stepwise integration, when a ray cast from the sensor encounters a region containing fire that was pre-computed by the external fire model, the simulation determines how many integration steps to process through the fire, or, how many

voxels containing fire on the way of cast ray, and the path length within each of the voxels. The physical field is considered as a voxel system: a set of physical properties defined for N regular spaced voxels. When the integration point does not fall on a grid point, a bi-linear interpolation is performed to compute the fire property at the integration point (Digital Imaging and Remote Sensing Laboratory, 2006). Physical properties of each voxel are a function of its temperature. Then, physical properties of each participating voxel are summed up to give a final projection to imaging plane. A participating voxel modifies the propagation of light through emission and absorption. Scattering is not considered so far.
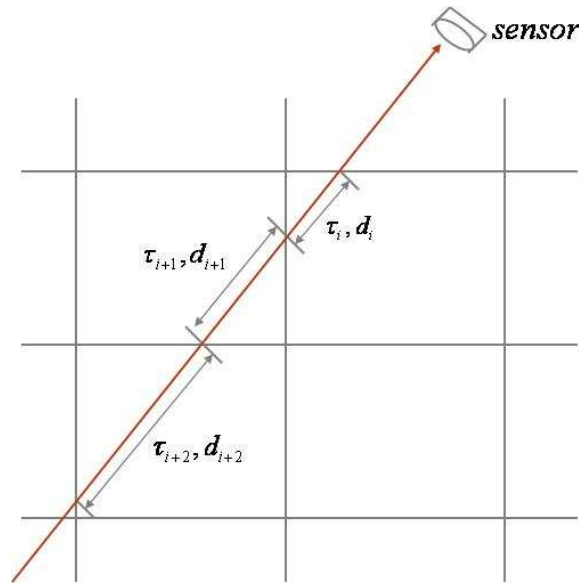
Figure 4.6: Ray cast on grids.

Fig. 4.6 shows how a ray passes grids/voxels, where τ_i is the transmission of each voxel along the ray's path. The additive projection is a summation of attenuated and transmitted radiance from all the voxels. The transmission properties of participating voxels are characterized by path length over the ray and

fire absorption. If we let there be n voxels between the ground and the sensor along the way of sight, then the contribution to the received radiance due to the self-emitted radiance from the ith voxel can be expressed as Eq. 4.2:

$$\Delta L_i = L_i \left(\tau_i - \tau_{i+1} \right) \tag{4.2}$$

where the indexing scheme for the fire voxels is defined to begin at the sensor and end with the voxel just above the ground. L_i is the radiance due to the temperature of the ith voxel; τ_i is the transmission along the sensor-target path from the sensor to the top of the ith voxel, and is the product of transmission of all the voxels between ith voxel and the sensor.

$$\tau_i = \prod_{j=1}^{i-1} \Delta \tau_j \tag{4.3}$$

$$\Delta \tau_j \left(\lambda \right) = e^{-\delta_j(\lambda)} = e^{-\beta d_j} \tag{4.4}$$

where δ is the optical depth along the vertical path to the sensor altitude; β is the medium extinction; d_j is the path length within the jth voxel on the sensor-target path; $\Delta \tau_i$ is the transmission of ith homogeneous voxel. It is obvious that the transmission along the path decreases due to the increased path length.

Substituting Eq. 4.4 into Eq. 4.3, we have

$$\tau_i = \prod_{j=1}^{i-1} e^{-\delta_j(\lambda)} \tag{4.5}$$

$$= \prod_{j=1}^{i-1} e^{-\beta d_j} \tag{4.6}$$

$$= e^{-\beta d_1} e^{-\beta d_2} ... e^{-\beta d_{i-1}} \tag{4.7}$$

$$= e^{-\beta \sum_{j=1}^{i-1} d_j} \tag{4.8}$$

Summing the radiance from each single voxel and substituting Eq. 4.8 in Eq. 4.2, the total contribution to radiance from the voxels can be expressed as the right side of Eq. 4.11.

$$L = \sum_{i=1}^{n} \Delta L_i \tag{4.9}$$

$$= \sum_{i=1}^{n} L_i \left(\tau_i - \tau_{i+1} \right) \tag{4.10}$$

$$= \sum_{i=1}^{n} L_i \left(e^{-\beta \sum_{j=1}^{i-1} d_j} - e^{-\beta \sum_{j=1}^{i} d_j} \right) \tag{4.11}$$

where the sum is over all the voxels in the direction of the casted ray. The flowchart in Fig 4.7 describes the steps in calculating sensor reaching radiance from each of the voxels on the way of the casted ray.
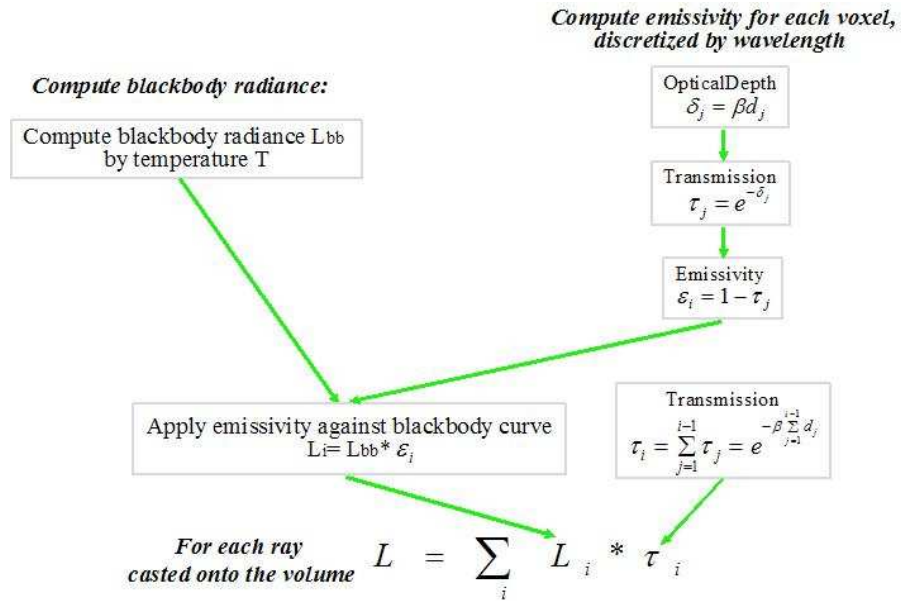
Figure 4.7: Volume rendering with regular grids.

4.4 Simulation of Fire as Secondary Source

Another phenomenon that must be included for visualizing the fire volume is to have the fire as a secondary source which illuminates the surrounding area. The support for secondary sources in DIRSIG includes modeling point sources and area sources and allows the user to observe illumination effects from these source objects (Ientilucci *et al.*, 2001). Secondary point sources are isotropic point sources that have isotropic angle distribution and radiate equally to all directions.

To simulate a point source in DIRSIG, radiant intensity of the source is required. With the equipment available, fire radiance could be measured. What needs to be figured out is how to convert source radiance to radiant intensity. Consider a spherical surface at distance r from a point source of radiant intensity $I_0[ws_r^{-1}]$ as shown in Fig. 4.8. The point source is radiating energy equally to
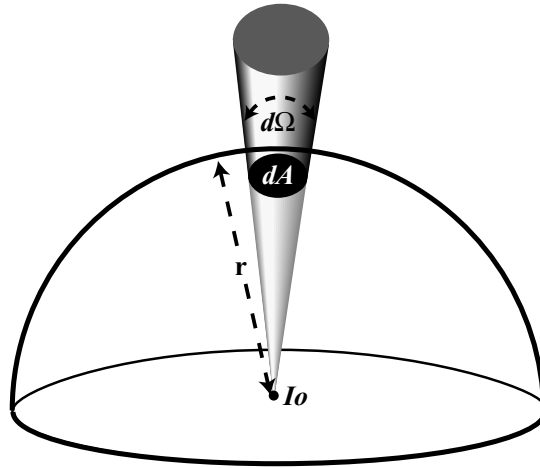
Figure 4.8: A source of radiant intensity I_0 produces an irradiance at a distance r of I_0/r^2. (Image courtesy of Dr. John Schott.)

all direction at radiant flux Φ[watts]. The radiance $L[wm^{-2}sr^{-1}]$ reaching the sphere is defined as:

$$L = \frac{d^2\Phi}{dA\cos\theta d\Omega} = \frac{dI}{dA\cos\theta} \tag{4.12}$$

where dA$[m^2]$ is an area element on the surface of interest; θ is the angle from the normal to the projected surface to the incident ray; $d\Omega$[steradian] is the element of solid angle; I$[wsr^{-1}]$ is the radiant intensity from the point source. Rewrite radiant intensity I as function of radiance L

$$dI = LdA\cos\theta \tag{4.13}$$

Since the area of point source is zero, radiant intensity can't be obtained by Eq. 4.13 and the term dA has to be substituted by another term. Using the

definition of solid angle

$$d\Omega = \frac{dA}{r^2} \tag{4.14}$$

where r is the distance from source to the area element, one can rearrange and substitute dA in Eq. 4.13 and obtain

$$dI = Lr^2 d\Omega \tag{4.15}$$

In our fire measurement, we used the ASD with the 1 degree optic to measure fire radiance. The ASD was placed about 2 meters distance from fuel bed. So, distance, r, from source to measuring surface is known; with distance r and optic FOV, solid angle Ω can be calculated. So far, all terms required to calculate the radiant intensity are available. Recall the definition of Inverse-Square Law that irradiance E from a point source of known radiant intensity I, varies inversely with the square of the distance r. It also explains why the point source appears to have finite extent in the image.

$$E = \frac{I}{r^2} \tag{4.16}$$

Since point source has no shape, the radiance/energy from it has to hit some geometry object before being seen. In Fig. 4.9 each of the radiating point in fire casts irradiance to certain small area on the ground before hitting the sensor. The irradiance from the point source reaching the area follows the Inverse-Square Law. A threshold $1\%I_0$ of the point source intensity is set to ignore the small irradiance onto the surfaces from far away. The irradiance on the area is the linear summation of all secondary sources from flame. (DIRSIG knows the solid angle of point source when it is casting rays to the small area. DIRSIG will calculate

the solid angle of focal point to detector/CCD element. If the detector is not over sampled, there will be single ray from center of the sample area to the center of the detector; with oversampling there will be a ray from center of the area to the center of each of the sampled area within single detector.)
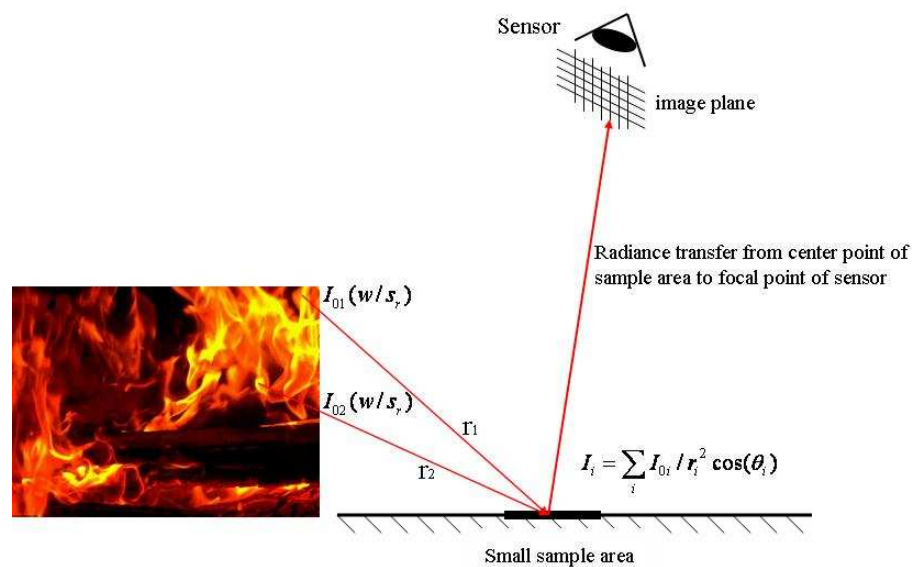
Figure 4.9: A ray tracer is utilized to determine how much radiance each emitting fire point contributes to the given pixel.

4.5   Fire Area Time-Temperature

The third requirement for correctly synthesizing remote sensing images of fire is that we should know the ground temperature before and after the passage of fire. Because the 2D ground surface is a solid surface with generally high emissivity, it has the potential to contribute considerable radiance to the scene. (Kremens and Faulring, 2003) made the measurement of surface temperature and

determined the length of time the burn scar remains visible to mid and long-wave infrared sensors for different ecosystem types, see Section 2.8.3.

To estimate how the burn scar temperature decreases with time, let's take a look at the issues that have to be concerned of ground cooling rate. The biomass root and the visible soil through the grass/soil areas contain a lot water which absorbs heat/radiation during the burning and releases the energy after fire. So there are two factors accounting for the burn scar temperature decay, one is natural ground cooling, the other is energy releasing from water which keeps surface temperature remains above ambient temperature a little longer after passage of the flaming front. Sum of two exponential curves with different time constants are used to model the ground temperature drop after fire front

$$T_t = T_1 e^{\frac{-t}{\tau_1}} + T_2 e^{\frac{-t}{\tau_2}} + T_a \qquad (4.17)$$

where T_t is time temperature of burn scar; T_1 and τ_1 are the peak temperature and time constant of curve one for natural ground cooling; T_2 and τ_2 are the peak temperature and time constant of curve two for energy releasing from water; T_a is 34^oC, ambient ground temperature during a bright sunny day; t is the time since ignition. The sum of T_1, T_2 and T_a is 800^oC, which is the peak temperature measured once the biomass is ignited. With T_1, τ_1, T_2 and τ_2 we can predict time-temperature of burn scar, generate a temperature map and synthesize the remotely-sensed burned-over area, and derive the path history of the fire.

A good match is obtained by fitting data points in (Kremens and Faulring, 2003) to Eq. 4.17. Fig. 4.10 shows the measured time-temperature profile (black) and curve-fitted results (red) with POWELL and AMOEBA algorithms. The algorithms are gradient-expansion algorithms which minimize a function of two

or more independent variables by computing a non-linear least square fit. Both
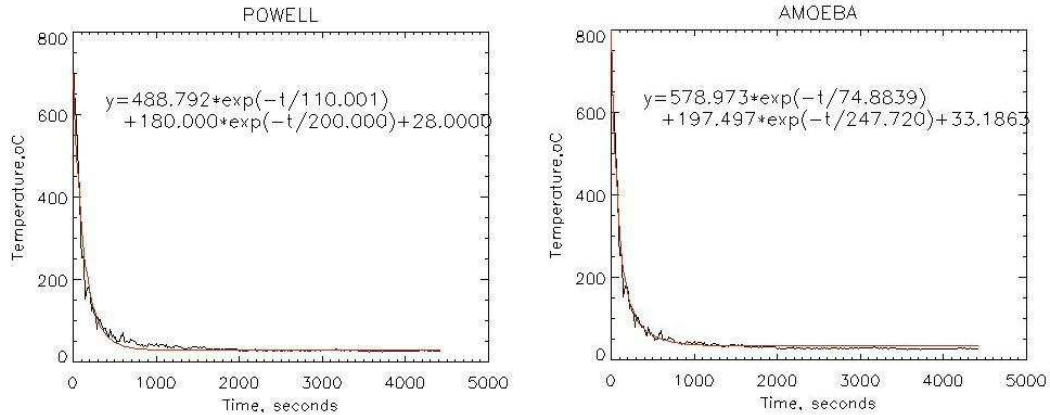
Figure 4.10: Time-temperature profiles. Dark curves are temperature measured by thermocouples in contact with soil surface. Red curves are decay time curve fit using two time constant exponential decay, left one with POWELL and right one with AMOEBA algorithm respectively.

of the fitted curves match the measured data points well. The POWELL algorithm is efficient and stable, but more sensitive to the start point of estimation. The AMOEBA algorithm gives better curve fit as long as it starts with proper start points of estimation. It fits the varying part well and reaches global minimum easily. With coefficients estimated with the AMOEBA algorithm the time-temperature of burn scar can be calculated as

$$T_t = 578.97e^{-t/74.88} + 197.50e^{-t/247.72} + 33.19 \qquad (4.18)$$

Preheating is a complex process relating to the fuel characteristics, wind, humidity, and etc. The thermal transfer mechanism in preheating might include both radiation and convection and could be very complex. In this work preheating process is simplified to a jump from ambient temperature to 800^oC. Fig. 4.11 is

an example of the modeled ground time-temperature.
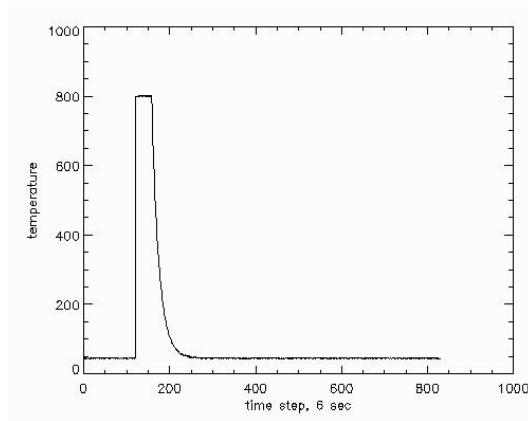
Figure 4.11: Modeled Time-temperature profile

4.6   3D Flame Geometry Estimation

Although fire simulation has been the subject of many investigations, with notable exceptions there have been relatively few studies of fast real-time flame simulation and prediction. An important part of this research is making fast prediction of 3D flame structure from heat sources on the ground, and adding the 3D flame structure to 2D ground fire propagation. We assume that the fire is a wind-blown flame with known heat flux along the ground surface taken from the propagation model. Three methods for predicting flame height were examined.

4.6.1 Estimate of flame height from surface fire sensible heat flux

This method assumes that the fire is a wind-blown flame with known heat flux along the ground surface. 'The amount of heat actually released during combustion is influenced by the surface area to volume ratio of particles in the fuel bed' (Wooster *et al.*, 2004). In this regard we could relate flame size to heat release, and further predict flame height when subjected to a given heat flux along the ground surface. High heat flux is translated into big flames (tall) and lower heat flux is translated into small flames (short). Due to the swirls within the burning region and the interactions between fire and the environment, the flame could be very turbulent. To make the real-time prediction and visualization of 3D flame for large and fast propagating wildfire, we focused on predicting flame height relative to the heat flux, instead of complex turbulence and complicated spatial configuration, which is often the goal of the graphics community.

Some experimental studies (Ris, 2002; Orloff and de Ris, 1982) showed that the flame volume is directly proportional to the chemical heat release rate of the fire,

$$V_f = \dot{Q}_{ch}/\dot{q}_{ch}''' \tag{4.19}$$

where V_f is the flame volume; $\dot{Q}_{ch}$ is the total chemical heat release rate of the fire; $\dot{q}_{ch}'''$ is the chemical heat release rate per unit flame volume, a constant $2000kW/m^3$. In the case of radiative heat transfer which tends to leave equally in all directions, it is appropriate to set proportionality between chemical heat release rate $\dot{Q}_{ch}$ and radiative heat transfer rate, take into account the area on

the ground through which the heat is being transferred there is the heat flux Q_h.

$$\dot{Q}_{ch} \propto Q_h \tag{4.20}$$

We assume that the fire volume V_f is the multiplication of fire ground area and flame height l_f. Fire ground dimensions are estimated by sizes of remotely sensed ground heat flux. If fire front has length w_1 along the direction of fire propagation and width w_2 perpendicular to the direction of fire propagation,

$$V_f = l_f w_1 w_2 \tag{4.21}$$

Substituting Eqs. 4.20 and 4.21 into Eq. 4.19 and rearranging, the flame height l_f can be estimated by

$$l_f = \frac{Q_h}{\dot{q}_{ch}''' w_1 w_2} \alpha \tag{4.22}$$

where α is a scale coefficient. Since wildland fires behave quite differently, an adjustable scale coefficient α is added according to fuel type to make the predicted flame size reasonable. In the simulation performed here for a grass land fire, a flame height of 2m was assumed.

Heat flux is proportional to temperature difference, thus pixels with large heat flux are taken as fire front where there is large temperature gap with surrounding area. Fire length is decided by scale of fire front. Because of spatial and temporal self-similarity of flame, the estimated flame height of each time step is constrained within one standard deviation from the heights of all the previous time steps, thus the flame height of each time step won't be too deviated from the previous or following time step when there is no dramatic change of atmospheric conditions such as wind, temperature, and humidity.

We analyzed images of a wood fire from the side with constant wind obtained with a high speed digital video camera to observe the flame geometry. Images with short integrating time show that there were forward bursts of flame which separated from the main body of flame. The forward bursts of flame composed of burning embers died out as they propagate away from the fire and cooled off. New balls of flame broke up from the fire and repeat the previous steps. In this research the predicted flame heights that are out of one standard deviation from the statistics are taken as these discontinuous flame. This method was used in generating the voxel distribution in this work.

4.6.2   Estimate of flame height from total heat release rate

(Heskestad, 1995) proposed the following expression for mean flame height:

$$L = -1.02D + A\dot{Q}^{2/5} \tag{4.23}$$

where D is the diameter of the fire source (or effective diameter for non-circular fire sources such that $\pi D^2/4$ = area of fire source); $\dot{Q}$ is the total heat release rate; A is the non-dimensional parameter defined by

$$A = 15.6 \left[\frac{C_p T_\infty}{g \rho_\infty (H_c/r)^3} \right]^{1/5} \tag{4.24}$$

where C_p is the specific heat of air; T_∞ and ρ_∞ are the ambient air temperature and density, respectively; g is the acceleration of gravity; H_c is the heat of combustion; r is the actual mass stoichiometric ratio of fuel-to-air ratio. H_c/r, the heat liberated per unit mass of air entering the combustion reactions, remains within the range of 2900 to 3200 KJ/Kg for a large number of gaseous and liquid fuels.

The associated range of A for H_c/r under normal atmospheric conditions (293K, 760 mm Hg) is 0.240 to 0.226 ($mKW^{-2/5}$), with a typical value of A=0.235. Solid fuels have a different story. H_c is 34300kJ/kg for wood char, 20934kJ/kg for paper birch, 15000kJ/kg for wood. r varies from 1.2 to 1.6 which is much lower than that of the gaseous and liquid fuels. If r is chosen to be 1.2, then A of wood char, paper birch, and wood are 0.062, 0.083, and 0.114 respectively, all of which are lower than A of gaseous and liquid fuels.

In this research wildfire field properties are represented by a 2-dimensional array of 20m x 20m grids with 140 cells on each axis. The effective diameter for 20 m x 20 m grid area is calculated by $\pi D^2/4 = 20 \text{ x } 20m^2$ and $D = 22.57m$.

The output from fire propagation model includes surface fire sensible heat flux. To get the heating in each grid volume, we need to calculate the vertical flux divergence:

$$\Delta Q_z = \frac{H_{fz} - H_{f0}}{z} \tag{4.25}$$

where H_{f0} is the surface fire sensible heat flux; H_{fz} is the heat flux of above grid at height z. H_{fz} decreases with height as an exponential function with the e-folding height 50 m.

$$H_{fz} = H_{f0}e^{-z/50} \tag{4.26}$$

Combining Eqs. 4.25 and Eq. 4.26 by substitution of H_{fz}, and integrating ΔQ_z with respect to z from ground level to infinite high yields the total heating Q from any 20 m x 20 m grid space with ground heat flux H_{f0}

$$Q = \sum_z^\infty \Delta Q_z = H_{f0} \sum_z^\infty \frac{e^{-z/50} - 1}{z} \tag{4.27}$$

Fig. 4.12 shows how the surface sensible heat flux and the total heating from
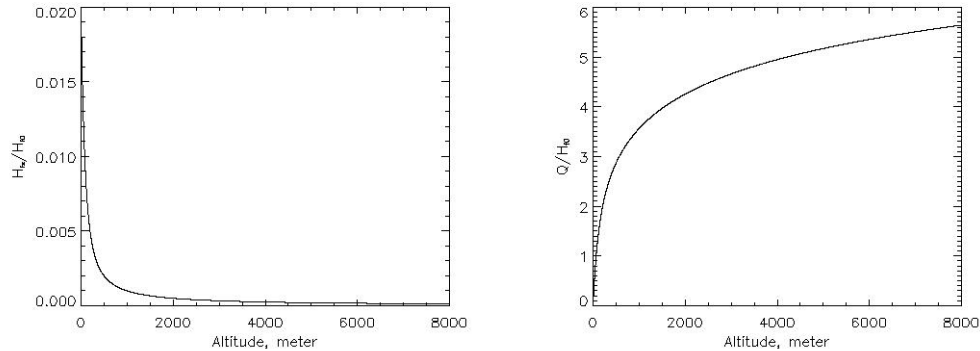
Figure 4.12: Left: heat flux H_{fz} decreases with height. Right: total heating Q from 20m x 20m grid space with surface sensible heat flux H_{f0}.

ground unit area decrease with height.

So far effective diameter D, coefficient A, and total heat release rate $\dot{Q}$ are known. These are substituted into Eq. 4.23 to calculate wood fire height. Fig. 4.13 shows the flame heights calculated with $A = 0.235$, the typical value for gaseous and liquid fuels. Fig. 4.14 shows the flame heights of wood char fire estimated with the heating.

Estimated wood char flame heights are lower than that of the gaseous or liquid fuel. It is clear in Eq. 4.23 that with fixed D and $\dot{Q}$, the larger the coefficient A, the higher the flame height L, thus wood char fire will always be lower than gaseous or liquid fire. Since it is less likely that visible flames can fill whole 20 m x 20 m area, the effective fire area has to be scaled down. If the effective fire area is scaled down by 1/40 and effective diameter is 3.57m, maximum flame height of most time steps are around 2m. If the effective fire area is scaled down by 1/20 and the effective diameter is 5.05m, then the estimated flame height may be negative.

(Newman and Wieczorek, 2004) reported that Eq. 4.23 applies well to the
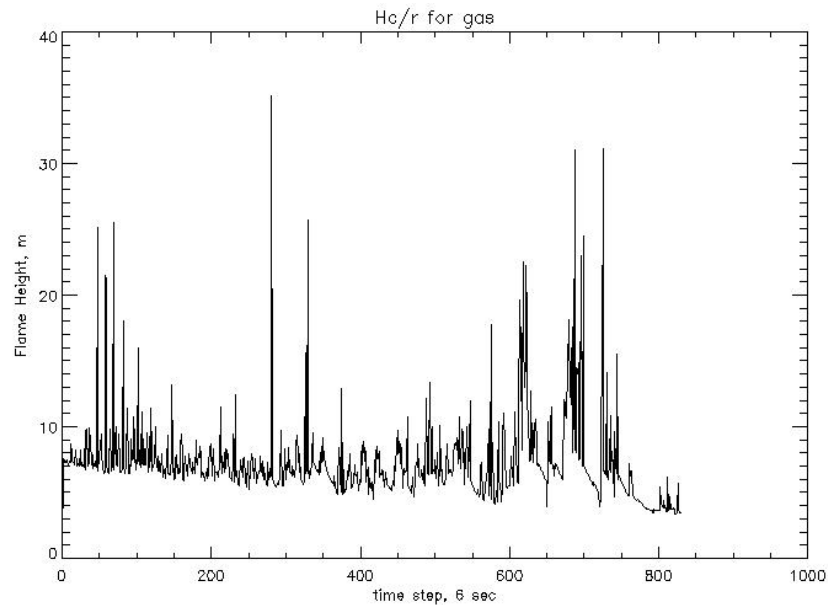
Figure 4.13: Flame heights of gas fuel with effective fire area scaled down by 1/40 from 20m x 20m.

chemical flame height estimation of gaseous and liquid pool fire less than 1m in diameter. According to the result in this research, the methodology proposed by (Heskestad, 1995) is not proper for solid fuels (wood etc.) because they liberate more heat per unit mass of air entering the combustion reactions. On the other hand, large scale wildfires are more turbulent and release more variable heat (including 70% of convective and 30% radiative heat release) to the surroundings. The methodology in (Heskestad, 1995) is not able to constraint the predicted flame heights within certain range given high variable total heat release rate of any burning process. That is why the estimated wood char flame heights at different time steps vary from 1m to 15m. Due to this variability and the difficulty in scaling the flame height this method was not used.
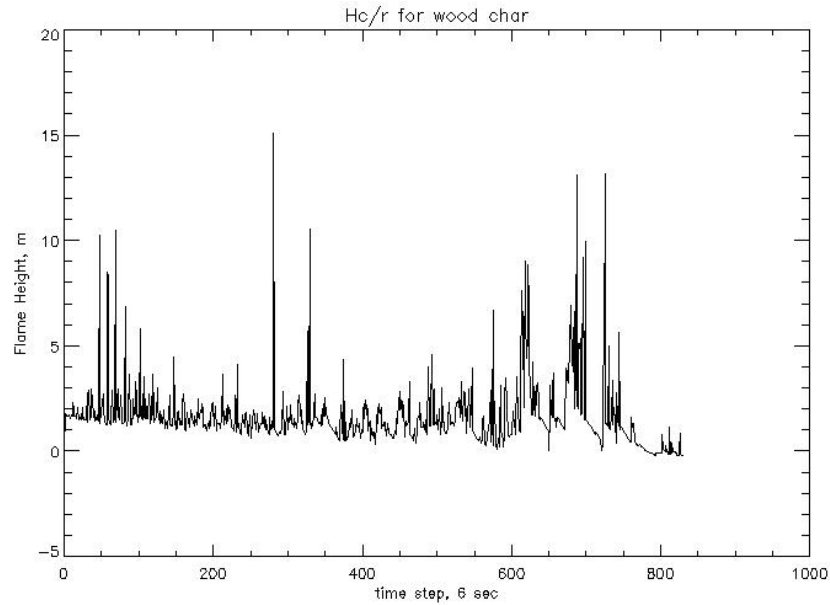
Figure 4.14: Flame heights of wood fuel with effective fire area scaled down by 1/40 from 20m x 20m.

4.6.3 Estimate of flame length from fuel loading

Flame length is defined to be the distance from the middle of the flame base to the flame tip. (Byram, 1959) proposed an empirical model of calculating flame length based on wood crib burns in the 1950's.

$$L_f = 0.0775 * I_B^{0.46} \qquad (4.28)$$

where I_B is the fire line intensity

$$I_B = H_c w R \qquad (4.29)$$

where H_c is heat of combustion, $20934kJ/kg$ for paper birch (Weise and Big-ing, 1996). 'If the heat of combustion is reduced for radiation loss (2791kJ/kg) and heat associated with water loss (1628kJ/kg), a low heat of combustion of 16515kJ/kg results' (Brown and Davis, 1973). w is fuel loading, kg/m^2; R is the rate of spread. Fuel loading is defined in the fire/fuel grid cells, which are subdivided from the atmospheric grid cells, on which the heat fluxes are defined.

(Weise and Biging, 1996) modified this relation from the results of wind tunnel tests on burning excelsior and wood sticks,

$$L_f = 0.016 * I_B^{0.7} \tag{4.30}$$

though this may be valid over only a low range of intensities.

Relation proposed by (Dupuy *et al.*, 2003) also produced flame lengths that were too high in simulations. There are more complex relations available in (Drysdale, 1999), but the relations in (Byram, 1959; Weise and Biging, 1996) are the most easily implemented. Although this technique is simple, this method ap-peared to give excessive flame lengths for the parameters provided. More testing of this method for our application is necessary.

4.6.4 Adding wind-caused deflection to predicted flame geometry

Besides terrain and fuel type and amount, wind plays an important role in energy transfer direction and rate. Wind speed is one of the dominant factors influencing ignition and burn down of certain fuels. In the open area, flame will be deflected by any air movement. The extent of flame will depend on the wind

velocity.

The video recorded with a high speed camera shows that the flame and forward bursts of fire tilted and stretched and propagated further downwind. According to study in (Drysdale, 1999), the effect of wind on fires is:

$$sin\theta = 1 \ for \ V^{'} < 1 \qquad (4.31)$$

and

$$sin\theta = (V^{'})^{-1/2} \ for \ V^{'} > 1 \qquad (4.32)$$

where θ is the tilt angle from the vertical to the front of the flame, as shown in Fig. 4.15.

$$V^{'} = V(\frac{2c_pT_\infty\rho_\infty}{\pi\rho_f\Delta H_c})^{1/3} \qquad (4.33)$$

in which c_p is air thermal capacity at constant pressure, 1040 $(J/Kg - K)$; T_∞ is ambient air temperature, 300 (K); ρ_∞ is ambient air density, 1.18 (Kg/m^3); ρ_f is fuel vapor density, 0.36 (Kg/m^3), an estimated value, a little bit higher than air density 0.32 (Kg/m^3) at temperature of 1100k; ΔH_c is heat of combustion, 16515kJ/kg. V is a dimensionless wind speed given by v/u where v is the actual wind speed, and u is a characteristic plume velocity given by

$$u_{max} = 1.9\dot{Q}_c^{1/5} \ m/s \qquad (4.34)$$

where $\dot{Q}_c$ is the rate of heat release.

The deflection angle of each flame pixel is calculated with this method. The flame pixels have different deflection angles according to the magnitude of heat
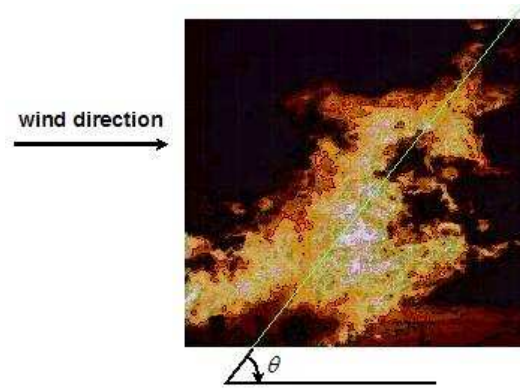
Figure 4.15: Deflection of a flame by wind.

flux from which flame points are estimated. After flame is deflected, small random deviates from a uniform distribution are added to XY coordinates of flame points in well gridded space to make the fire appear more turbulent.

4.6.5   The Complete Algorithm

Given the heat flux of wildfire area and the local wind, the full algorithm of predicting fire scale from heat flux becomes:

(i) Identify fire front by properly thresholding the heat flux, decide fire width by calculating fire front scale.

(ii) Convert heat flux to flame height for the fire front pixels by Eq. 4.28, and constrain the flame height of each time step within one standard deviation of the heights of all the previous time steps. The predicted flame parts which are higher than one standard deviation from the statistics are taken as burning embers breaking up from fire. The flame is represented as a set of voxels arranged on a regular grid.

(iii) Calculate the deflection angle of each fire pixel based on the wind speed.

Small uniformly distributed terms are added to fire pixel coordinates to make fire appear more turbulent.

Fig. 4.16 shows the algorithm processes as a series of images, and Fig. 4.17 shows how the flame evolves with time. In this illustration the flame heights were estimated with method described in section 4.6.1.
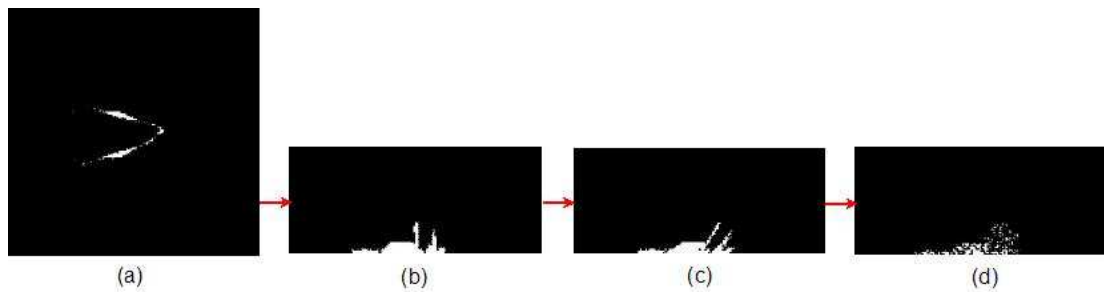
Figure 4.16: Procedures predicting 3D flame voxel geometry, flame heights were estimated with method described in section 4.6.1. (a) top view of 2D heat flux field 61 min 54 sec after ignition. (b) side projection of estimated flame height. (c) side projection of tilted flame. (d) flame with small uniformly distributed shifts.
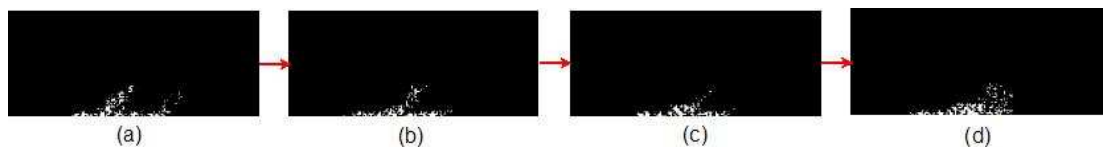
Figure 4.17: Side view of estimated flame evolution. (a) 61:18 (61 min 18 sec after ignition). (b) 61:30. (c) 61:42. (d) 61:54.

This method utilizes the heat flux and wind field to provide simple prediction of flame height and tilt angle which are the primary variables affecting the rate and direction of energy transfer. By iteratively solving Eq. 4.22 from method

I and Eq. 4.31 ∼ Eq. 4.34 while updating the constraint of flame scale, unique solutions to flame height and deflection angle will be obtained for each ground pixel with high heat flux at each time step, and flame geometry will be uniquely defined.

4.7 Atmospheric Prediction for Fire Radiance Observation within DIRSIG

The ground imagery collected by airborne or spaceborne remote sensing missions are contaminated by the effects of atmospheric gases and particles through absorption and scattering of the radiation in the atmosphere, as well as the radiation from the adjacent ground surface. To produce radiometrically correct remotely sensed imagery, or say, to simulate what the sensors really 'see', we should consider not only surface leaving radiance from the target, but also the effects of the atmosphere including water vapor absorption and aerosol features in a well-characterized remote sensing environment. This process is called *atmospheric prediction*. Atmospheric effects within DIRSIG are performed using MODTRAN. By combining the known value of the target and the atmospheric effects, individual pixels in the synthetic spectral scenes should contain radiance originating from both the ground and the atmosphere.

4.7.1 Energy Interactions in the Atmosphere

Aerosol particles can absorb and/or scatter electromagnetic radiation at different wavelengths. They can also emit thermal radiation.

Absorption is a process that removes energy from the electromagnetic radia-

tion field, and converts it to another form. Different molecules absorb radiation of different wavelengths. An absorption spectrum will show a number of absorption bands corresponding to structural groups within the molecule. The absorption of infrared radiation generally corresponds to vibrational transitions in a molecule and visible absorption corresponds to changes in the electronic energy of a molecule.

Scattering is a process which conserves the total amount of energy, but the direction in which the radiation propagates may be altered.

Rayleigh scattering dominates when the particle size is smaller than one tenth of the wavelength of interest. Rayleigh scattering is proportional to $1/\lambda^4$. The strong wavelength dependence of Rayleigh scattering enhances the scattering of short wavelengths, giving us the familiar blue of a cloud free sky.

Mie theory is used when particle is about the same size as the wavelength and Mie scattering dominates when particle size is larger than wavelength. It is not very wavelength dependent and has more of an influence at longer wavelengths than Rayleigh scattering.

Finally, the water droplets that make up a cloud are much larger than the molecules of the air and the scattering from them is almost independent of wavelength in the visible range, producing the typical white or grey reflection from clouds.

Through the law of conservation of energy, the incident energy equals the sum of the reflected, the absorbed, and transmitted energy:

E=$E_{Reflection} + E_{Transmission} + E_{Absorption}$

Dividing through by E gives:

100%=$E_{Reflection}/E + E_{Transmission}/E + E_{Absorption}/E$

Some of the quotients above are known as follows:

$E_{Reflection}/E$=Reflection r,

$E_{Transmission}/E$=Transmission τ,

$E_{Absorption}/E$=Absorption α.

All these quantities are wavelength dependent.

To simulate effects due to fire transparency, *transmission* τ is needed to calculate how much a ray is attenuated when it passes through the volume. *Extinction* (or attenuation) is the sum of scattering and absorption, so it represents the total effect of the medium on incident radiation. The following equation can be used to convert the transmission τ to extinction/attenuation β:

$$\beta = \frac{-ln(\tau)}{d} \qquad (4.35)$$

Rewrite Eq. 4.35 and represent τ with β,

$$\tau = e^{-\beta d} = e^{-ecd} \qquad (4.36)$$

where e is absorption cross-section with units of cm^2; d is the path length of the sample with units of centimeters; c is the concentration of the absorbing species, expressed in cm^{-3}.

4.7.2 Atmospheric Prediction with MODTRAN

The atmosphere affects the brightness (radiance) at a sensor in two ways:

(1) it reduces the illuminating energy (and thus the reflected energy);

(2) it acts as a reflector itself, adding a scattered path radiance to the signal detected by the sensor.
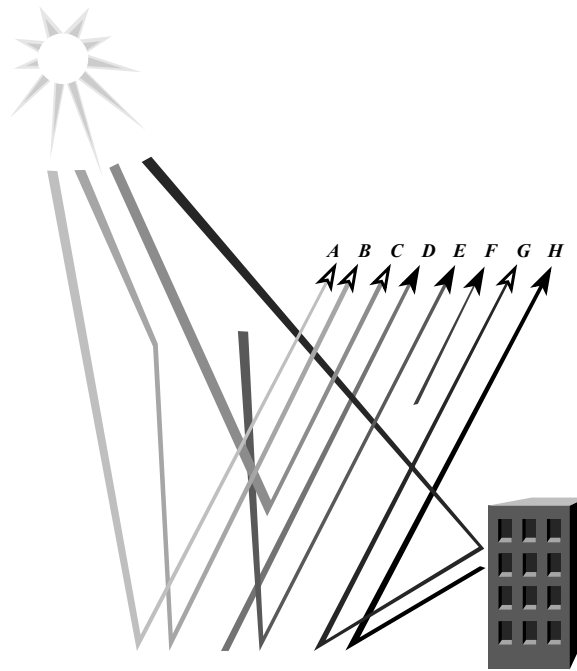
Figure 4.18: Energy paths associated with the photon flux onto the sensor. Image Courtesy of Dr. John Schott.

MODTRAN is applied in this research to predict various radiometric parameters including atmospheric transmission, path radiance, solar irradiance, sky irradiance, and aerosol absorption. Besides the radiation from target, effects of atmospheric and smoke/haze absorption should also be taken into account. Major absorbers of solar radiation include water vapor, carbon dioxide, and ozone. The estimates are then used to predict radiance reaching the sensor and compared to that of real image to tell how well our synthetic method works. For the inverse problem, if the sensor is assumed to provide accurate radiance values, information about absolute or relative reflectance or temperature of scene elements could be extracted providing the atmospheric contribution to the radiance removed.

According to Equation 4.37 from (Schott, 1997), the spectral radiance reaching the sensor is

$$L_\lambda = \{E_s'(\lambda)\cos\sigma'\,\tau_1(\lambda)\frac{r(\lambda)}{\pi} + \varepsilon(\lambda)L_T(\lambda) + F[E_{ds}(\lambda) + E_{d\varepsilon}(\lambda)]\frac{r_d(\lambda)}{\pi}$$
$$+(1-F)[L_{bs}(\lambda) + L_{b\varepsilon}(\lambda)]r_d(\lambda)\}\tau_2(\lambda) + L_{us}(\lambda) + L_{u\varepsilon}(\lambda) \quad (4.37)$$

The relationship between each of these terms and the energy path is illustrated in Figure 4.18. The energy paths associated with the photon flux onto the sensor are

type A	$E_s'(\lambda)\cos\sigma'\,\tau_1(\lambda)\frac{r(\lambda)}{\pi}\tau_2(\lambda)$
type B	$FE_{ds}(\lambda)\frac{r_d(\lambda)}{\pi}\tau_2(\lambda)$
type C	$L_{us}(\lambda)$
type D	$\varepsilon(\lambda)L_T(\lambda)\tau_2(\lambda)$
type E	$FE_{d\varepsilon}(\lambda)\frac{r_d(\lambda)}{\pi}\tau_2(\lambda)$
type F	$L_{u\varepsilon}(\lambda)$
type G	$(1-F)L_{bs}(\lambda)r_d(\lambda)\tau_2(\lambda)$
type H	$(1-F)L_{b\varepsilon}(\lambda)r_d(\lambda)\tau_2(\lambda)$

where $E_s'(\lambda)$ is the exoatmospheric solar irradiance, units in $W/(m^2\mu m)$;

σ' is the solar zenith angle measured from the target normal;

$\tau_1(\lambda)$ is the atmospheric transmission along the sun-target path;

$\tau_2(\lambda)$ is the transmission along the target-sensor path;

$r(\lambda)$ is the reflectance of the target;

$r_d(\lambda)$ is the reflectance of the target if it is assumed diffuse (constant with angle);

π is the irradiance to radiance conversion factor;

$\varepsilon(\lambda)$ is the target emissivity;

$L_T(\lambda)$ is the spectral radiance $[W/(Sr\ m^2\mu m)]$ for a blackbody at temperature

T;

F is the shape factor for the background (if the target can be assumed to be approximately Lambertian);

$E_{ds}(\lambda)$ is the solar scattered downwelled irradiance;

$E_{d\varepsilon}(\lambda)$ is the atmospheric scattered downwelled irradiance;

$L_{bs}(\lambda)$ is the solar reflected background radiance;

$L_{b\varepsilon}(\lambda)$ is the spectral radiance from the background due to self-emission;

L_{us} is the solar upwelled radiance;

$L_{u\varepsilon}(\lambda)$ is the upwelled radiance due to self-emission from the atmosphere along the line of site.

To rapidly extract these components for use in general propagation calculations for different reflectance spectra and utilize the output from MODTRAN run, Schott's Equation 4.37 is simplified. Assuming the target is horizontal and unobstructed such that the entire hemisphere above the target is sky (fully exposed horizontal surface), and ignoring the background self-emission, the generalization and simplified version of the equation for the radiance reaching a sensor can be expressed as:

$$L = (Direct\ Reflected\ Radiance) + (Diffuse\ Reflected\ Radiance) + (Path\ Radiance)$$

$$(4.38)$$

Using wavelength dependent radiometric terms we have

$$L_\lambda = \frac{E_s'(\lambda)}{\pi} \cos \sigma' \tau_1(\lambda) r(\lambda) \tau_2(\lambda) + \frac{E_{ds}(\lambda)}{\pi} r(\lambda) \tau_2(\lambda) + L_{us}(\lambda) + L_{adj}(\lambda) \quad (4.39)$$

where $L_{adj}(\lambda)$ is the adjacent radiance scattered into the field of view.

The *Direct Reflected Radiance* in equation 4.38 represents the radiance that

comes from the solar irradiance interacting with the target and reflected to the sensor (A in Fig. 4.18). For a reflectance of 1.0, the term will contain the following

$$\frac{E'_s(\lambda)}{\pi} \cos \sigma' \tau_1(\lambda)\tau_2(\lambda) \tag{4.40}$$

Diffuse Reflected Radiance represents the radiance that comes from the down-welling sky and reflected by the target to the sensor. For a reflectance of 1.0, the term will contain the following

$$\frac{E_{ds}(\lambda)}{\pi}\tau_2(\lambda) \tag{4.41}$$

Path Radiance, also known as upwelled radiance, represents the radiance due to the atmospheric path, and is a portion of the signal reaching the sensor that has not interacted with the target.

$$L_{us}(\lambda) + L_{adj}(\lambda) \tag{4.42}$$

Take into account the strong signal from the target, the radiance reaching the sensor due to the target self-emissivity ε is:

$$L_t(\lambda) = L_{target}(\lambda)\varepsilon(\lambda)\tau_2(\lambda) \tag{4.43}$$

With knowledge of all these radiometric parameters, the target leaving radiance reaching the sensor could be expressed as:

$$L_\lambda \;=\; \frac{E'_s(\lambda)}{\pi}\cos\sigma'\,\tau_1(\lambda)\tau_2(\lambda)r(\lambda) + \frac{E_{ds}(\lambda)}{\pi}\tau_2(\lambda)r(\lambda) + L_{us}(\lambda) + L_{adj}(\lambda)$$

$$+\; L_{target}(\lambda)\varepsilon(\lambda)\tau_2(\lambda) \tag{4.44}$$

The colored component radiances are computed using MODTRAN at the viewing zenith angle of the sensor relative to the target, and with aerosol characteristics specified using the standard rural model. The atmosphere was assumed to be mid-latitude summer with 23 km visibility. Upwelling radiance is estimated by subtracting the total ground reflected radiance $GRND\_RFLT$ from total radiance reaching the sensor $TOTAL\_RAD$, for a target ALBEDO of 1.0, which assumes that the target reflects 100% of incident radiance. $L_{target\lambda}$ is the radiance from ground target. For this research the radiance and temperature from fire and burn scar are of key interest. Taking fire as blackbody with typical highest temperature of 1100K, the radiance of a 1100K blackbody is substituted for $L_{target\lambda}$ in Eq. 4.44. Along with the MODTRAN predicted radiometric parameters, the radiance from a blackbody is cascaded together with the atmospheric transmission spectra to yield the spectral radiance reaching the sensor, as shown in Fig. 4.19. These spectra show how different absorbers are affected in different wavelength regions; (a) shows the downwelling solar irradiance at the altitude of the observer, which agrees well with ideal blackbody at temperature of 300K, (b) is the transmission from ground to sensor at altitude of 4.2km, (c) is the total radiance of 1100K blackbody reaching the sensor, and (d) is the comparison of BB radiance before and after atmospheric attenuation. The black curve is the radiance from an ideal blackbody at a temperature of 1100K, the red one is the radiance reaching sensor after atmospheric attenuation. It is obvious that land

leaving radiance contributes more in the visible and NIR bands. From the short-wave IR to long-wave IR there are several orders of magnitude more flux from the blackbody radiance than from the sun. Fire dominates in the mid-wave IR and long-wave IR region, which accounts for the use of these bands for fire detection. The molecules that account for most of the absorption in the IR region are H_2O, CO_2, NO, O_3, CO, and CH_4. The major absorption bands are due to H_2O and CO_2.
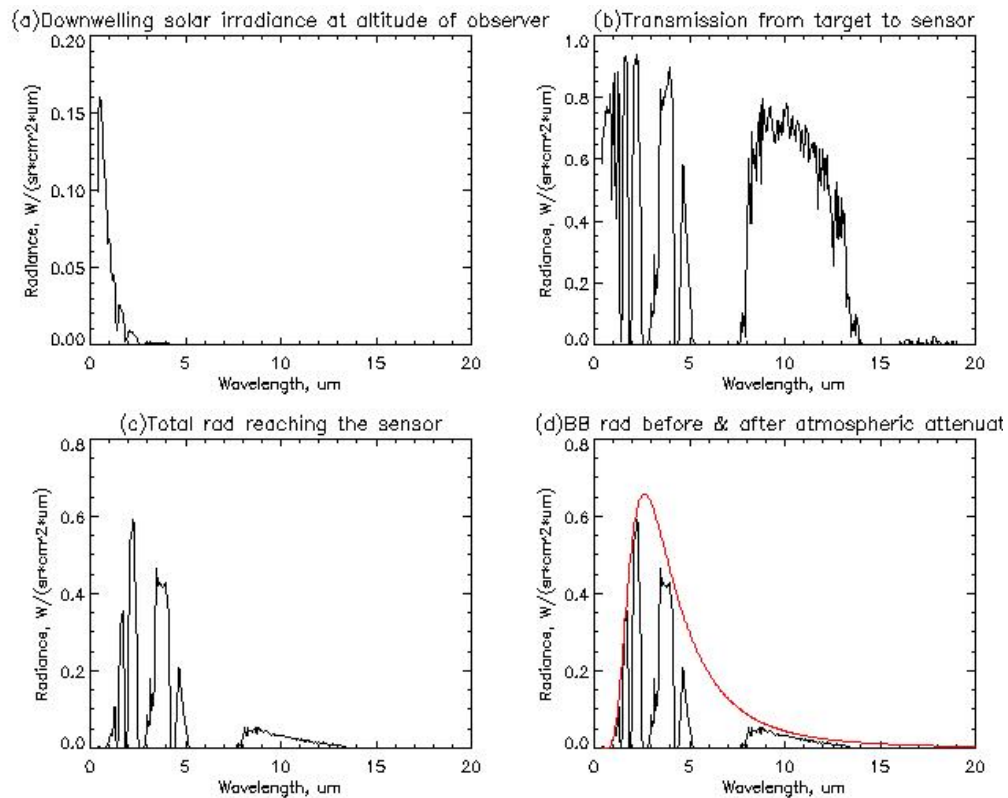

Figure 4.19: Atmospheric prediction of 1100K blackbody spectral radiance reaching the sensor at 4200m altitude. (a)Downwelling solar irradiance at the altitude of observer. (b)Transmission from target to the sensor. (c)Total radiance reaching the sensor. (d)BB radiance before and after atmospheric attenuation.

MODTRAN is based on empirical measurements and physics modeling. MOD-
TRAN is 'band model' implementation of HITRAN database which contains over
1 million spectral absorption lines for 38 gaseous constituents of the earth's atmo-
sphere, along with absorption cross sections for 27 additional molecules (Myers
et al., 2004). MIE code is used to calculate aerosol scattering. As a first princi-
ple physics based model, MODTRAN has been extensively verified and validated
against measurement data from interferometer, balloon, and airborne imagery.
The MODTRAN-based atmospheric prediction/compensation described above
will be used to evaluate the synthetic hyperspectral image generated by DIRSIG,
and the retrieval of apparent surface temperature. More discussion on these topics
will be included in Chapter 6.

4.8   Software Layer

The real time simulation of many ground level and atmospheric scenarios is a
computationally heavy mission. To distribute computation and utilize all avail-
able computer resources without affecting other people's job, CONDOR is intro-
duced in this work. Condor is a software system for managing compute-intensive
jobs. "It effectively utilizes the computing power of workstations that communi-
cate over a network" (University of Wisconsin-Madison, 2006). After submitting
a job, Condor will find available idle machines on the network and begin running
the job on the machines. It has the capability to move (migrate) the jobs from
unavailable machines to the idle ones, checkpoint the job and continue the job on
the new machines from exactly where the job left off. Being able to preserve the
local execution environment via remote system calls, Condor doesn't require user
to change the source code or make data files available to remote workstation. The

job attributes and requirements are bundled up into a job ClassAd. Condor plays
the role of 'matchmaker' by continuously reading all the job ClassAds and all the
machine ClassAds, matching and ranking job ads with machine ads, and making
certain that all requirements in both ClassAds are satisfied. This implementation
enables the users to increase their computing throughput.
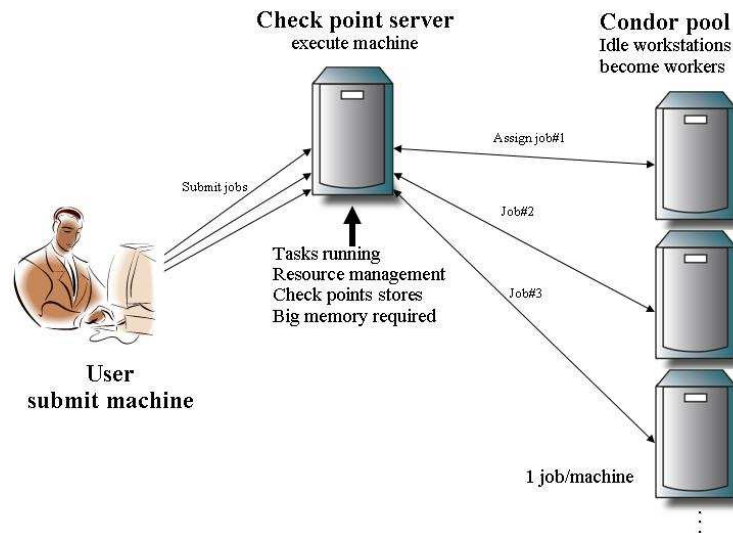
Figure 4.20: Condor grid job submission.

The user submits the job to the check point server which works as 'traffic cop'
(Fig. 4.20). It would announce work to the condor pool where all the working
computers are, assign one job to one computer. When there is new user submit-
ting jobs, the server will save the check point, and resend the job once there are
computers announced as free. So the server requires large memory to hold all the
idle information. Condor will make certain there is only one job running in one
machine.

Chapter 5

Fluid Dynamic Models of Fire

Numerical heat transfer and fluid flow models can solve equations describing conservation of mass, momentum, and energy. These models are applied to calculate sets of variables representing characteristics of a combustion process over time. Applications include wildfire modeling, structural fire modeling, and combustion modeling of furnaces based on different fire types (Table. 5.1).

A structure fire is a fire in any of various residential or commercial buildings. It is in contrast to wildfires or other outside fires. Structural fire modeling
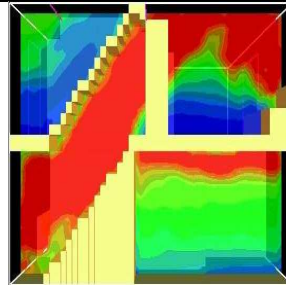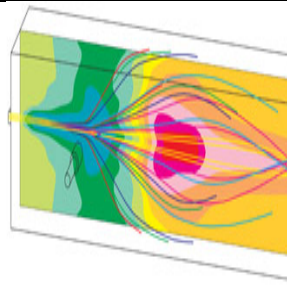
models	wildland fire	structural fire	furnace combustion
figure			

Table 5.1: models from left to right: wildfire, structural fire, furnace combustion.

combines computational fire modeling with structural modeling using the finite element method to predict more accurately the behavior of buildings on fire (more accurate estimation of the structural response over the full duration of the defined fire). Representative boundary conditions are utilized, leading to improved computational efficiency. Material behavior at elevated temperatures, material safety factors, and significant structural contribution should be taken into account. Localized behavior may not be modeled accurately in whole building modeling. The University of Manchester and NIST have been doing the research on structural fires.

A furnace or direct fired heater is used to provide heat for a process or can serve as reactor which provides heat of reaction. An air blower provides air to mix with fuel flows circulation inside the furnace. Proper air/gas mixture ratios are important for fuel efficiency. The Glass Furnace Model (GFM) was developed at Argonne National Laboratory and has been extensively validated against a comprehensive database acquired from in situ measurements in furnaces.

Current wildfire models differ in complexity and origin. They range in complexity from simple algebraic models to complex formulations that require vast computational resources (Linn *et al.*, 2002). Besides the coupled atmospheric transport-wildfire behavior model FIRETEC (Linn *et al.*, 2002; Linn, 1997), there are fast-running operational models like Fire Area Simulator (FARSITE) (Finney, 1998) which simulates fire behavior and growth, Fire Behavior Prediction and Fuel Modeling System (BEHAVE) (Andrews, 1986; Grabner *et al.*, 2001), Rare Event Risk Assessment Process (RERAP), Wildland Fire Situation Analysis (WFSA), Fire Effects Information System (FEIS), Fire Monitoring Handbook Software (FMHS) (National Park Service, 1999), and the NEXUS model which

computes surface, transitional and crown fire behavior. A slightly different model is the First Order Fire Effect Model (FOFEM) that predicts tree mortality, fuel consumption, smoke production, and soil heating caused by prescribed fire or wildfire. Fig. 5.1 lists a hierarchy of fire models in order of complexity. The level of complexity required depends on the application.

A Hierarchy of 'Models'

Experience, Intuition

BEHAVE

FARSITE

Modeled (mesoscale) winds used as input to BEHAVE

NCAR Coupled Atmosphere-Fire Model

Los Alamos FIRETEC

Full combustion treatment

Increasing complexity
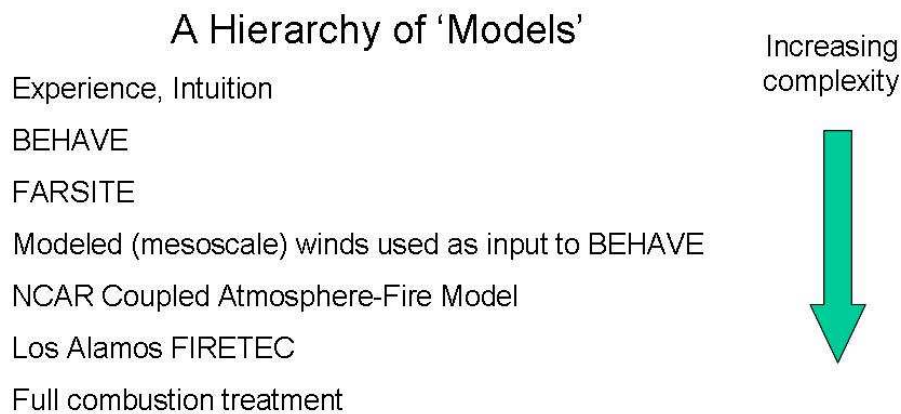
Figure 5.1: A hierarchy of wildfire modeling.

The fire behavior models studied in this research include the Fire Dynamics Simulator (FDS) and NCAR's Coupled Atmosphere-Fire Model. Both of them predict the fire-induced flow, and give raster representations of spatial physical properties for the burning and burned area with time.

5.1   Fire Dynamics Simulation Model

Fire Dynamics Simulator (FDS) is a computational fluid dynamics (CFD) model of fire-driven fluid flow. It solves numerically a form of the Navier-Stokes equations appropriate for low-speed, thermally-driven flow with an emphasis on

smoke and heat transport from fires (McGrattan *et al.*, 2007). The growth of fire is very sensitive to the thermal properties of the surrounding materials. The result of this model might differ a little if there are more materials in computational region. The model can simulate highly detailed small scale indoor fires (the grid size can be as small as sub-centimeter) and large scale wildfires. Time-velocity and time-temperature are generated at a regular 3D grid of position. FDS is said to be able to predict flow velocities and temperatures to within 20% of the experimental measurement. Fig. 5.2 is the temperature field side views from perpendicular directions of a pool fire within space of 0.6m x 0.6m x 1.2m simulated by FDS. Fig. 5.3 shows the horizontal cross section of velocity field from perpendicular directions of the pool fire.
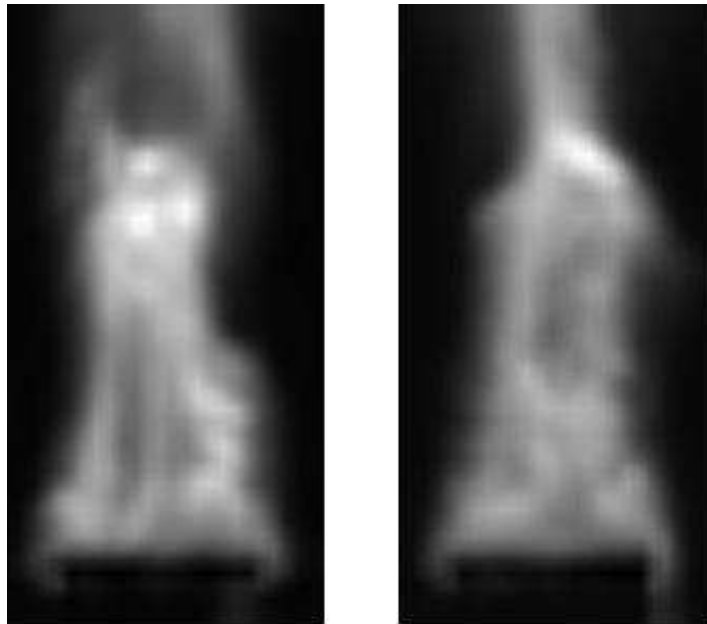
Figure 5.2: Side view of temperature field from perpendicular directions simulated by FDS.
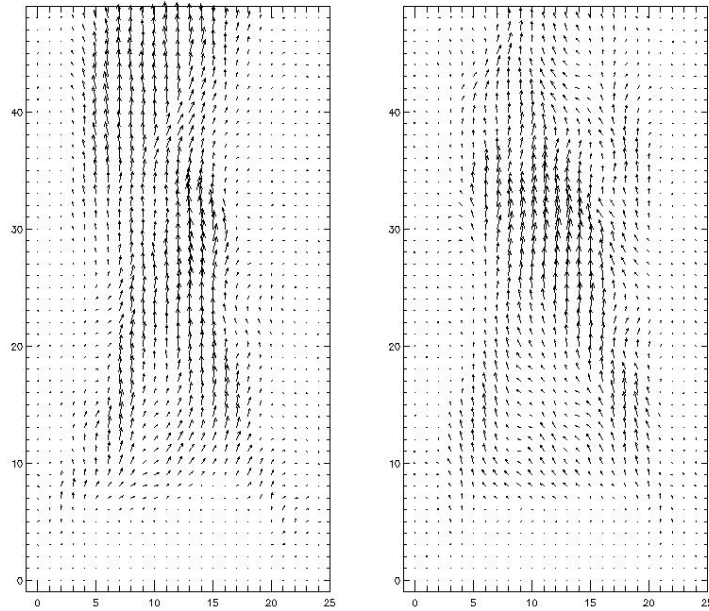
Figure 5.3: Horizontal cross section of velocity field simulated by FDS

The length of time FDS takes to run a simulation depends on the resolution of the physical domain and how much combustion is taking place within the domain. For the simulations of grassland fires which are 1500m x 1500m x 200m in general, 16 million grid cells and 11 processors are required. The smaller the numerical grid (i.e., the higher the spatial resolution) the longer the simulation will take to run. In addition, as more grid cells become involved in the combustion process (as with a growing fire), the processing time will increase. 'For most of the cases considered 44 cpu hours were needed for 100s simulated time (i.e., all 11 processors running for 44 hours on 1.8 GHz processors)' (Mell *et al.*, 2007). Although FDS is actually very fast as a computational fluid dynamics (CFD) code involving so many cells and processes, the length of time it takes to run a simulation is too long to meet our requirements of real-time measurement and

prediction for wildfire propagation. Beside the time concern, FDS is not capable of simulating fires on complex terrain which is highly possible for wildfires. So in this research FDS won't be used to predict fire propagation.

5.2   Coupled Atmosphere-Fire Model

The Coupled Atmosphere-Fire model is developed by National Center for Atmospheric Research (NCAR) to investigate the dynamics of wildfires through physically-based modeling. The model has a sophisticated high-resolution non-hydrostatic numerical mesoscale atmospheric model that solves prognostic fluid dynamics equations of motion for air momentum, a thermodynamic variable, water vapor and precipitation. This 3D atmospheric prediction model (Clark and Hall, 1995; Clark *et al.*, 1996a,b; Coen *et al.*, 2001) is coupled with an empirical fire spread model (Rothermel, 1972; Mandel *et al.*, 2004b). Rothermel's method generates fire behavior data for a given set of weather and fuel moisture data inputs. Local fire spread rates depend on the modeled wind components. The output values of each cell in the study area represent how the fuels will be burning under certain landscape, weather, and environmental conditions. The atmospheric winds drive the fire propagation and the heat and moisture fluxes from the fire are predicted and then fed back to the atmospheric dynamics allowing the fire to influence its own mesoscale winds that in turn affect the fire behavior (Clark *et al.*, 2004; Mandel *et al.*, 2004a). The time the fire takes to establish convective heat balance varies from case to case. In the coupled model, the time is between 1 and 2 minutes. For the simulation it was about 30:1, which means 30 seconds on a single processor are needed to simulate 1 second burning. This run time is fast to meet our requirement of real-time measurement and prediction for

wildfire propagation. The coupled model can represent the complex interaction between large scale wildfires and local winds.

In this research, the Coupled Atmosphere-Fire Model is used to simulate the dynamics of a small wildland fire. The simulation is the line ignition of a fire propagating over a small hill with tall grass and chaparral fuel. The output physical quantities include 2D heat flux, 2D fuel loading, 3D buoyancy field, velocity, vorticity, and etc. The solution is achieved by representing the field on regular grid. The ground grid dimensions in this case are 140 x 140, with a horizontal grid spacing of 20 m x 20 m. The whole simulation includes 830 time steps each 6 seconds apart. Fig. 5.4 shows the surface fire sensible heat flux and fuel loading respectively, from model output.
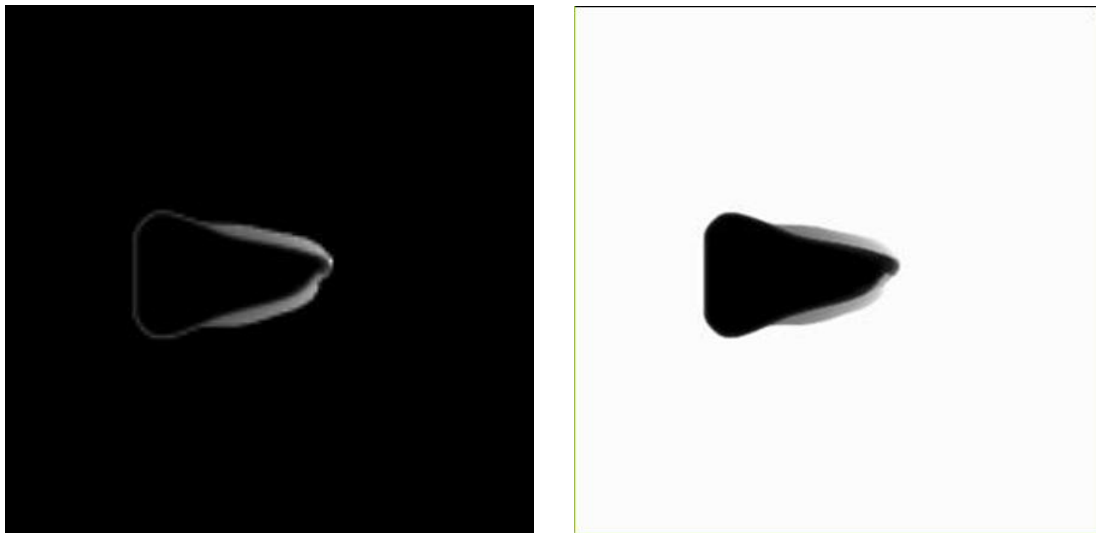
Figure 5.4: The Coupled Atmosphere-Fire model output. (Left) Heat flux 3672 seconds after ignition. (Right) Fuel loading 3672 seconds after ignition. In both cases, white represents high values.

Fig. 5.5 and Fig. 5.6 show the side view, front view, top view, and perspective view of the 3D buoyancy field.
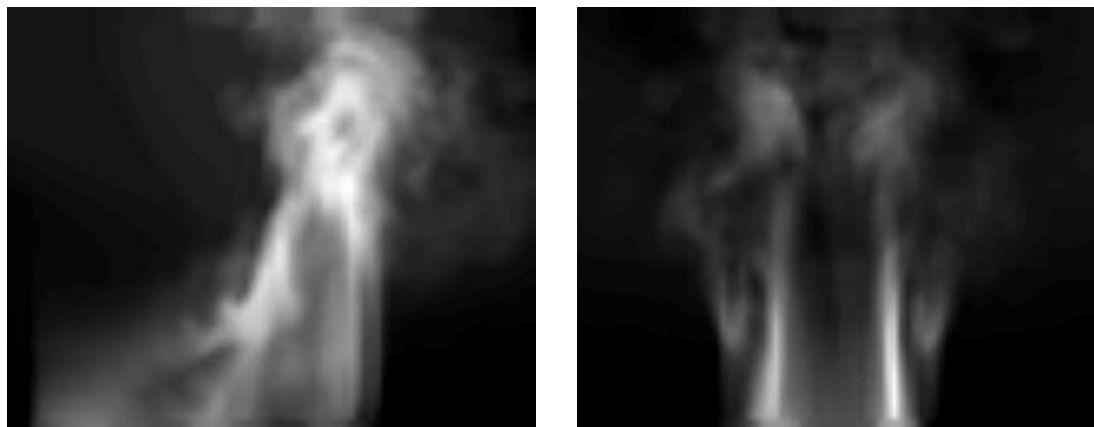
Figure 5.5: The Coupled Atmosphere-Fire model output. (Left) Side view of buoyancy plume 3672 seconds after ignition. (Right) Front view of buoyancy plume 3672 seconds after ignition.
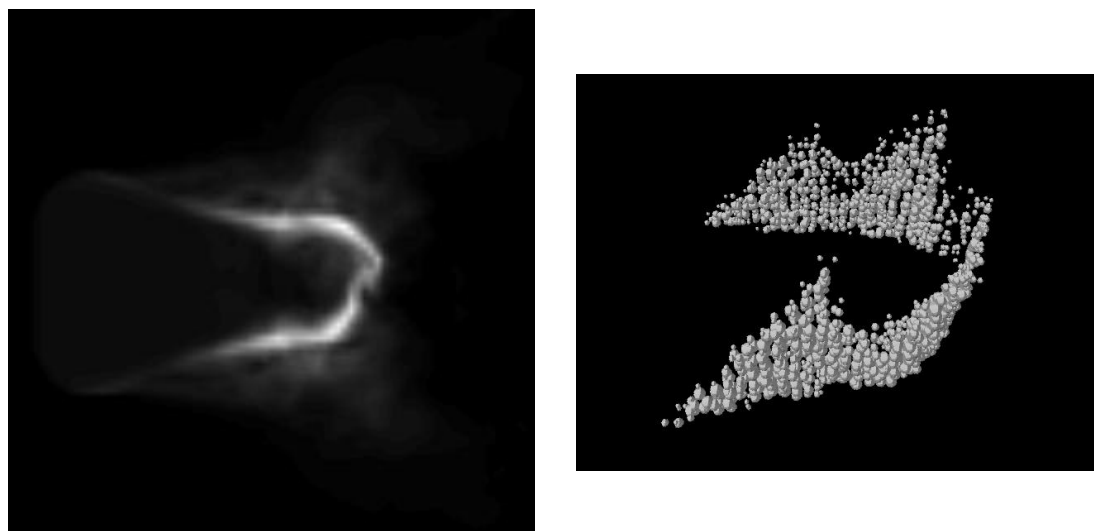
Figure 5.6: (Left) Top view of buoyancy plume 3672 seconds after ignition. (Right) Perspective view of sphere representation of 3D buoyancy.

Chapter 6

Results

Given the general approaches introduced previously, results from radiometric modeling and visualization of wildland fire are reported. Section 6.1 gives the fire radiance characteristics from spectroradiometric measurements. Section 6.2 shows the predicted burn scar time-temperature. In Section 6.3, Section 6.4, and Section 6.5 the visualization of 3D fire with a regular grid of voxels, adding secondary point sources, and the final generic radiometry approaches are exhibited, respectively. Finally, Section 6.6 verifies our synthetic radiometry by calculating Fire Radiative Energy (FRE) and comparing the synthetic results to those estimated from satellite images.

6.1   Fire Radiance Characteristics

6.1.1   ASD Spectroradiometer

In the experiment conducted in Missoula, Montana, the length of the fuel bed was varied from 0.305 meter to 2.743 meter to study the change of fire

radiance on flame thickness. We used the ASD to observe the flame radiance from 350nm to 2500nm. The ASD was optimized with a 1100K blackbody before the measurement to reach the best sensor performance and avoid detector saturation. The solid curve in Fig. 6.1 (a) is the observed radiance from a fire with a thickness of 2.438m. The gap at about 1000nm maybe due to different gains and responses of the ASD sensors, or the non-random field of view of the fiber bundle. The fire spectral radiance was compared to blackbody radiation to obtain temperature. The dashed curve is blackbody radiation at 1700K, scaled to generally match the radiometer spectrum. The two lines match reasonably well from visible region to NIR. At wavelengths longer than 1.8μm the spectral match is not so good, in part due to difficulty in setting the sensor gains and avoiding the detector saturation. This result suggests that as a first approximation, fire is a blackbody radiator, and the flame temperature is higher than that from the thermocouple measurement.

(a) 2.5m fire radiance vs. blackbody of 1700K   (b) Potassium emission
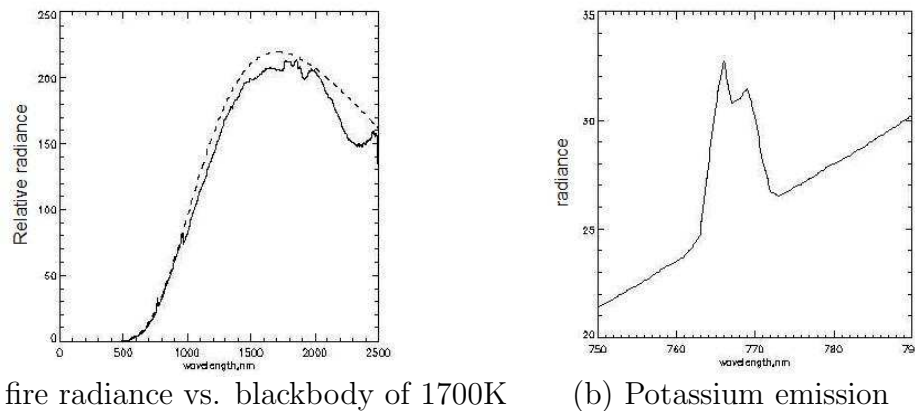
Figure 6.1: ASD measured fire spectrum

For all the test fires the radiance between 1000nm and 1500nm increases smoothly and fits the blackbody radiance so we used this part of the ASD data

for comparison and analysis. Radiance at 1200nm for all test fires are extracted and plotted in Fig. 6.2. Fire radiance increases almost linearly with fuel bed length from 0.305 meter to 2.438 meter. For a 2.743-meter large fire, the radiance doesn't increase further. The result suggests that small fires are transparent or semi-transparent and the observed radiant emission is the accumulation from all parts of the flame. Fires become more opaque when they are thicker than about 3m.
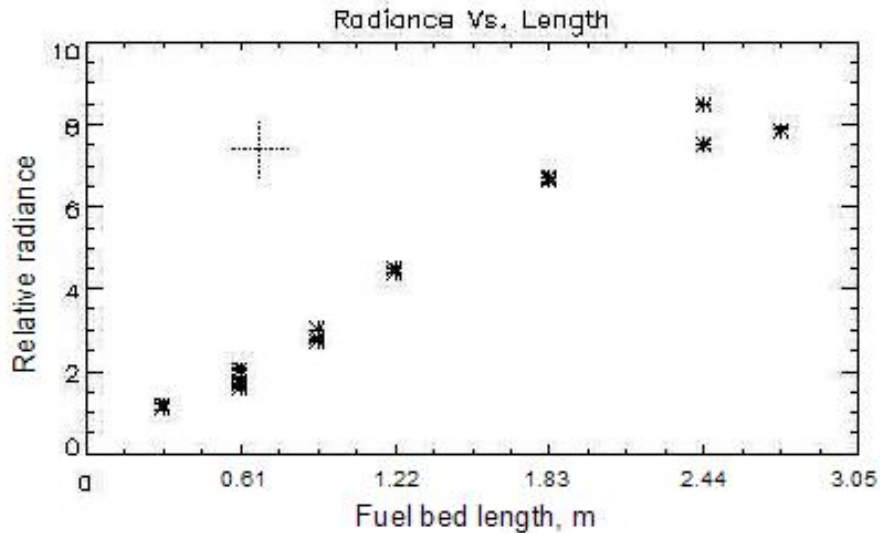
Figure 6.2: Radiance as a function of fuel bed length

The ASD FieldSpec has a spectral resolution of about 3nm, which is sufficient for characterizing the potassium emission observation. Fig. 6.1 (b) is the zoom-in of radiance from an 2.4m thick fire. The two peaks in the curve correspond to K lines at 766.5nm and 769.9nm. It is possible to simulate the Potassium emission radiance in the synthetic image, although that was not done for the synthetic scene generated in this work. The intensities of Potassium emitted lines depend

upon the population of the ionized atoms. To compute the power associated with line emissions, we need to estimate the amount of ionized potassium atoms present in a specific flame. Combined Saha-Boltzmann equation is used to calculate expected line intensities for Potassium emission. See Appendix A for steps calculating the expected line intensities for potassium emission.

6.1.2 IR Systems Spectroradiometer

A high resolution IR System Spectroradiometer was used to investigate the molecular line emissions in fire radiation. A 20cm-thick test fire was observed as close as 2m. In Fig. 6.3, (a) is the fire spectra showing the water vapor and CO_2 lines for the close range view. There are strong H_2O emission centered roughly on 1.5μm, 2.0μm, and 6.5μm, strong and wide CO_2 emission centered roughly on 2.6μm and 4.3μm. In (b) the fire spectra is compared to a blackbody radiation at 800^oC. The overall shape of fire radiation agrees with blackbody radiation except the unique combinations of gas signatures in fire. The lower curve in Fig. 6.5 is the thermal emission of the 1100K hot atmosphere calculated by the atmospheric propagation model MODTRAN. The fire and the hot atmosphere have the similar emission lines since they are both dominated by water vapor and carbon dioxide. However, these molecule radiation is not seen remotely because of absorption by the same cool gasses in the intervening atmosphere.
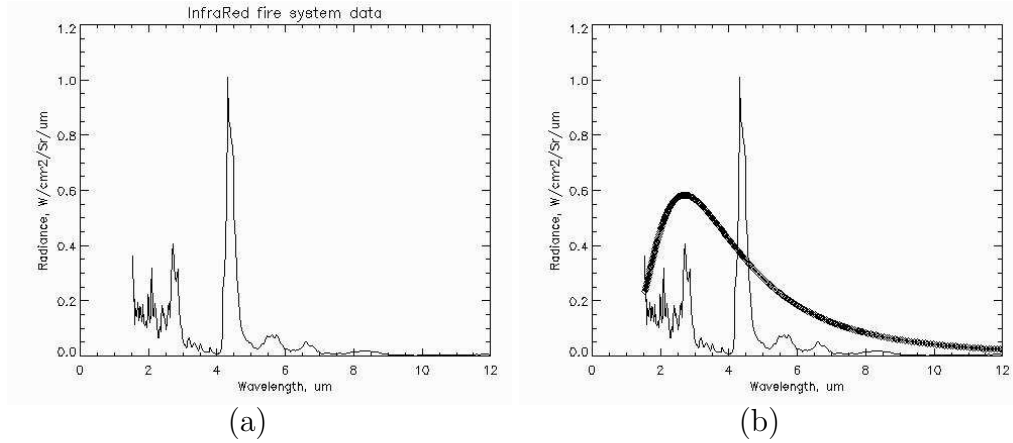
Figure 6.3: Fire radiation measured with IR Systems. (a) fire spectral radiation showing the water vapor and CO_2 lines. (b) fire radiation vs. blackbody radiation at 1153K.

6.2 Ground Temperature Prediction

To correctly label the fire front, burn scar, and unburned area for remote sensing scene generation, the 2D surface fire sensible heat flux from the Coupled Atmosphere-Fire Model output is utilized to give a dynamic demonstration of combustion area temperature evolution. Heat flux is proportional to the temperature difference, so the fire edge exists where there is large heat flux. A threshold of 1000 (the highest heat flux is $5.92 * 10^6 W/m^2$ in this simulation) is set for the heat flux data to record pixels with large temperature differences and extract fire edge. The pixels with heat flux greater than threshold are marked as 'burning' (fire front) and assigned temperature of $800^o C$. Pixels with heat flux greater than 0 and less than the threshold are marked as 'hot' which is the burn scar. The burn scar for any specific time step after ignition is the total burned area from all the previous time steps and labeled with the following logic

$$burned = current\ hot \bigotimes previous\ burning \bigoplus previous\ burned$$

The time temperature variation of the burn scar is calculated with Eq. 4.18. Unburned areas are the pixels where there is zero heat flux and no temperature difference. They are assigned ambient temperature 34^oC. Fig. 6.4 shows the temperature map at different times after ignition. The white area is the fire front. The brighter the area, the higher the temperature. The pixels getting darker are the areas where fuels are consumed and the fire is dying out. Each pixel goes through three distinct phases: ignition, burning and cooling down, and burn out. In Fig. 6.4 the fire perimeter is brighter in the front (leading downwind edge of the fire which is moving left to right), which means the temperatures of the fire front are higher than the backing fire. Bailey and Anderson (1980) reached a similar conclusion, 'Fire temperatures were significantly higher in head fires than in backfires'.
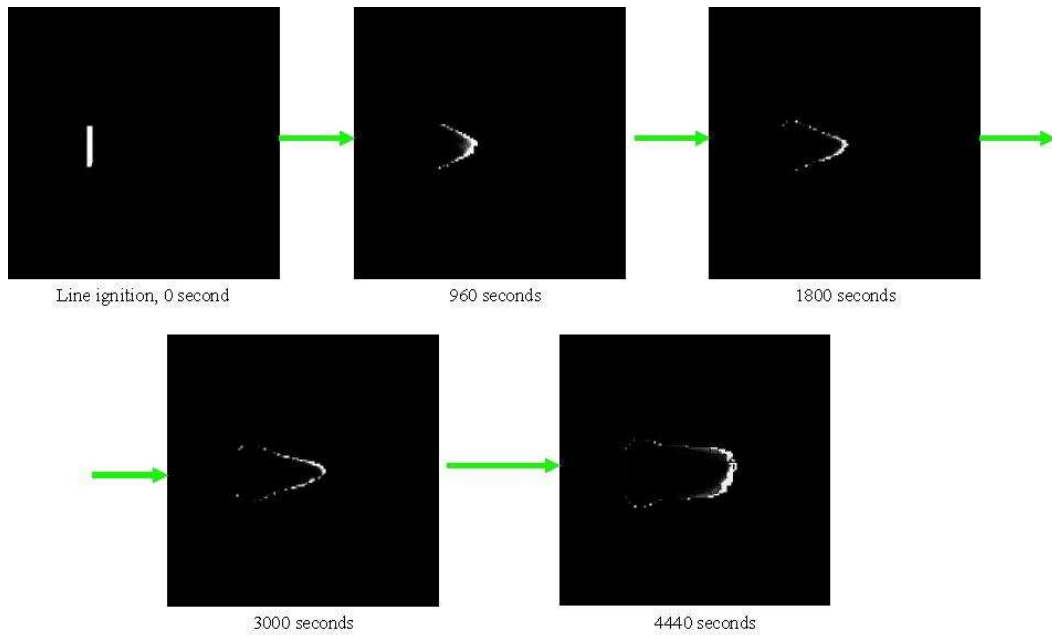
Figure 6.4: Fire perimeters with line ignition at times of 0, 16, 30, 50, and 74 minutes respectively.

6.3 Voxel Flame

To visualize transparent and semi-transparent flame and smoke volume, step-wise integration and the regular grid method introduced in Section 4.3 were used. The volume is gridded into many regular voxels. Each voxel in the system has the following attributes:

- Position
- Temperature
- gas concentration
- emissivity

The emissivity from each voxel is required to collect its transmitted radiance

reaching the sensor. The emissivity ε is calculated as follow:

$$
\begin{aligned}
\varepsilon &= 1 - \tau \\
&= 1 - e^{OpticalDepth} \\
&= 1 - e^{PathLength * extinction} \\
&= 1 - e^{PathLength * absorption * concentration}
\end{aligned}
\tag{6.1}
$$

where τ is the transmission of the voxel. The question left is how to calculate the absorption for flame and fuel gas. Since particles emit and absorb photons at the same wavelengths, the particle absorption could be approximated by calculating the particle emission. The atmospheric propagation model MODTRAN is used to determine emitted and scattered radiances. In the MODTRAN configuration, the sensor is placed at 8 meters high above the ground, the boundary temperature is set to 1100K which is the typical temperature of biomass fire. The sensor is surrounded by hot air in this setting. Without knowledge of exact amount of trace gases in the flame, the flame emission is assumed to be the same as hot air thermal emission and will be dominated by water vapor and carbon dioxide. The lower curve in Fig. 6.5 is the thermal emission term of the path radiance calculated by MODTRAN, the upper curve is the total target to sensor transmission. The spectral path transmission is opposite the spectral thermal emission, the dips in transmission correspond to the spikes in emission. The MODTRAN run testifies the correspondence of the particle's emission and absorption. In conservation of energy there is

$$
absorption + scattering + transmission = 1
\tag{6.2}
$$

For this case the scattered radiance is only 4% of the thermal emission. So to simplify the calculation the scattering within flame is set zero and the absorption is approximated by $1 - transmission$. The absorption has the same spectral overall shape as thermal emission.
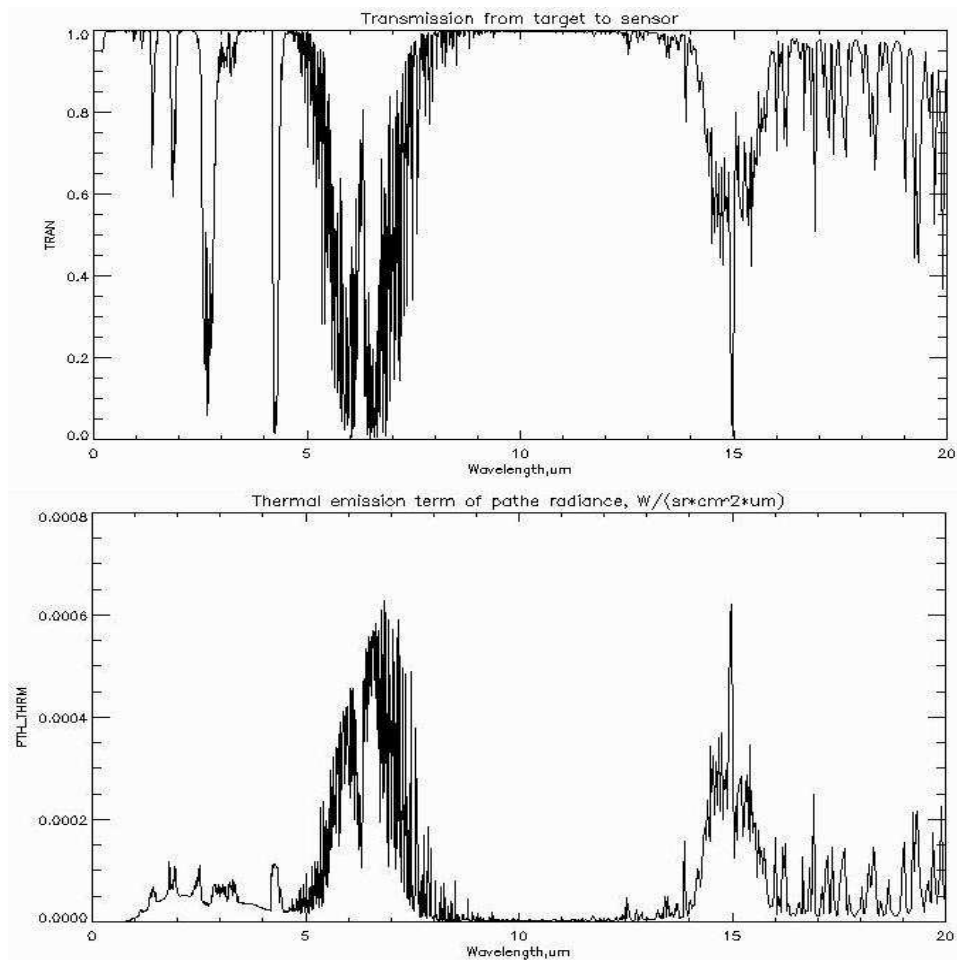
Figure 6.5: The upper curve is the transmission from target to sensor with surface albedo of 0. The lower curve is the thermal emission term of the path radiance with the boundary temperature of 1100K.

With the knowledge of position, temperature, concentration, and emissivity,
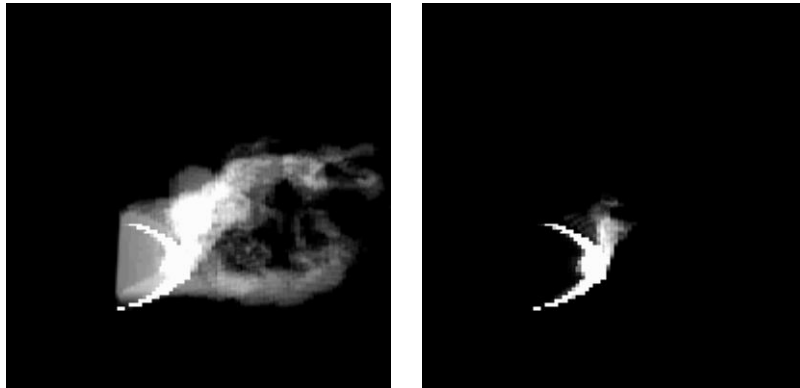
Figure 6.6: Synthetic remote sensing scenes of buoyancy plume at wavelength 3 μm. Left: more buoyancy grids involved. Right: less buoyancy grids.

the flame volume can be visualized with proper radiometry using DIRSIG. See Appendix C for DIRSIG setup for voxel rendering. The Coupled Atmosphere-Fire model is used to give 3-dimensional buoyancy plume which demonstrates the buoyancy evolution of a tall grass fire on flat terrain. Fig. 6.6 shows the synthetic slant view of buoyancy plume after 636 seconds of ignition at zenith angle 27°. The left view has lower threshold for buoyancy data and more voxels involved. The right one has higher threshold for buoyancy data and fewer voxels involved. Both of the visualizations are at wavelength 3 μm. Fig. 6.7 shows the synthetic spectrum of hot ground and flame pixels, respectively.

Having the 3-dimensional structure of the object we are able to view the target from different view angles. Fig. 6.8 shows the synthetic slant view and top view of buoyancy plume in the near infrared, and top view of buoyancy plume in the mid infrared. The fire has strong signal in mid infrared thus in the right scene we can see through the flame and observe the hot ground areas.

Fig. 6.9 shows the synthetic slant view of buoyancy plume at times 0, 16, 30, 50, and 74 minutes after line ignition. There is constant wind of 3 m/s to the
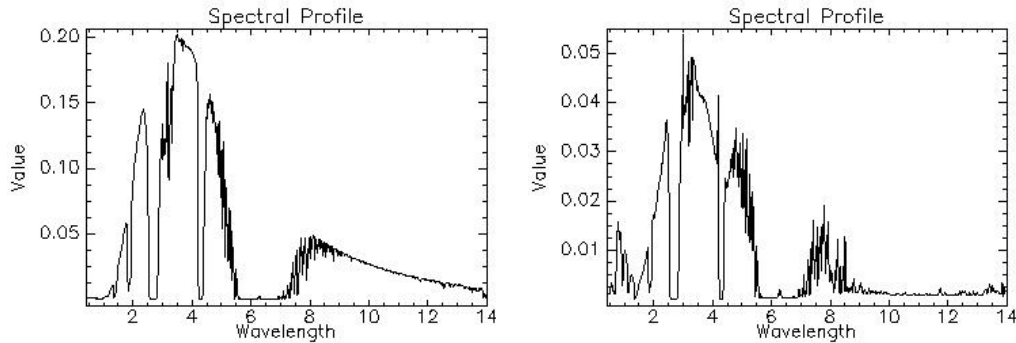
Figure 6.7: Synthetic spectrum of thermal components within the scene. Left: spectrum of hot ground pixel. Right: spectrum of flame pixel.
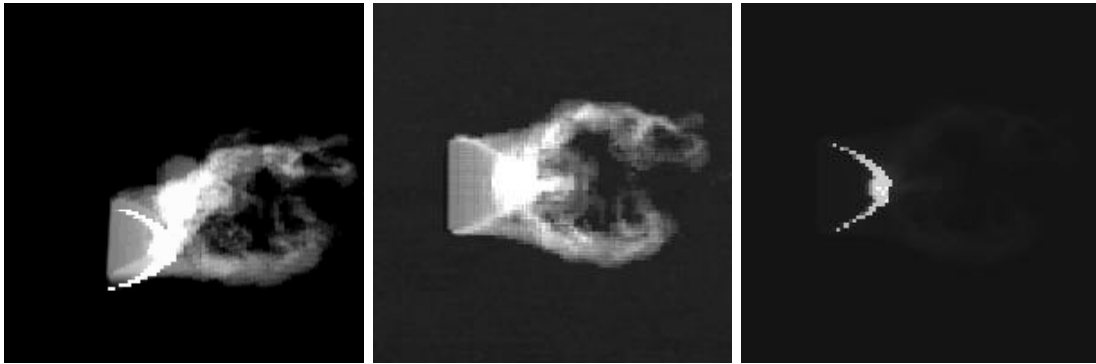
Figure 6.8: Synthetic scenes of fire and buoyancy plume at different view angles and wavelengths. From left to right: slant view at nearIR 3 μm, top view at 3 μm, top view at MIR 5 μm.

right. The fire propagates downwind and forms a finger-like fire front. There is also a backing fire slowly creeping into the wind. The buoyancy plume is tilted by the wind. Hot ground can always be seen through the flame.

In these synthetic scenes high temperature fire, flame, smoke, cooling burn scar, and background maybe present within the same image pixel. A hot pixel might be a mixture of all the thermal components and ambient background, and won't give a 'pure' activity pixel. The spectrum of a synthetic pixel is the linear combination of a set of activity components present in the pixel and the

Line ignition, 0 second

960 seconds

1800 seconds

3000 seconds

4440 seconds
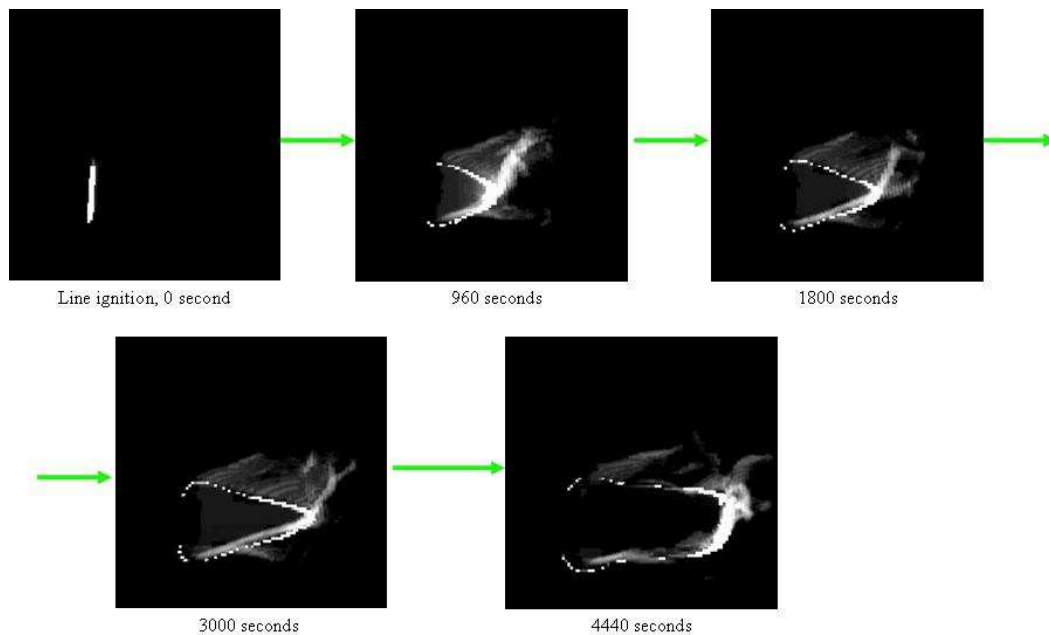
Figure 6.9: Synthetic scenes of fire and buoyancy plume at wavelength $3\mu m$ at times of 0, 16, 30, 50, and 74 minutes respectively.

radiance will be dominated by the hottest components. For example, although the buoyancy is important for some applications, with typical infrared remote sensing systems the primary target seen will be the fire itself. Subpixel analysis needs to be performed for improved target detection.

6.4 Fire as Secondary Point Source

Fire is a source of light and radiance. It illuminates and heats the surrounding by radiation. One way to illustrate this is to assume the fire as a volume composed of isotropic point sources which have isotropic angular distribution and radiate equally to all directions. Fig. 6.10 is the synthetic top view of 3D fire as secondary

source. The fire illuminates the surrounding equally. Fig. 6.11 shows the synthetic slant view of illuminating fire at times 0, 16, 30, and 74 minutes after ignition.
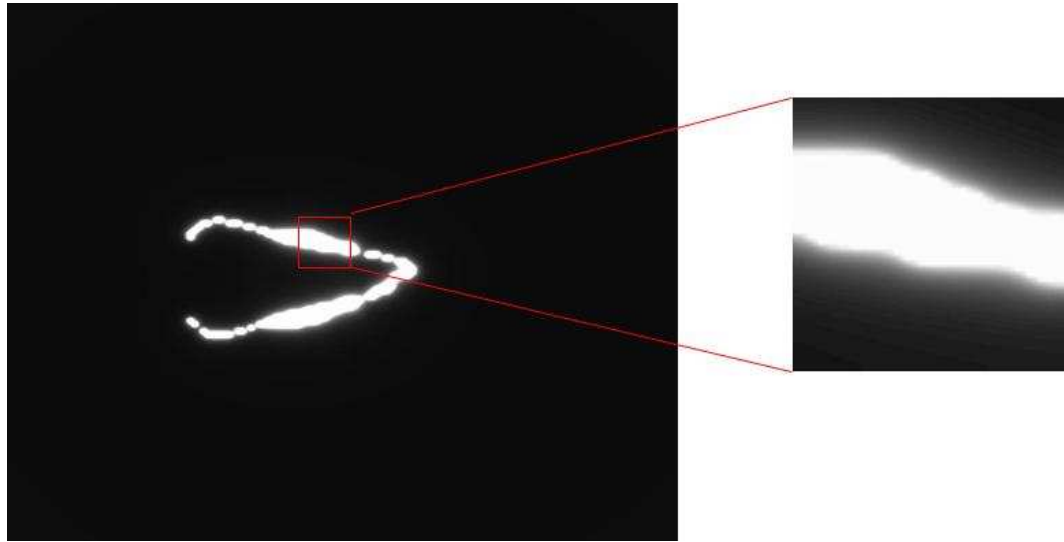
Figure 6.10: 3D visualization of fire as secondary source at 3 μm. (a) Synthetic top view of ground fire 61 min 54 sec after ignition. (b) zoomed in area.

The irradiance from a point source varies inversely with the square of the distance, which explains why the source appears to have finite extent in the image. See Appendix D for DIRSIG setup for point secondary source rendering. Although the point source rendering provides realistic visualization of the secondary source effect, it requires arbitrary scaling to produce the correct radiometry. This point source approach was abandoned in favor of the voxel rendering using DIRSIG Generic Radiometry Solver.

Line ignition, 0 second   960 seconds   1800 seconds

3000 seconds   4440 seconds
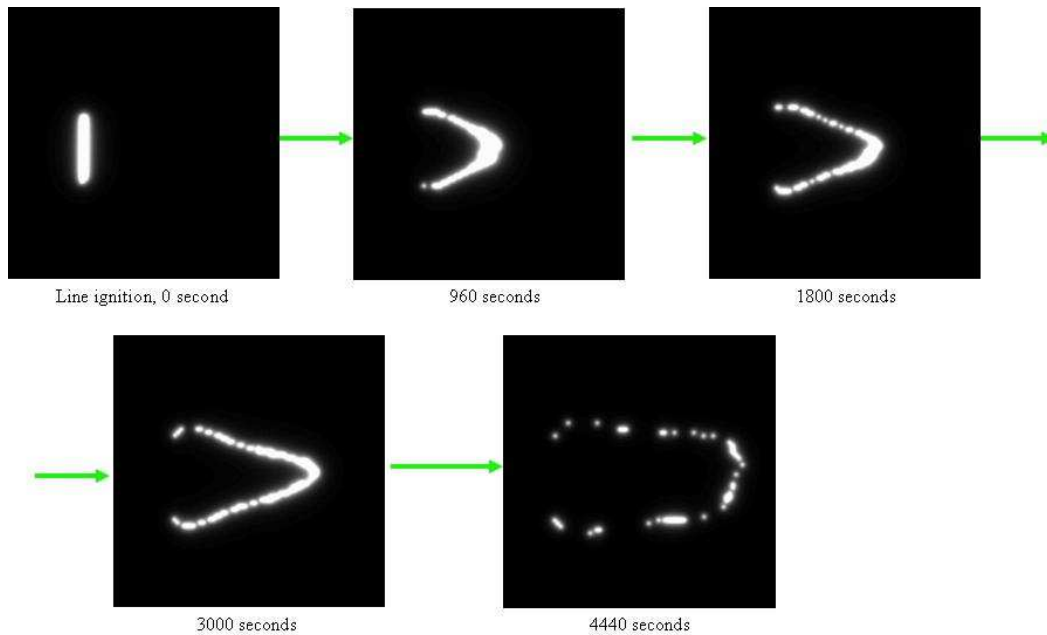
Figure 6.11: Secondary point source effect of flame at wavelength $3\mu m$ at times of 0, 16, 30, 50, and 74 minutes respectively.

6.5 Visualizing 3D Flame Geometry with the Generic Radiometry Solver

The configuration of the generic radiometry solver and the related optical properties (reflectance, emissivity, scattering and extinction properties) is defined in the material database file. See Appendix E for the DIRSIG setup. Figures 6.12 $\sim$ 6.14 are complete DIRSIG rendering of the modeled fire using the Generic Radiometry Solver. The three scenes correspond to the characteristics of three channels of the WASP sensor and include the effects of burn scar cooling, 3D radiation from the flames, the hot ground under the flame, and the radiation from the 3D flame reflected off the nearby ground. Fig. 6.15 shows a zoomed

slant view of the modeled fire volume with background reflecting radiance of the approaching hot flame. Fig. 6.16 shows the slant view of fire at times 0, 16, 30, 50, and 74 minutes after ignition. The visualizations in Fig. 6.15 and Fig. 6.16 are at wavelength 3 μm.
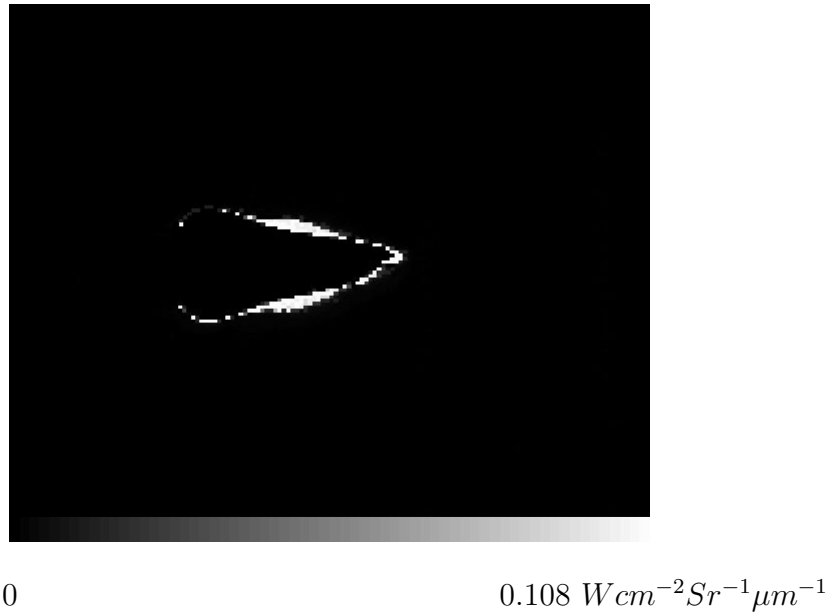
0   0.108 $Wcm^{-2}Sr^{-1}\mu m^{-1}$

Figure 6.12: DIRSIG rendering of grassfire scene with WASP sensor specification in the short-wave infrared channel, 0.9 - 1.8μm. The highest radiance is 0.108 $Wcm^{-2}Sr^{-1}\mu m^{-1}$.
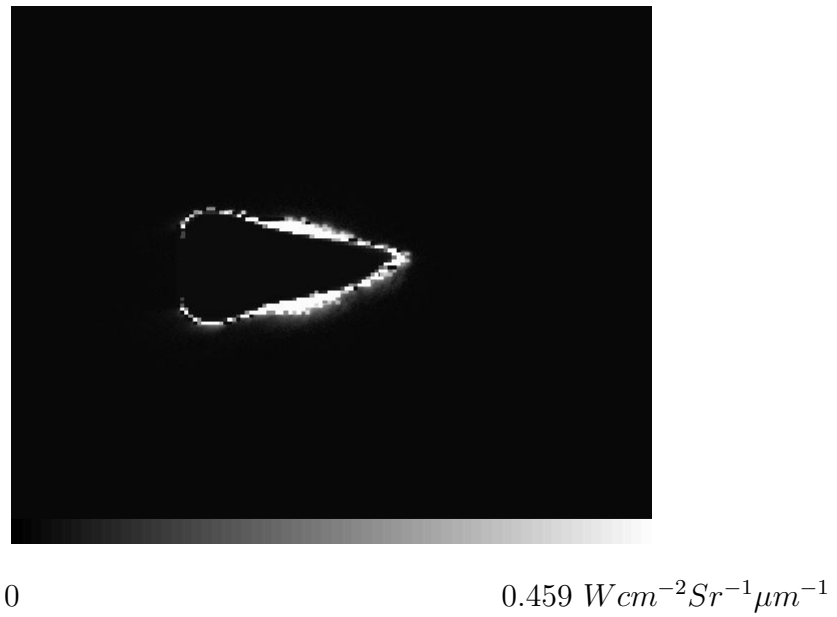
0 $0.459 \ Wcm^{-2}Sr^{-1}\mu m^{-1}$

Figure 6.13: DIRSIG rendering of grassfire scene with WASP sensor specification in the mid-wave infrared channel, 3.0 - 5.0μm. The highest radiance is 0.459 $Wcm^{-2}Sr^{-1}\mu m^{-1}$.
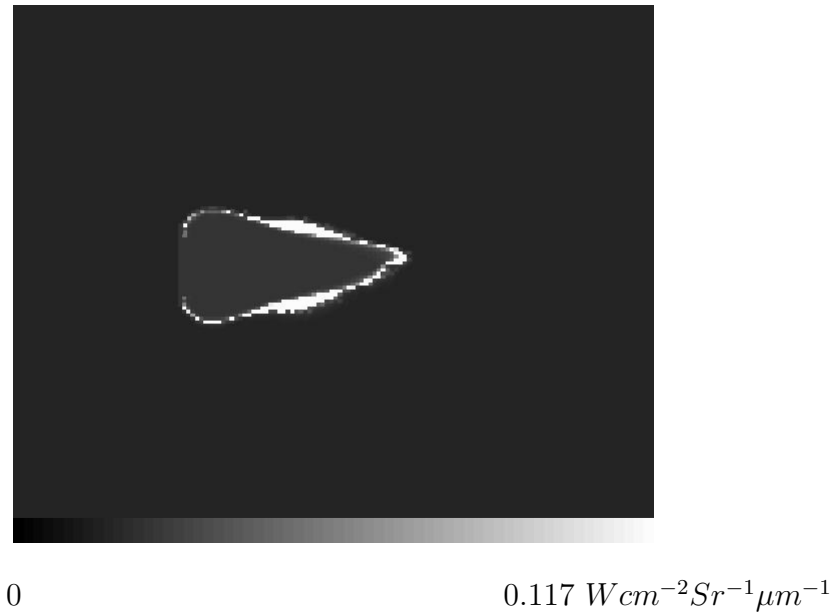
0   0.117 $Wcm^{-2}Sr^{-1}\mu m^{-1}$

Figure 6.14: DIRSIG rendering of grassfire scene with WASP sensor specification in the long-wave infrared channel, 8.0 - 11.0μm. The highest radiance is 0.117 $Wcm^{-2}Sr^{-1}\mu m^{-1}$.
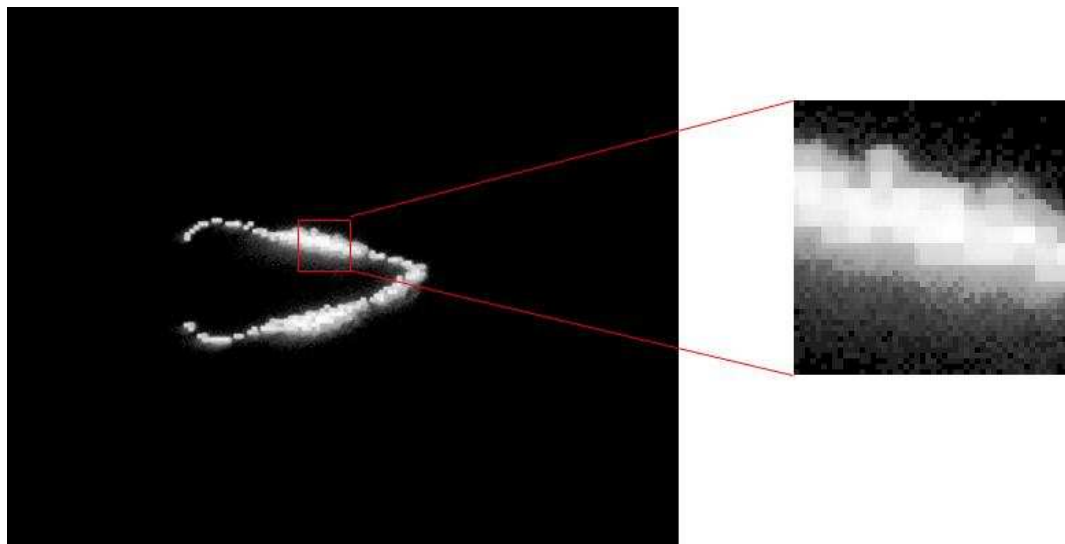
Figure 6.15: Synthetic 3D visualization of modeled fire volume with generic radiometry solver at wavelength 3μm. (a) top view of ground fire 61 min 54 sec after ignition. (b) zoomed in area.
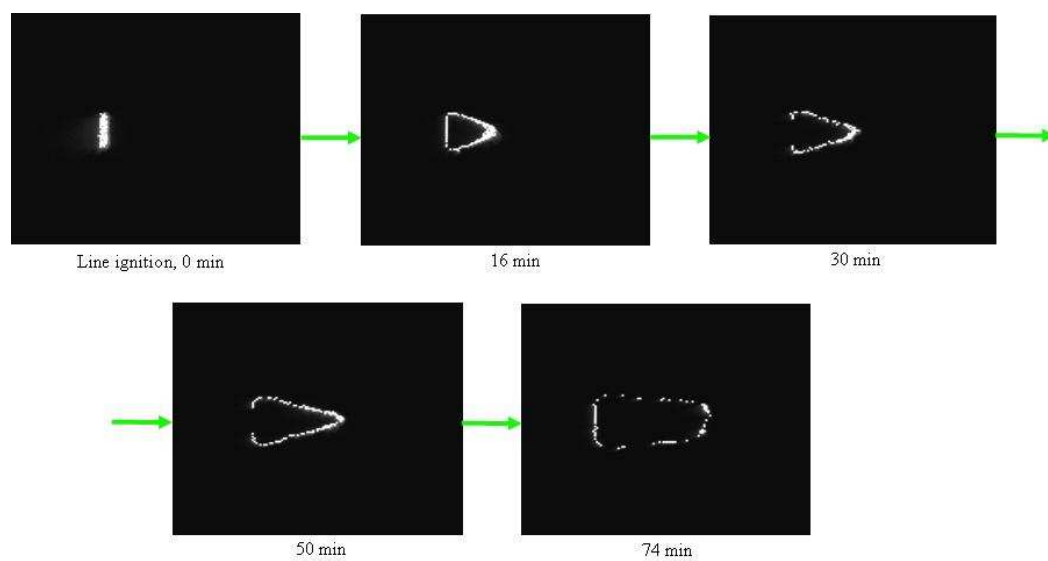
Figure 6.16: Time shot of 3D visualization of modeled fire volume with ground reflection at wavelength $3\mu m$ at times of 0, 16, 30, 50, and 74 minutes respectively.

6.6 Verification

6.6.1 Subpixel analysis on Synthetic Multispectral Imagery

After the multispectral or hyperspectral images are generated, we should be able to evaluate the abundance of various material (called end members) types present within each individual pixel. This prompts the need for subpixel analysis of a scene. According to linear spectral unmixing, each image pixel is described as a linear combination of a set of known spectra. The library is the collection of mean spectral digital count values of all the pure materials in the scene. The end product is a set of material maps (fractional area) where the value of each pixel stands for the fraction of an end member. The sum of all values within material maps should not exceed 1.0.

An approach to linear unmixing is stepwise regression. Stepwise regression is an iterative approach where a subset of end members is used to significantly reduce unmixed image error. In stepwise algorithm, each pixel in the scene is supposed to contain all the end members at first and will call for the whole spectral library. Then the fraction is calculated for each of the end members. A ratio, which stands for performance of spectral combination, is calculate and compared to a tabulated F-statistic with appropriate degrees of freedom at the desired confidence level. If the ratio is greater than the tabulated value, then added end member is required. If the ratio is smaller, then the current library is kept. The stepwise algorithm regressively adds or removes content of spectral library for each pixel until the final subset contains the optimum combination of end members. This algorithm allows subset selection that gives better unmixing

without the spectral influence from un-participated end members. The process requires both a forward regression to add classes and a backward regression to examine already accepted classes for removal. More detail of this algorithm can be found in Appendix F. Fig. 6.17 shows the process of generating spectral library, finding the best subset of end-member, and creating material maps in this research.
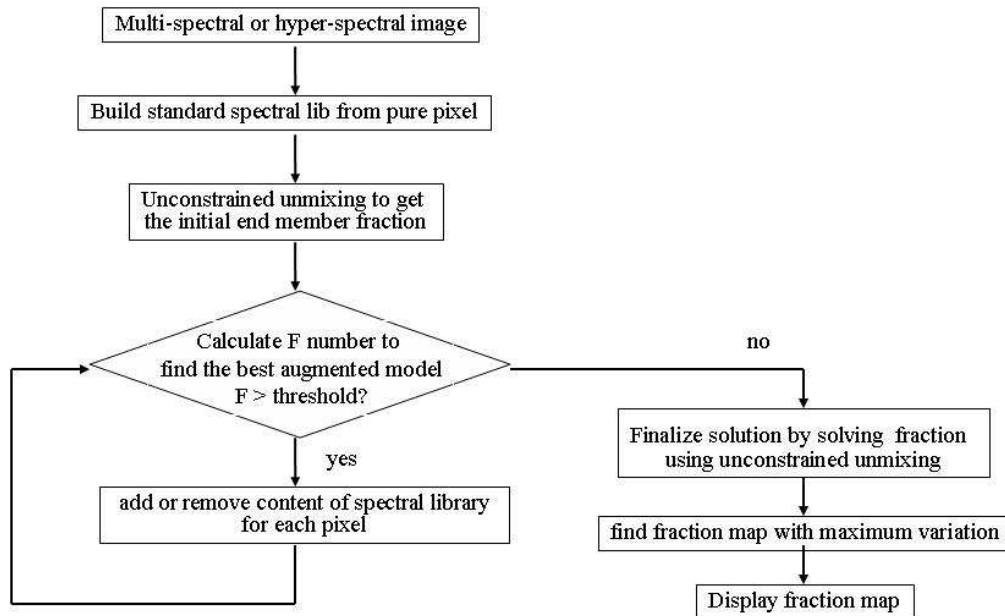
Figure 6.17: Flowchart of implementation of stepwise algorithm.

Fig. 6.18 is a synthetic scene of wildfire at wavelength 3 μm 63 minutes 36 seconds after ignition. There are hot ground, flame, smoke, burn scar, and background, a total of five type of end members in the scene. Fig. 6.19 shows the material maps of the end members and their spectra from the synthetic scene in Fig. 6.18. The fractional area of each end member can vary from 0 to 1.0. The brighter the pixel, the greater degree the pixel is filled by corresponding end

member. The most bright pixels in the material map indicate the domination of that end member.
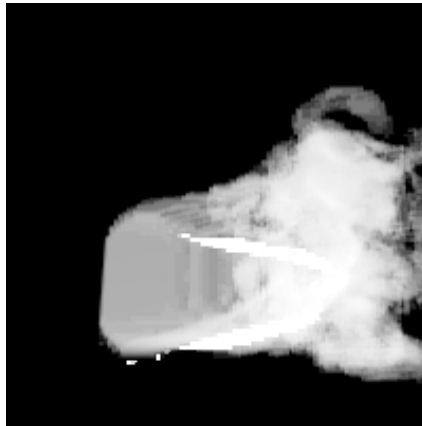
Figure 6.18: Synthetic scene of grass fire with buoyancy plume at $3\mu m$.

6.6.2 FRE Verification

The synthetic multi-spectral remote sensing wildfire scene can be verified on a pixel-by-pixel basis. Fire radiative energy (FRE) is used to determine the emitted radiant energy released during biomass combustion. It 'has been suggested as a new tool for determining variations in biomass combustion rates' (Wooster *et al.*, 2003). The calculation of FRE of a hotspot pixel is based on temperature and retrieved spatial extent of the active flaming and cooling component within the area. The active fire pixels in synthetic remote sensing image are less likely to be homogeneous and can be mixture of several thermal components each having a different temperature and fractional area. In our simulation the ground area of a single grid unit is $20*20m^2$. With this scale hotspot pixels might be composed of fire, flame, burn scar, and background. All the end members are assumed to

have a single temperature within each pixel.

(i) *Calculation of FRE true value*

The total FRE from all fire thermal components can be calculated as:

$$FRE_{TRUE} = A_{sample}\varepsilon\sigma\sum_{i=1}^{n} A_i T_i^4 \qquad (6.3)$$

where FRE_{TRUE} is fire radiative energy, J/s; A_{sample} is ground sampling area, m^2; ε is emissivity; σ is Stefan-Boltzmann constant, $5.67*10^8 J/(sm^2K^4)$; A_i is the fractional area of ith thermal component (ground truth) within a specific ground pixel; T_i is the temperature of ith thermal component, K.

Fire temperature is set to be $1100K$, which is the highest temperature observed by (Kremens and Faulring, 2003); mean flame temperature is $1000K$ and the cooling scar is $600K$ (Wooster *et al.*, 2003). The emissivity of fire front, optically thick flames, and cooling ground are close to 1. They are set to 0.90 according to Kremens and Faulring (2003) measurements.

Stepwise linear unmixing algorithm was performed on each pixel of the synthetic hyperspectral wildfire scene to calculate the fractional area A_i of each thermal component. Fig. 6.20 is the synthetic image of the wildfire at $2.0\mu m$. Fig. 6.21 shows the material maps of the thermal components in Fig. 6.20. The brighter the pixel, the higher the fractional area is of the corresponding component. The fractional area of each component varies from 0 to 1.0. The ground sampling area A_{sample} is set to be 1 m^2, the fractional area A_n of fire and other thermal components are calculated within this $1m^2$. Then FRE$_{TRUE}$ was calculated for pixels with active fire. If we leave out the sample area from equation 6.3 the units for FRE$_{TRUE}$ are $Js^{-1}m^{-2}$. The total FRE$_{TRUE}$ was determined per

unit area by summing the contribution from all thermal components for the subset of pixels that had a flaming fraction. The FRE$_{TRUE}$ per unit area for these pixels ranges from $7.309 * 10^4 Js^{-1}m^{-2}$ to $7.472 * 10^4 Js^{-1}m^{-2}$. These are total values above the background and potentially include contributions from each of the components based on the unmixing fractions. These values are slightly higher than the FRE$_{TRUE}$ per unit area for the flaming fraction in Table 2 of Wooster *et al.* (2003). This is reasonably close agreement with the results of Wooster *et al.* (2003) given that the parameters of our unmixing model were different because we included the separation of the ground temperature and the 3D flame temperature, and the ground temperature (based on field measurements) was higher than the flaming temperature in their work.

(ii) *FRE calculation via MIR radiance*

Wooster *et al.* (2003) propose a method which relates FRE to the midwave infrared radiance of the hot pixel. The Stefan-Boltzmann law states that the total energy radiated per unit surface area of a blackbody in unit time is directly proportional to the fourth power of the blackbody's thermodynamic temperature T. Rewriting the law in the form of radiance is:

$$L(\lambda) = aT^4 \tag{6.4}$$

Within the appropriate temperature range, the T^4 relationship is used to represent a 'hotspot' pixel containing n subpixel thermal components:

$$L_{MIR,h} = a\varepsilon_{MIR} \sum_{i=1}^{n} A_i T_i^4 \tag{6.5}$$

where $L_{MIR,h}$ and ε_{MIR} are the hot 'fire' pixel spectral radiance and surface

emissivity in the appropriate MIR band; a is a constant empirically determined from best-fit relationship between blackbody temperature and emitted spectral radiance (indicated in Eq. 6.4) at a single wavelength for satellite-based imaging systems. In this research $a = 3.3 * 10^{-9}$ is used which is appropriate to the Bispectral Infrared Detector (BIRD) Hotspot Recognition System (HSRS) (Wooster *et al.*, 2003). Combining Eq. 6.3 and Eq. 6.5 relates FRE to the MIR spectral radiance of the hot pixel:

$$FRE_{MIR} = \frac{A_{sample}\varepsilon\sigma}{a\varepsilon_{MIR}}L_{MIR,h} \qquad (6.6)$$

The total FRE_{MIR} per unit area for pixels with a flaming component ranged from $6.02 * 10^4 Js^{-1}m^{-2}$ to $7.89 * 10^4 Js^{-1}m^{-2}$, bounding the value of $6.36 * 10^4 Js^{-1}m^{-2}$ for the flaming component alone in Table 2 of Wooster *et al.* (2003). This is good evidence that our synthetic scene is a valid representation of fire infrared radiance.

	FRE per unit area of component $(Js^{-1}m^{-2})$	
	True value	MIR radiance method
Total FRE	$7.31 * 10^4 \sim 7.47 * 10^4$	$6.02 * 10^4 \sim 7.89 * 10^4$
Wooster *et al.* (2003): flaming	$5.97 * 10^4$	$6.36 * 10^4$

Table 6.1: FRE per unit area of flaming fire
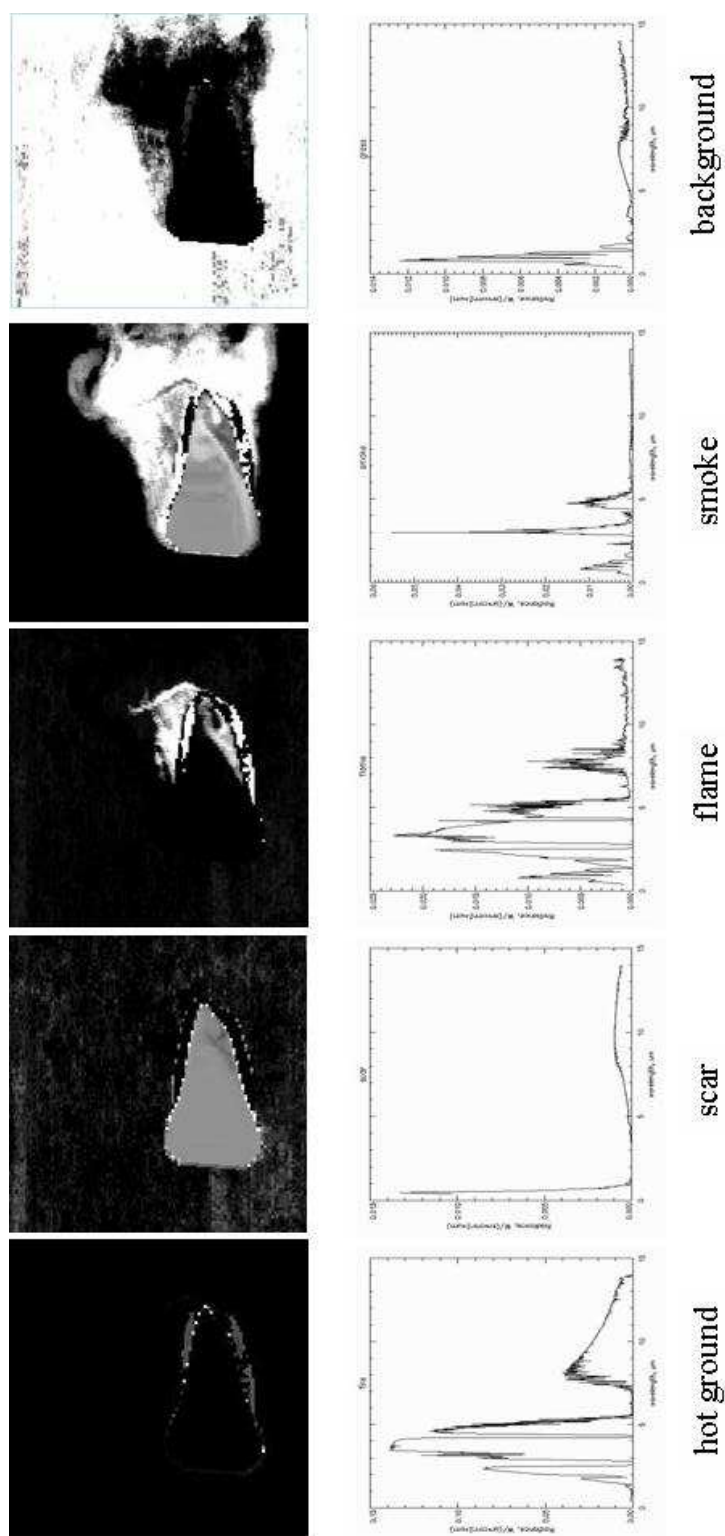
Figure 6.19: End member spectra and their material maps.
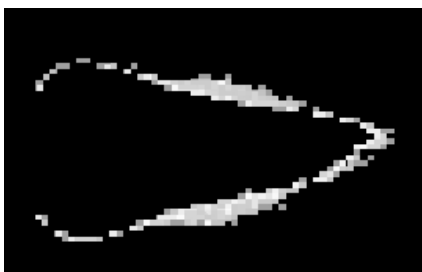
Figure 6.20: Syntheic scene of wildfire at wavelength 2.0 μm.
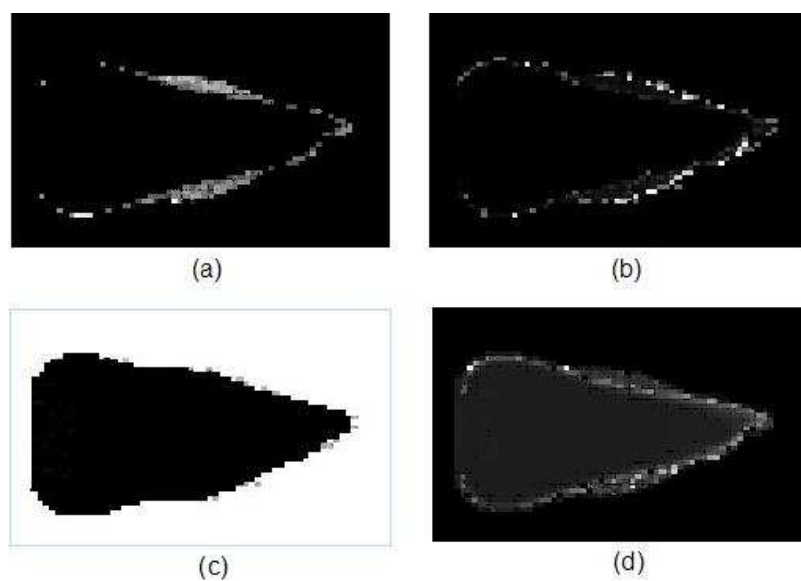
Figure 6.21: Material maps of the thermal components of the synthetic wildfire in Fig. 6.20. (a) hot ground under the fire; (b) flame; (c) unburned healthy grass; (d) burn scar.

Chapter 7

Conclusions and Future Work

The method in this research for creating synthetic infrared remote sensing scenes of wildland fire uses information from a 2D fire propagation model and knowledge of fire physical properties to estimate 3D flame spectral radiance. A grassland fire scene is rendered using a physics-based ray tracing model, DIRSIG, that accounts for radiation from the ground surface, radiation from the 3D flame, any reflected radiation from the ground nearby the fire, and atmospheric transmission. The visualization of the scene can be made for a variety of spectral responses and spatial resolutions of different sensors. Values of Fire Radiated Energy (FRE) calculated from the synthetic scene mid wave infrared radiance provide confirmation that the radiance produced by the method is valid. Given the output of a fire propagation model, the generation of the synthetic scene takes less than three minutes of computation time on a Sun Blade 1500 workstation.

The use of a physics-based image generation model like DIRSIG provides a means for very accurate rendering of the scene, both spectrally and spatially. A general assumption of the approach is that the fire radiation is a blackbody

or gray body. Improved measurements of fire spectral radiation could be used to modify these assumptions and improve the spectral rendering. However, for many operational scenarios for airborne remote sensing image data input to a data-driven fire propagation model, the use of a complicated rendering model like DIRSIG may not be necessary. Future work will examine the potential to simplify the procedures described here. For example, fire propagation codes that consider simpler 3D flame structures than our voxelized structure within their radiation transfer calculations could be used to estimate the direct and reflected radiation. Further, pre-computed atmospheric transmission properties in a look up table could be used to estimate atmospheric effects on the radiation reaching the sensor. These changes would allow a tighter coupling between the dynamic fire propagation model and the remote sensing image data and reduce computational requirements.

Appendix A

Line intensity calculation for potassium emission

Combined Saha-Boltzmann equation is used to calculate expected line intensities for Potassium emission. Boltzmann excitation equation tells the ion fraction in the lower level involved in the spectral line. Saha equation gives the ionization fraction of dominating ionic species in potassium. Multiplication of Saha factor and Boltzmann factor gives the number of potassium atoms capable of emitting the strong line emissions. According to Saha equation, degree of ionization is a function of the temperature, density, and ionization energies of the atoms. If n_{i+1} is the density of atoms in the ionization state $i + 1$ and n_i, the atom density in the ionization state i, then the Saha equation is written as

$$R_j = \frac{n_{i+1}}{n_i} = \frac{2Z_2}{n_e Z_1}(2\pi m_e k \frac{T_j}{h^2})^{3/2} e^{\frac{-E_i}{kT_j}} \tag{A.1}$$

where Z_1 and Z_2 are partition functions of ionized and neutral potassium respectively; n_e is the number density of free electrons within the flame; m_e is the

electron mass, $9.109 * 10^{-31}(Kg)$; k is Boltzmann's constant, $1.38 * 10^{-23}(J/K)$; T_j is the fire temperature in kelvin; h is the Planck constant, $6.63 * 10^{-34}(J/s)$; E_i is Potassium ionization energy, $6.92064 * 10^{-19}(J)$. Then fraction of ionized Potassium to total number of potassium atom is:

$$f_j = \frac{R_j}{R_j + 1} \tag{A.2}$$

Using dimensional analysis, the power in potassium line is given by

$$P_{o_j} = Na * a * K1 * E1 * f_j * V \tag{A.3}$$

where Na is the number density in the fire volume; a is the decay rate of Potassium from excited state to ground state, specified in 1/sec; K1 is the number of ionized atoms that transit from excited to ground state (from singly ionized Potassium to neutral Potassium); E1 is the energy of 1st excited state, in unit of J; f_j is the fraction of ionized Potassium to total potassium atoms from Eq A.2; V is interrogated volume. The power associated with the second emission peak is about 60% of the first peak. Hence, the total power P_{k_j} is

$$P_{k_j} = P_{o_j} + 0.6P_{o_j} = P_{o_j} * 1.6 \tag{A.4}$$

P_{k_j} is the power in potassium line into 4π steradians from the interrogated volume. So Potassium emission intensity as a function of temperature is obtained and illustrated in Fig A.1.

The curve indicates that potassium power increases dramatically as temperature is over 900K, almost reaches the peak power at 1100k, and keeps unchanged
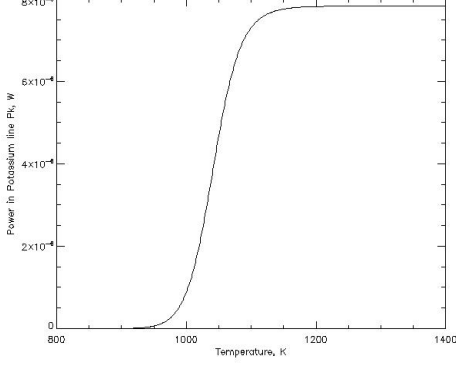
Figure A.1: Power in potassium line as function of temperature.

when temperature is higher than 1200K. Ratio of potassium power to blackbody power is estimated to further analyze potassium line emission. The radiance emitted by flame of emissivity ϵ at temperature T_j follows Planck's radiation law

$$BB_{i,j} = \frac{2\pi hc^2\epsilon}{\lambda_i^5(e^{\frac{hc}{\lambda_i k T_j}} - 1)} * 10^{-9} \tag{A.5}$$

The total power radiated over energy window of Potassium emission observation is

$$S_j = \left(\sum_i BB_{i,j}\right) * 10^{-9} \tag{A.6}$$

Hence, the sensor reaching potassium power is

$$P_{b_j} = S_j * A_i \tag{A.7}$$

where A_i is the sensor optics surface area on the front face. Potassium has two strong emission lines at spectrum 766.490nm and 769.896nm. Integrate both the potassium and blackbody spectral power P_{k_j} and P_{b_j} within energy windows

766.40nm $\sim$ 766.60nm and 769.80nm $\sim$ 770.00nm, take the ratio of sums

$$R_j = \frac{P_{k_j}}{P_{b_j}} \tag{A.8}$$
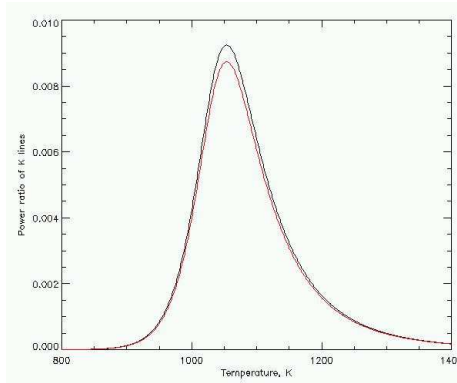
Figure A.2: Ratio of potassium power to blackbody power as function of temperature.

R_j is the power ratio of potassium to blackbody as function of temperature, as shown in Fig A.2. The black and red curves are power ratio for potassium emission lines 766.490nm and 769.896nm, respectively. The plot indicates that the excitation of potassium takes place when the temperature is higher than 800K. The peak of relative power happens at temperature around 1050K, which is very close to the measured highest wildfire temperature of 1100K. Flowchart in Fig A.3 describes the steps calculating potassium line intensities.

Since big fires perform as blackbody, potassium emission lines are added to blackbody spectral radiation based on the power ratio calculated above to simulate fire radiometry. Fig A.4 shows blackbody radiation with potassium emission lines at temperature of 1100K. The calculated fire temperatures with high potassium/blackbody power ratio are much lower than that estimated from observed
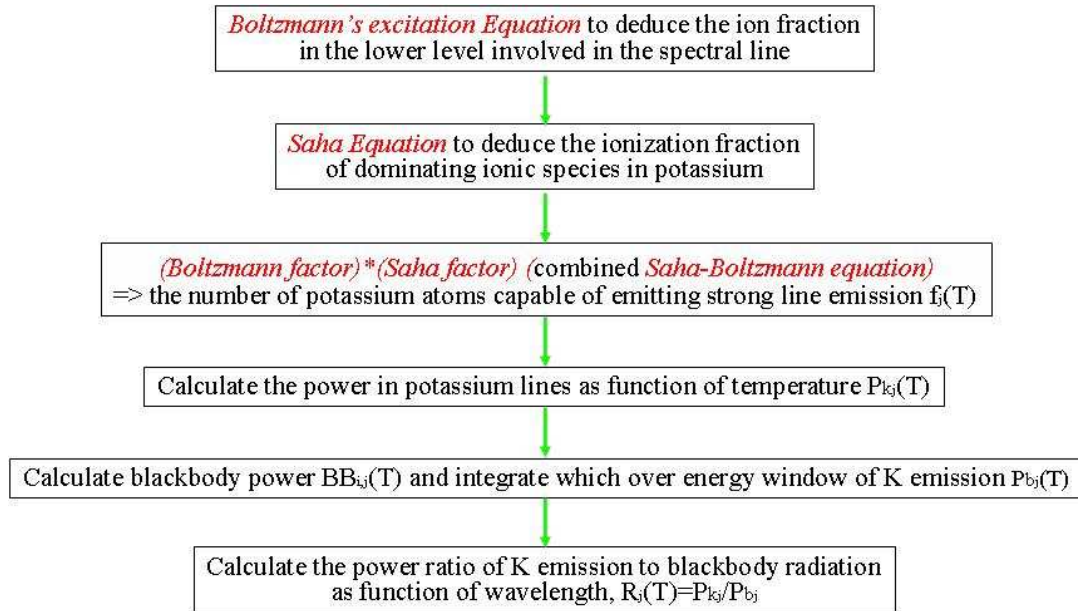
Figure A.3: Calculate potassium line emission intensities.

ASD data, see Fig. 6.1 (a). With the calculations proposed in this method, we won't be able to observe K emissions when fire is hotter than 1200K because potassium power takes less than 2% of the blackbody radiative power, which doesn't agree with the experiment result. The estimated potassium emission intensity is also lower than that from AVIRIS measurement, see Fig. 3.1. The method proposed here needs to be improved to make precise reproduction of K emission intensity.
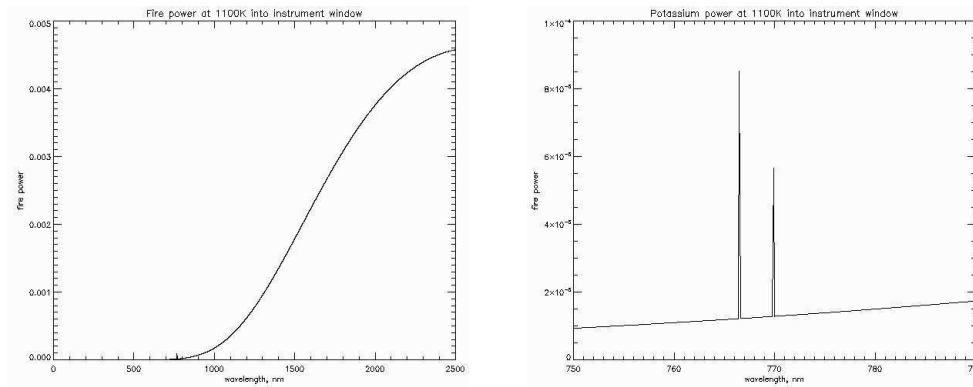
Figure A.4: Left: blackbody radiation with potassium emission lines at 1100K. Right: zoom in potassium lines.

Appendix B

CONDOR submit file

```
# Submit DIRSIG jobs to condor


# we want to run dirsig-condor
Executable = /dirs/pkg/dirsig/bin/dirsig-3.6.1-condor


# we will use standard universe since it supports preemption
Universe = standard


# we want a Solaris 5.9 machine with at least 100 MB of memory
Requirements = Arch == "SUN4u" && (OpSys == "SOLARIS29")


# we want to be notified if things go bad
Notification = error


# make a file to log all the condor activity for the jobs
```

```
Log = fire.log


# queue frame #1_16

FrameName = 1_16

Output = out/$(FrameName).output

Error = err/$(FrameName).error

Arguments = cfg/$(FrameName).cfg

Environment = DIRSIG_HOME=/dirs/lib/dirsig

Queue


# queue frame #2_16

FrameName = 2_16

Output = out/$(FrameName).output

Error = err/$(FrameName).error

Arguments = cfg/$(FrameName).cfg

Environment = DIRSIG_HOME=/dirs/lib/dirsig

Queue


...
```

Appendix C

File Formats for Voxelized Geometry

Voxelized geometry in DIRSIG allows users to implement volume visualization. The volume is divided into a series of regularly spaced boxes. A unique material, temperature, and concentration is assigned to each box. The voxelized grid implementation treats each voxel along the path as a piece of volume geometry. The radiometry contribution from each intersected voxel is solved independently and then folded into the path solution. The grid itself is specified in two different files: the grid file and the ODB file. The grid file specifies the voxel data without any physical dimensions. The entry in the ODB indicates the physical dimensions and location of the grid.

C.1 CFG: Configuration

```
DIRSIG_CFG
```

```
PATHS {

    GDB_PATH =          ./gdb

    ODB_PATH =          ./odb/google_grid_WASP

    EMISSIVITY_PATH = ./emissivity

    EXTINCTION_PATH = ./extinction

    ABSORPTION_PATH = ./absorption

    MATERIAL_PATH =    ./materials

    WEATHER_PATH =     /dirs/common/dirsig/data/weather

    TAPE5_PATH =       ./tape5

    MAPS_PATH =        ./maps

    SOURCES_PATH =     ./source

    RESPONSE_PATH =    ./responses

    PROFILE_PATH =     ./profile

}


SCENE {

    ODB_FILENAME = 666.odb

    GDB_UNITS = METERS

    MATERIAL_FILENAME = fire.mat

    GROUND_ALTITUDE = 0.300

    DATE = 8 1 2000

    GMT_OFFSET = 4.000

    LOCAL_TIME = 22.000

    LATITUDE = 43.000
```

```
    LONGITUDE = 88.000
}


ENVIRONMENT {
    TAPE5_FILENAME = mls.tp5
    ADB_FILENAME = WASP_top_MWIR.adb
    WEATHER_FILENAME = mls.wth
}


PLATFORM {
    NAME =
    INSTRUMENT {
        NAME = pan
        TYPE = FRAMING_ARRAY
        FOCAL_LENGTH = 25.00
        BAND_LIST {
            BAND {
                X_PIXELS = 640
                Y_PIXELS = 512
                MINIMUM_WAVELENGTH = 3.000
                MAXIMUM_WAVELENGTH = 5.000
                DELTA_WAVELENGTH =   1.000
                RESPONSE_FILENAME = SPECTRAL
                IMAGE_FILENAME = grid.img
            }
```

```
        }
    }
    POSITION {
        TARGET_LOCATION =   2000.0000, 2000.0000, 0.0000
        PLATFORM_LOCATION = 2000.0000, 2000.0000, 3000.0000
    }
}


OPTIONS {
    ENABLE_TRUTH_IMAGES =           FALSE
    ENABLE_THERMAL_MODEL =          TRUE
    ENABLE_MAPS =                   TRUE
    ENABLE_SOURCES =                TRUE
}


TRUTH_IMAGES {
    IMAGE_FILENAME =            truth.img
    MATERIAL_MAPS =             TRUE
    TEMPERATURE_MAPS =          TRUE
}


#  0  = 8000  grass/brown and green/dirt
# 210 = 9     Scar
# 255 = 211   blackbody1100K
MAPS {
```

```
MATERIAL_MAP {

    IMAGE_FILENAME = coupled_mat_WASP/666.pgm

    MATERIAL_ID = 100

    INSERT_POINT = 0.0, 0.0, 0.0

    GSD = 20.0000

    LUT {

        0   = 8000

        255 = 211

        210 = 9

    }

}

TEMPERATURE_MAP {

    IMAGE_FILENAME = coupled_temp_WASP/666.img

    MATERIAL_ID = 8000, 211, 9

    INSERT_POINT = 0.0, 0.0, 0.0

    GSD = 20.0000

}

TEXTURE_MAP {

    IMAGE_FILENAME = grass_texture.pgm

    MATERIAL_ID = 8000, 9

    MINIMUM_WAVELENGTH = 0.400

    MAXIMUM_WAVELENGTH = 0.700

    GSD = 0.8

}

}
```

C.2   ODB: Object Database

The insert point indicates the scene coordinates (in meters) at which to place the grid. The parameters DELTA_X, DELTA_Y, and DELTA_Z associate a physical size to the voxels. The GRID_FILENAME indicates where the dimensionless grid data is stored.

```
DIRSIG_ODB = 1.0


OBJECT {
    GDB_FILENAME = plate.gdb
    UNITS = METERS
    INSTANCES {
        INFO = 0, 0, 0, 1, 1, 1, 0, 0, 0
    }
}


REGULAR_GRID {
    INSERT_POINT = 600.0, 600.0, 0.0
    DELTA_X = 20.0
    DELTA_Y = 20.0
    DELTA_Z = 5.0
    GRID_FILENAME = 666.grid
}
```

C.3 GRID: Regular Grid

The three integers in the first line denote the dimensions of the grid. The remainder of the file consists of lines with six columns of data. The first three columns indicate the voxel index (counting from 0). The fourth column indicates a DIRSIG material ID corresponding to an entry in the Material Database File (.mat). The fifth column indicates temperature in kelvin. The final column indicates concentration in [ppm]. Unspecified voxels are treated as being empty. They do not take up memory though they do slow the ray tracing process to some degree.

```
142    142    64
 43     57     0    206    795.444   1000.2030
 44     57     0    206    795.228   1000.2030
 41     58     0    206    795.228   1000.2030
 42     58     0    206    796.091   1000.2030
 52     60     0    206    795.875   1000.2030
 ...
```

Appendix D

File Formats for Secondary Point Source

D.1   CFG: Configuration

The configuration file for secondary point source rendering is the same as that in C.1.

D.2   ODB: Object Database

```
DIRSIG_ODB = 1.0

OBJECT {
    GDB_FILENAME = plate.gdb
    UNITS = METERS
    INSTANCES {
```

```
        INFO = 0, 0, 0, 1, 1, 1, 0, 0, 0

    }

}


OBJECT {

    GDB_FILENAME = ptsource.gdb

    UNITS = METERS

    INSTANCES {

        INFO = 1380, 1640, 1.00000, 1, 1, 1, 0, 0, 0

        INFO = 1400, 1640, 1.00000, 1, 1, 1, 0, 0, 0

        INFO = 1420, 1640, 1.00000, 1, 1, 1, 0, 0, 0

        ...

    }

}
```

D.3   GDB: Geometry Database

```
OBJECT

PT_SOURCE_OBJECT

1-0-0

PART

PT_SOURCE_PART

1-1-0

FACE

PT_SOURCE_1

1-1-1
```

```
point sources

777

NONE

0.00

1.0000

0.0000

0.0

null

null

null

1

0.0 0.0 0.0

0.000000000000000e+00  0.000000000000000e+00  -1.000000000000000e+00

0.0000000000

0.0000000000

0.0000000000

END
```

Appendix E

File Format for Generic Radiometry Solver

```
MATERIAL_ENTRY {

    NAME = Terrain

    ID = 100

    EDITOR_COLOR = 0.6941, 0.6471, 0.3765


    TEMP_SOLVER_NAME = Therm

    TEMP_SOLVER {

        SPECIFIC_HEAT = 0.0000

        THERMAL_CONDUCTIVITY = 0.0000

        MASS_DENSITY = 0.5

        SOLAR_ABSORPTION = 0.2500

        THERMAL_EMISSIVITY = 0.9000

        EXPOSED_AREA = 0.4500
```

```
        THICKNESS = 0.1
    }


    SURFACE_PROPERTIES {
        EMISSIVITY_PROP_NAME = ClassicEmissivity
        EMISSIVITY_PROP {
            FILENAME = field1_brngrass_grass_mix300.ems
            SPECULAR_FRACTION = 0.0
        }
    }


    RAD_SOLVER_NAME = Generic
    RAD_SOLVER {
        INITIAL_SAMPLE_COUNT = 64
        MAX_BOUNCES = 3
        SAMPLE_DECAY_RATE = 4
    }
}
```

Appendix F

Subpixel Unmixing and Stepwise Regression

The widely applied linear mixing model assumes that if a pixel is not pure, then the observed spectral vector is a linear combination of the spectral vectors that would be observed from pure samples of the end members present in the pixel(Smith *et al.*, 1990a,b). If there are k end members and l bands of the observed image, then observed energy (reflectance, radiance, digital count, or any linear-transformed space) of a pixel in l bands can be written in l equivalent expressions (i.e., one for each band)

$$
\begin{aligned}
x_1 &= v_{11}f_1 + v_{12}f_2... + v_{1k}f_k + \epsilon_1 \\
x_2 &= v_{21}f_1 + v_{22}f_2... + v_{2k}f_k + \epsilon_2 \\
&... \\
x_l &= v_{l1}f_1 + v_{l2}f_2... + v_{lk}f_k + \epsilon_l
\end{aligned}
\tag{F.1}
$$

where $(\mathbf{v_1}, \mathbf{v_2}...\mathbf{v_k})$ are the spectrum of k end members, $(f_1, f_2...f_k)$ are k unknown area-weighted subpixel fractions of the pure end members contained in the pixel, see Fig. F.1. $(\epsilon_1, \epsilon_2...\epsilon_l)$ are residual error in the mixture model of each band. A nine-pixel three-material example is shown in Fig. F.1.
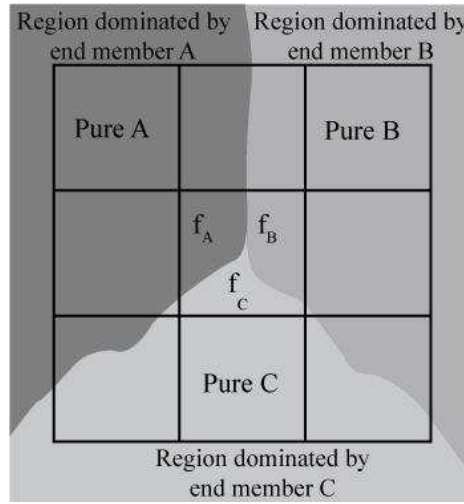

Figure F.1: Illustration of linear mixing of material component. For linear mixing in radiance, $L_M = f_A L_A + f_B L_B + f_C L_C$; for linear mixing in digital count, $DC_M = f_A DC_A + f_B DC_B + f_C DC_C$. (Image courtesy of John Schott, 2007)

Rewrite the equivalent expressions in array F.1 in form of vector:

$$\mathbf{x} = \mathbf{B}\alpha + \epsilon \qquad\qquad (\text{F.2})$$

where

$$
\mathbf{x} = \begin{bmatrix} x_1 \\ x_2 \\ \dots \\ x_l \end{bmatrix} \text{ and } \mathbf{B} = \begin{bmatrix} v_{11} & v_{12} & \dots & v_{1k} \\ v_{21} & v_{22} & \dots & v_{2k} \\ \dots & & & \\ v_{l1} & v_{l2} & \dots & v_{lk} \end{bmatrix} \text{ and } \alpha = \begin{bmatrix} f_1 \\ f_2 \\ \dots \\ f_k \end{bmatrix} \text{ and } \epsilon = \begin{bmatrix} \epsilon_1 \\ \epsilon_2 \\ \dots \\ \epsilon_l \end{bmatrix}
$$

With the observed image spectrum $\mathbf{x}$ and pure sample $\mathbf{v_1}$ through $\mathbf{v_k}$ of end members, unknown weights f_1 through f_k need to be solved to give the vector of end-member fractions (α). Since the number of band l is usually more than the number of end member k which is typically less than 10, this problem is over determined and can be solved by conventional least-squares methods. Thus, we can unmix each spectral vector into the end-member fractions contained in that pixel according to

$$
\hat{\alpha} = \mathbf{B}^\sharp \mathbf{x} = E < \mathbf{B}^\sharp \mathbf{B} \alpha + \epsilon > \simeq \mathbf{I}\alpha = \alpha \tag{F.3}
$$

where the pseudo-inverse operator $B^\sharp$ yields a best fit (in a least-squared error sense) solution for $\hat{\alpha}$; E represents the expected value operator. The residual error vector ϵ can be computed as

$$
\epsilon = \mathbf{x} - \mathbf{B}\hat{\alpha} \tag{F.4}
$$

Operationally Eq. F.3 is solved for each pixel, and k fraction images are produced whose brightness is proportional to the fractional value of each of the k end members computed for each pixel. In practice, there are two limitations we need to be concerned about. The first limitation enforces the physical constraint

that the fractional contributions of the end members sum to one, i.e.,

$$\sum_{i=1}^{k} f_i = 1 \qquad \text{(F.5)}$$

The second constrains the fractional abundances to be fractions, i.e.,

$$0 \leq f_i \leq 1 \qquad \text{(F.6)}$$

Fractions slightly outside the 0 to 1 range may be reasonable, but the values significantly outside the expected range are taken as poor fit to the model. The high error pixels are often pixels that contain materials not in the end-member model. To search for the best end member combination and overcome the limitations of the fixed model approach to unmixing, stepwise regression rises to solve the problem.

Stepwise unmixing is an approach where a subset of end-members is used to significantly reduce unmixed image error. In stepwise algorithm, each pixel in the scene is supposed to contain all the end members at first and will call for the whole spectral library. Then the fraction is calculated for each of the end members. A ratio, which stands for performance of spectral combination, is calculate and compared to a tabulated F-statistic with appropriate degrees of freedom at the desired confidence level. If the ratio is greater than the tabulated value, then added end member is required. If the ratio is smaller, then the current library is kept. The stepwise algorithm regressively adds or removes content of spectral library for each pixel until the final subset contains the optimum combination of end members. At this point, any conventional linear unmixing algorithms (unconstrained, partially constrained, or fully constrained) can be

employed to unmix the pixel with known end members included. This algorithm allows subset selection that gives better unmixing without the spectral influence from unparticipated end members.

The metric used to control the stepwise process uses the errors associated with the regression which can be expressed as

$$\sigma_{tot} = \mathbf{x^T x} = SSR + SSE = \hat{\alpha}^{\mathbf{T}} \mathbf{B^T x} + [\mathbf{x^T x} - \hat{\alpha}^{\mathbf{T}} \mathbf{B^T x}] \tag{F.7}$$

where σ_{tot} is the total variation in the pixel (about the origin); SSR is the sum squared variation explained by the regression; SSE is the sum squared error. A mixing model is sought to explain as much of the variation as possible (maximize SSR) without over fitting to the measurement noise. The solution is based on an analysis of variance, which assumes that if the model is good, the errors will be Gaussian with zero mean, the SSR and SSE are chi squared distributed, and their mean square ratio is $F_{k,l-k}$ distributed (i.e., k degrees of freedom in numerator, $l - k$ degrees of freedom in the denominator) according to:

$$F_{k,l-k} = \frac{MSR}{MSE} = \left(\frac{SSR}{k} \right) \Big/ \left(\frac{SSE}{l-k} \right) \tag{F.8}$$

where MSR is the mean square variation explained by the regression and MSE is the mean square error (residual error). When we are comparing the difference between two models, i.e., one of which has k end members and the other has $k-1$ end members, the decision rule used to compare the augmented (k) model to the $k - 1$ model uses the mean square value for the extra term expressed as

$$MS_{extra} = \frac{\hat{\alpha}_{\mathbf{k}}^{\mathbf{T}} \mathbf{B_k^T x} - \hat{\alpha}_{\mathbf{k-1}}^{\mathbf{T}} \mathbf{B_{k-1}^T x}}{k - (k-1)} \tag{F.9}$$

This represents the difference in the amount of variation explained by the model with k terms and $k-1$ terms. The ratio of MS_{extra} to MSE is F-distributed with [k-(k-1)=1] degree of freedom in the numerator and $l-k$ in the denominator. We can test if the model improvement is significant by checking if

$$F_{1,l-k} = \frac{MS_{extra}}{MSE} = \frac{\hat{\alpha}_{\mathbf{k}}^{\mathbf{T}}\mathbf{B}_{\mathbf{k}}^{\mathbf{T}}\mathbf{x} - \hat{\alpha}_{\mathbf{k-1}}^{\mathbf{T}}\mathbf{B}_{\mathbf{k-1}}^{\mathbf{T}}\mathbf{x}}{k-(k-1)} * \frac{l-k}{\mathbf{x}^{\mathbf{T}}\mathbf{x} - \hat{\alpha}^{\mathbf{T}}\mathbf{B}^{\mathbf{T}}\mathbf{x}} \qquad (F.10)$$

exceeds the tabulated value for the corresponding F-test. 'If the improvement is significant, the new end member should be included. If, during the backward stepwise test, the smallest F value is below the threshold, then that end member is removed from the model since its inclusion no longer significantly increases the amount of variation explained by the model' (Schott, 2007).

Bibliography

Andrews, P. L. (1986). BEHAVE: Fire behavior prediction and fuel modeling system-BURN subsystem, part 1. Technical report, USDA Forest Service.

Asensio, M. I. and Ferragut, L. (2002). On a wildland fire model with radiation. *International journal for numerical methods in engineering*, **54**, 137–157.

Bailey, A. W. and Anderson, M. L. (1980). Fire temperatures in grass, shrub and aspen forest communities of central alberta. *Journal of Range Management*, **33**, 37–40.

Barnard, J. and Bradley, J. (1985). *Flame and Combustion*. Chapman and Hall, 2nd edition.

Bertschi, I., Yokelson, R. J., Ward, D. E., Babbitt, R. E., Susott, R. A., Goode, J. G., and Hao, W. M. (2003). Trace gas and particle emissions from fires in large diameter and belowground biomass fuels. *J. Geophysical Research*, **108**(D13).

Borovik, A. A., Rojas, H. L., King, G. C., and Remeta, E. Y. (1999). Electron-impact excitation of potassium autoionizing levels in the near-threshold region. *J. Phys. B: At. Mol. Opt. Phys.*, **32**, 4225–4235.

Bowen, H. J. M. (1979). *Environmental Chemistry of the Elements*. London: Academic Press.

Brenner, J., Green, K., Coen, J., and McLellan, S. (2005). Assessing fire risk in florida using integrated GIS and remote sensing applications.

Brown, A. A. and Davis, K. P. (1973). *Forest fire control and use*. McGraw-Hill, New York, 2nd edition.

Brown, S. (2003). DIRSIG user documentation. Technical report, Rochester Institute of Technology.

Brown, S. and Schott, J. (2000). Characterization techniques for incorporating backgrounds into DIRSIG. In *SPIE AeroSense Conference*.

Byram, G. M. (1959). Forest fire behavior. In K. P. Davis, editor, *Forest Fire: Control and Use*, pages 90–123. McGraw-Hill, New York.

Cahoon, D. R., Stocks, B. J., Levine, J. S., III, W. R. C., and Chung, C. C. (1992). Evaluation of a technique for satellite-derived area estimation of forest fires. *J. Geophysical Research*, **97**(D4), 3805–3814.

Chiba, N., Muraoka, K., Takahashi, H., and Miura, M. (1994). Two-dimensional visual simulation of flames, smoke and the spread of fire. *J. of Visualization and Computer Animation*, **5**(1), 37–54.

Clark, T. L. and Hall, W. D. (1995). The design of smooth, conservative vertical grids for interactive grid nesting with stretching. *J. Appl. Meteor*, **35**, 1040–1046.

Clark, T. L., Jenkins, M. A., Coen, J., and Packham, D. (1996a). A coupled atmospheric-fire model: convective feedback on fire line dynamics. *J. Appl. Meteor*, **35**, 875–901.

Clark, T. L., Jenkins, M. A., Coen, J., and Packham, D. R. (1996b). A coupled atmospheric-fire model: role of the convective froude number and dynamic fingering at the fireline. *Intl. J. of Wildland Fire*, **6**, 177–190.

Clark, T. L., Coen, J., and Latham, D. (2004). Description of a coupled atmosphere-fire model. *Intl. J. Wildland Fire*.

Coen, J. L., Clark, T. L., and Latham, D. (2001). Coupled atmosphere-fire model simulations in various fuel types in complex terrain. In *4th Symposium on Fire and Forest Meteorology*.

Cofer, W. R., Winstead, E., Stocks, B., Goldammer, J., and Cahoon, D. (1998). Crown fire emissions of CO2, CO, H2, CH4, and TNMHC from a dense jack pine boreal forest fire. *Geophysical Research Letters*, **25**(21), 3919–3922.

Cottrell, W. H. (1989). *The Book of Fire*. Mountain Press Publishing Company.

Cunningham, P., Goodrick, S. L., Hussaini, M. Y., and Linn, R. R. (2005). Coherent vortical structure in numerical simulations of buoyant plumes from wildland fires. *Intl. J. Wildland Fire*, **14**, 61–75.

Darema, F. (2004). Dynamic data driven applications systems: A new paradigm for application simulations and measurements. In *ICCS*, pages 662–669.

Dennison, P. E. (2006). Fire detection in imaging spectrometer data using atmo-

spheric carbon dioxide absorption. *International Journal of Remote Sensing*, **27**, 3049–3055.

Digital Imaging and Remote Sensing Laboratory (2006). *The DIRSIG User Manual*. Rochester Institute of Technology.

Drysdale, D. (1999). *An Introduction to Fire Dynamics*. John Wiley and Sons.

Dupuy, J.-L. and Larini, M. (1999). Fire spread through a porous forest fuel bed: a radiative and convective model including fire-induced flow effects. *Intl. J. Wildland Fire*, **9**, 155–172.

Dupuy, J.-L., Marechal, J., and Morvan, D. (2003). Fire from a cylindrical forest fuel burner: combustion dynamics and flame properties. *Combustion and Flame*, **135**, 65–76.

Finney, M. A. (1998). FARSITE:fire area simulator–model developement and evaluation. Technical Report RMRS-RP-4, USDA Forest Service, Rocky Mountain Research Station.

Fraser, R. and Li, Z. (2002). Estimating fire-related parameters in boreal forest using SPOT VEGETATION. *Remote Sensing of Environment*, **82**, 95–110.

French, N. H. F., Kasischke, E. S., Johnson, R. D., Bourgeau-Chavez, L. L., Frick, A. L., and Ustin, S. L. (1996). Estimating fire-related carbon flux in alaskan boreal forests using multi-sensor remote sensing data. In *AGU Chapman Conference on Biomass Burning and Climate Change*.

Goody, R. E. (1995). *Principles of Atmospheric Physics and Chemistry*. Oxford University Press US.

Grabner, K. W., Dwyer, J. P., and Cutter, B. E. (2001). Fuel model selection for BEHAVE in midwestern oak savannas. *Northern Journal of Applied Forestry*, **18**(3), 74–80.

Harris, S. E. (1980). Proposal for a 207-Å laser in lithium. *OPTICS LETTERS*, **5**(1).

Hecht, E. (1998). *Optics*. Addison-Wesley, 3rd edition.

Henderson, T. C., McMurtry, P. A., Smith, P. J., Voth, G. A., Wight, C. A., and Pershing, D. W. (2000). Simulating accidental fires and explosions. *Computing in Science and Engineering*, **2**, 64 – 76.

Heskestad, G. (1995). Fire plumes. In *SFPE handbook of fire protection engineering*, pages 2:9–19. National Fire Protection Association, 2 edition.

Ientilucci, E., Brown, S., and Schott, J. (2001). Low-light-level simulations and extended area source modeling. Technical Report 00/01-68-159, RIT/DIRS.

Kaufman, Y. J., Tucker, C. J., and Fung, I. (1990). Remote sensing of biomass burning in the tropics. *Journal of Geophysical Research*, **95**(D7), 9927–9939.

Kaufman, Y. J., Remer, L. A., Ward, D. E., Kleidman, R., Flynn, L., Shelton, G., Ottmar, R. D., Li, R.-R., Fraser, R. S., and McDougal, D. (1996). *Global biomass burning*, chapter Relationship between remotely sensed fire intensity and rate of emission of smoke: SCAR-C Experiment, pages 685–696. MIT Press.

Kaufman, Y. J., Justice, C., Flynn, L., Kendall, J., Prins, E., Ward, D. E.,

Menzel, W. P., and Setzer, A. (1998). Monitoring global fires from EOS-MODIS. *Journal of Geophysical Research*, **103**, 32215–32238.

Kaufman, Y. J., ICHOKU, C., GIGLIO, L., KORONTZI, S., CHU, D. A., HAO, W. M., LI, R. R., and JUSTICE, C. O. (2003). Fire and smoke observed from the earth observing system MODIS instrument–products, validation, and operational use. *Intl. J. Remote Sensing*, **24**(8), 1765–1781.

King, M. D., Kaufman, Y. J., Menzel, W. P., and Tanré, D. (1992). Remote sensing of cloud, aerosol, and water vapor properties from the moderate resolution imaging spectrometer MODIS. *IEEE Transactions on Geoscience and Remote Sensing*, **30**, 2–27.

Kremens, B. (2001a). The physics and phenomenology of wildfire. In *University of Rochester S & T Symposium*.

Kremens, R. (2001b). Advanced concepts in fire detection. local.

Kremens, R. L. and Faulring, J. (2003). Measurement of the time-temperature and emissivity history of the burn scar for remote sensing applications. In *2nd Annual Fire Ecology Congress*.

Kuhlbusch, T. A. J. and Cruzen, P. J. (1996). Black carbon, the global carbon cycle, and atmospheric carbon dioxide. *Biomass Burning and Global Change*, **1**, 160–169.

Lamorlette, A. and Foster, N. (2002). Structural modeling of flames for a production environment. In *Proceedings of SIGGRAPH 02, Computer Graphics Proceedings*, pages 729–735.

Lee, H., Kim, L., Meyer, M., and Desbrun, M. (2001). Meshes on fire. In *Computer Animation and Simulation 2001, Proc. of the Eurographics Workshop in Manchester, UK*, pages 75–84.

Levine, J. S., Cofer, W. R., Cahoon, D. R., and Winstead, E. L. (1995). Biomass burning: A driver for global change. *Environmental Science and Technology*, **29**, 120–125.

Li, Z. and Cihlar, J. (1999). Remote sensing of Canadian boreal forest fires: hotspots, burned area, and smoke plumes. In *IEEE International Geoscience and Remote Sensing Symposium*.

Li, Z., Jin, J., and Fraser, R. (2000). Mapping burned areas and estimating fire emissions over the Canadian boreal forest. In *Proceedings of the Joint Fire Science Conference and Workshop*, pages 247–251, Idaho, USA.

Lin, C. C. (1996). http://raptor.physics.wisc.edu/talk/part_3a.htm.

Linn, R., Reisner, J., Colman, J. J., and Winterkamp, J. (2002). Studying wildfire behavior using FIRETEC. *International Journal of Wildland Fire*, **11**, 233–246.

Linn, R. R. (1997). A transport model for prediction of wildlife behavior. Technical Report LA-13334-T, Los Alamos National Laboratory.

Longo, K. M. and Freitas, S. R. (2006). Estimation of biomass burning emissions on south america using field observations and remote sensing. In *Proceedings of 8 ICSHMO*, pages 115–119.

Mandel, J., Chen, M., Coen, J. L., Douglas, C. C., Franca, L. P., Johns, C., Kremens, R., Puhalskii, A., Vodacek, A., and Zhao, W. (2004a). Dynamic data driven wildfire modeling. In *Dynamic Data Driven Applications Systems*. kluwer.

Mandel, J., Chen, M., Franca, L., Johns, C., Puhalskii, A., Coen, J., Douglas, C., Kremens, R., Vodacek, A., and Zhao, W. (2004b). A note on dynamic data driven wildfire modeling. In *Proceedings ICCS*.

McCaffrey, B. J. (1979). Purely buoyant diffusion flames: Some experimental results. Technical Report 79-1910, National Bureau of Standards.

McGrattan, K. B., Baum, H., Rehm, R., Hostikka, S., and Floyd, J. (2007). *Fire Dynamics Simulator (Version 5) Technical Reference Guide*. Natl. Inst. Stand. Technol. Spec. Publ. 1018-5.

Mell, W., Jenkins, M. A., Gould, J., and Cheney, P. (2007). A physics-based approach to modelling grassland fires. *International Journal of Wildland Fire*, **16**, 1–22.

Miller, J. D. and Yool, S. R. (2002). Mapping forest post-fire canopy consumption in several overstory types using multi-temporal landsat TM and ETM data. *Remote Sensing of Environment*, **82**, 481–496.

Myers, D. R., Emery, K., and Gueymard, C. (2004). Revising and validating spectral irradiance reference standards for photovoltaic performance evaluation. *Journal of Solar Energy Engineering*, **126**, 567–574.

National Institute of Standards and Technology (2007). NIST atomic spectra database. http://physics.nist.gov/PhysRefData/ASD/.

National Park Service (1999). *Wildland Fire Management Reference Manual*. U.S. Department of the Interior.

Newman, J. S. and Wieczorek, C. J. (2004). Chemical flame heights. *Fire Safety Journal*, pages 375–382.

Nguyen, D., Enright, D., and Fedkiw, R. (2003). Simulation and animation of fire and other natural phenomena in the visual effects industry. Technical report, Western States Section, Combustion Institute, UCLA. Fall Meeting.

Nguyen, D. Q., Fedkiw, R., and Jensen, H. W. (2002). Physically based modeling and animation of fire. *SIGGRAPH*, pages 721–728.

Orloff, L. and de Ris, J. (1982). Froude modeling of pool fires. In *Nineteenth Symposium (International) on Combustion*, pages 885–895.

Ostlie, D. A. and Carroll, B. W. (1996). *An Introduction to Modern Stellar Astrophysics*. Addison-Wesley Publishing Company, Weber State University.

Perry, C. and Picard, R. (1994). Synthesizing flames and their spreading. In *Proc. of the Fifth Eurographics Work shop on Computer Animation and Simulation, Oslo, Norway*, pages 105–117.

Radke, L., T.L.Clark, Coen, J., Walther, C., Lockwood, R., Riggan, P., Brass, J., and Higgins, R. (2000). The wildfire experiment(WiFE): Observations with airborne remote sensor. *Canadian Journal of Remote Sensing*, **26**(5), 406–417.

Reeves, W. T. (1983). Particle systems - technique for modeling a class of fuzzy objects. *ACM Transactions on Graphics*, **2**, 91–108.

Reeves, W. T. (1985). Approximate and probabilistic algorithms for shading and rendering structured particle systems. *Computer Graphics*, **19**(3), 313–322.

Richards, J. A. and Jia, X. (1998). *Remote Sensing Digital Image Analysis*. Springer, 3 edition.

Riggan, P., Hoffman, J., and Brass, J. (2000). Estimating fire properties by remote sensing. In *Aerospace Conference Proceedings, IEEE*, volume 3, pages 173–179.

Ris, J. L. D. (2002). Will it support a self-propagating fire? Technical report, National Institute of Standards and Technology.

Rizzi, R. and Saunders, R. (1998). http://www.ecmwf.int/newsevents/training/ rcourse_notes/DATA_ASSIMILATION/REMOTE_SENSING/Remote_sensing 2.html.

Rothermel, R. C. (1972). A mathematical model for predicting fire spread in wildland fires. Technical Report INT-115, USDA Forest Service.

Rushmeier, H. and Hamins, A. (1995). Volume rendering of pool fire data. *IEEE Computer Graphics and Applications*, **15**(4), 62–66.

Salvador, R., Díaz-Delgado, R., Valeriano, J., and Pons, X. (1998). Remote sensing of forest fires. In *Proc. of GIS PlaNET'98 International Conference and Exhibition on Geographic Information*, Lisbon, Portugal.

Salvador, R., Valeriano, J., Pons, X., and Diaz-Delgado, R. (2000). A semi-automatic methodology to detect fire scars in shrubs and evergreen forests

with landsat mss time series. *International Journal of Remote Sensing*, **21**, 655 – 671.

Schott, J., Brown, S., Raqueno, R., Gross, H., and Robinson, G. (1998). Advanced synthetic image generation models and its application to multi/hyperspectral algorithm development. In *Proceedings of the AIPR Workshop in Washington DC*.

Schott, J. R. (1997). *Remote Sensing: The Image Chain Approach*. Oxford University Press.

Schott, J. R. (2007). *Remote Sensing: The Image Chain Approach*. Oxford University Press, 2 edition.

Smith, M. O., Ustin, S. L., Adams, J. B., and Gillespie, A. R. (1990a). Vegetation in deserts: I. a regional measure of abundance from multispectral images. *Remote sensing of environment*, **31**, 1–26.

Smith, M. O., Ustin, S. L., Adams, J. B., and Gillespie, A. R. (1990b). Vegetation in deserts: II. environmental influences on regional abundance. *Remote sensing of environment*, **31**, 27–52.

Stam, J. and Fiume, E. (1995). Depicting fire and other gaseous phenomena using diffusion processes. In *Proceedings of SIGGRAPH 95, Computer Graphics Proceedings*, pages 129–136.

University of Wisconsin-Madison (2006). *Condor Version 6.6.9 Manual*.

Viegas, D. X. (2004). Slope and wind effects on fire propagation. *International Journal of Wildland Fire*, **13**, 143–156.

Vodacek, A., Kremens, R. L., Fordham, A. J., Vangorden, S. C., Luisi, D., Schott, J. R., and Latham, D. J. (2002). Remote optical detection of biomass burning using a potassium emission signature. *International Journal of Remote Sensing*, **23**, 2721–2726.

Wei, X., Li, W., Mueller, K., and Kaufman, A. (2002). Simulating fire with texture splats. In *Proceedings of the conference on Visualization, Boston*, pages 227–234.

Weinstein, D., Green, K., Campbell, J., and Finney, M. (1995). Fire growth modeling in an integrated gis environment. In *ESRI International User Conference*.

Weise, D. R. and Biging, G. S. (1996). Effects of wind velocity and slope on flame properties. *Can. J. For. Res.*, **26**, 1849–1858.

White, J., Ryan, K., Key, C., and Running, S. (1996). Remote sensing of forest fire severity and vegetation recovery. *International Journal of Wildland Fire*, **6**(3), 125 – 136.

Wooster, M. J., Zhukov, B., and Oertel, D. (2003). Fire radiative energy for quantitative study of biomass burning: derivation from the BIRD experimental satellite and comparison to MODIS fire products. *Remote Sensing of Environment*, **86**, 83–107.

Wooster, M. J., G.L.W.Perry, Zhukov, B., and Oertel, D. (2004). Estimation of energy emissions, fireline intensity and biomass consumption in wildland fires: A potential approach using remotely sensed fire radiative energy. In *Spatial*

Modeling of the Terrestrial Environment, pages 175–196. John Wiley & Sons Ltd.

Worden, H., Beer, R., and Rinsland, C. P. (1997). Airborne infrared spectroscopy of 1994 western wildfires. *Journal of geophysical research*, **102**, 1287–1300.